The teleconnections from the Indian Ocean Dipole to the North Atlantic region with a focus on the boreal winter season 2019/2020



Tim Hempel

Trinity College University of Oxford

Supervised by

Antje Weisheimer

Tim N. Palmer

12.02.2024

Abstract

Accurate seasonal forecasts of the extratropical atmospheric circulation are reliant on a precise representation of teleconnections from the tropics. Understanding the mechanisms that link the tropics to the extratropical circulation anomalies in reanalysis and models gives an insight into the teleconnections involved and where model forecasts deviate from observations.

For the winter weather in Europe, the phase of the North Atlantic Oscillation is of high importance as it has a large influence on the average wind, temperature, and precipitation. The positive phase of the NAO brings warm and wet air to Northern Europe and simultaneously drying Southern Europe, while the negative phase brings colder and dryer conditions to Northern Europe and wet conditions to Southern Europe. Therefore, it is important to identify components of the climate system that interact with the NAO.

In the boreal winter of 2019/2020, the NAO was unusually well predicted with many seasonal forecast models accurately forecasting a positive NAO. This high agreement between different models point towards a common well represented mechanism in the models. A well known source of predictability on seasonal timescales is the El Niño Southern Oscillation (ENSO). However, in 2019/2020 ENSO was in a neutral state which points towards another tropical mechanism being the source of the good NAO forecast.

Here, I investigate teleconnections from the Indian Ocean Dipole as a source of predictability for the NAO in the boreal winter of 2019/2020. In model experiments with ECMWF's OpenIFS I perturb boundary conditions and initial conditions and identify the IOD as the main aspect of 2019/2020 that led to the strong- well forecasted NAO. Experiments with Sea-Surface-Temperatures in the Indian Ocean from 2019/2020 and climatological average SSTs everywhere else, show a positive Arctic Oscillation/NAO that is close to the observed conditions.

In reanalysis, enhanced convection over the western Indian Ocean forced by high SSTs, induce a Rossby wave train that propagates north- eastward and impacts the

North Pacific and North Atlantic. The model experiments support this Rossby wave train, but they also reveal another mechanism associated with eddy, mean-flow interactions. In the North Pacific the strength and latitude of the eddy-driven jet is modified due to the strong IOD. This shift of the Pacific jet and the accompanying eddy field then propagates downstream and induces similar shifts in the North Atlantic and anomalies in the NAO.

Analysing and modelling the IOD teleconnections towards the Southern Hemisphere did not reveal a robust impact of the IOD on the Southern Annular Mode. In 2019/2020 the strong anomalies in the SAM are linked to anomalous initial conditions over the southern high latitudes that impact atmosphere in this season and no large influence from the tropics could be identified.

I propose the mechanism depicted in Figure 1 as the path of the teleconnection between the Indian Ocean and the North Atlantic. The heating and convection dipole in the Indian Ocean create the conditions for a Rossby wave train that propagates into the North Pacific creating an anomalous high over the Aleutian cyclone region. This shifts and extends the Pacific jet northward leading to more anticyclonic wave breaking in the Pacific jet exit region. This preconditions the Atlantic jet into a more northerly and extended phase as well, which is associated with a positive NAO.

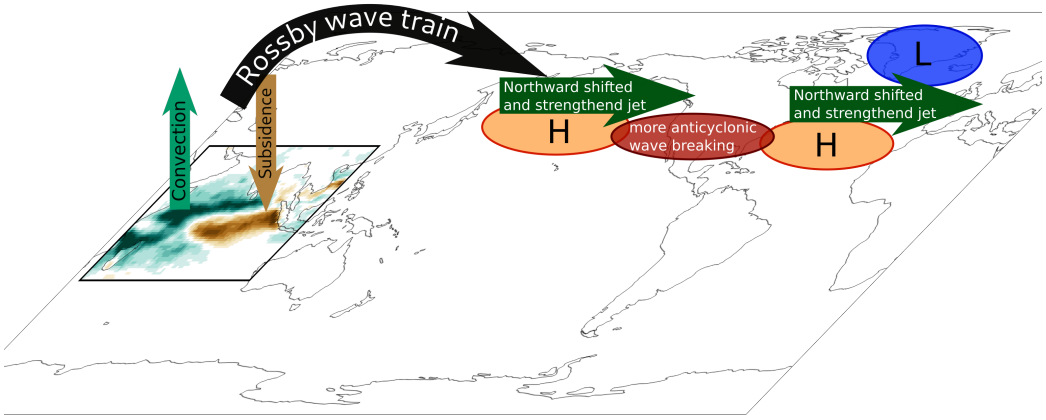


Figure 1: **Schematic of proposed IOD teleconnections**

Acknowledgements

I am immensely grateful for all the support I had during my time here in Oxford. Without all the help from everyone around me I would not have managed to write this thesis.

First, I would like to thank Antje and Tim for your continued guidance, your questions and inspirations during our meeting, and that you have given me a better understanding of our climate system. During the time here I have learned how little I knew before about the climate system and how much there is still to discover and that is honestly very exciting (to me). I really appreciate the group you both have built and I have learned a lot during the group meetings and in discussions with you and other members of the group.

I thank all members of this research group, but want to mention a few of you specifically:

Chris, Adnan, and Matt: Thank you for all the good discussions and the help you gave me throughout my DPhil. I always really enjoy our discussions and have learned so much from you.

Glenn and Sarah: You have helped me with all the model troubles I had and I couldn't be more grateful. Without you I would not have managed to get the model running (twice). It is always good to hear from you and understand the more technical side of models a bit better.

I would also like to thank my Master Thesis supervisors Johanna and André. Without you both I would not be on this path, you got me excited about seasonal forecasts, and I still am. Thank you for that.

I am so lucky to have friends like all of you! I could not have done this without you and I can not describe how happy and privileged I feel to know you!

Simon and Kevin: I can't really write how happy I am that we are still such good friends even with a little distance between us. When we became friends I felt like I found people who I understand and who understand me, thanks for that.

Andrew, talking with you is always great and I know we can loose hours and hours

just discussing some small little nerd thing ... I am always really enjoying that. You are probably the person I have talked most with in the last four years and I am really happy that I could.
I am also happy to have so many other good friends: Andrew W., Ed, Emily, and Mat; Andrea, Birte, Rike, and Caro; Lea and Jana; Christoph, Cally, and Tevio; Noa and Franzi. Thank you for everything.
Mama and Papa, thank you for being always there. Thanks for helping and supporting me, thanks for listening and teaching me. Thanks for raising me and everything you did with and for me. Also thanks to Oma for such a very good time when I was young.

There are so many more that I would like to and should thank, but sadly this will have to end somewhere. However, I want to say thank you to everyone who I have learned from, be it family, friends, or colleagues. I have learned so much because of you all in Biology, Psychology, Nature Conservation, Law, Languages, and much more and I will never be able to thank you enough for teaching me something new.
If you are reading this know that I have thought of you while writing, even if I have not mentioned you explicitly.

Contents

1 Outline **3**

2 Introduction **5**

2.1 Seasonal . . . 6

2.1.1 El Niño Southern Oscillation . . . 6

2.1.2 Indian Ocean Dipole . . . 8

2.1.3 Timing of Indian Ocean Dipole teleconnections . . . 11

2.1.4 Co-occurring IOD and ENSO . . . 12

2.1.5 The North Atlantic Oscillation . . . 13

2.1.6 Monsoon systems . . . 14

2.1.7 Southern Annular Mode . . . 15

2.1.8 Rossby wave train . . . 15

2.2 Side note on Sub-Seasonal timescale . . . 16

2.3 Background conditions of 2019/2020 in ERA5 . . . 18

2.3.1 Tropical anomalous conditions . . . 18

2.3.2 Northern Hemisphere anomalous conditions . . . 23

3 Methods **26**

3.1 OpenIFS model . . . 26

3.2 OpenIFS sensitivity experiments . . . 27

3.3 ECMWF model overview . . . 28

3.4 Significance calculation . . . 30

3.5 E-Vectors . . . 30

3.5.1 Eddy feedback . . . 32

4 Forecasts of 2019/2020 **33**

4.1 ECMWF model forecast . . . 33

4.2 C3S model forecast performance . . . 39

5 OpenIFS model experiments **43**
5.1 OpenIFS control forecast . . . 43
5.2 OpenIFS experiments . . . 47
5.3 Combination of tropical drivers . . . 55
5.4 Impact of climate change on the IOD event of 2019/2020 . . . 62

6 Stratosphere in reanalysis and forecast **69**
6.1 Analysis of stratospheric forecasts . . . 69

7 Rossby wave train teleconnection **76**
7.1 OpenIFS@Home control experiments . . . 81
7.1.1 Composites . . . 81

8 Eddy, mean-flow interactions **88**
8.1 Climatological E-Vectors . . . 89
8.2 2019/2020 E-Vector teleconnection . . . 93

9 Initial condition impact on the Southern Hemisphere **103**
9.1 Individual months of the Southern Hemisphere . . . 109

10 Differences in hindcasts **114**
10.1 Geopotential height differences between models . . . 114
10.2 Origin of differences and propagation . . . 118

11 Conclusion and Outlook **121**
11.1 Proposed teleconnection mechanism . . . 129

Bibliography **131**

List of Figures

1 Schematic of proposed IOD teleconnections 4

2.1 Schematic depiction a strong IOD event 10
2.2 Anomalous conditions in SON 2019 20
2.3 Anomalous conditions in DJF 2019/2020 22
2.4 Northern Hemisphere anomalies in DJF 2019/2020 24
2.5 European anomalies in DJF 2019/2020 25

4.1 Z500 from ECMWF models in DJF 2019/2020 36
4.2 NAO in 2019/2020 in OIFS and SEAS5 members 38
4.3 TP from C3S models in DJF 2019/2020 40
4.4 Z500 from C3S models in DJF 2019/2020 42

5.1 OpenIFS comparison to SEAS5 and ERA5 45
5.2 OpenIFS tropical ocean experiments 50
5.3 OpenIFS NAO in experiments 53
5.4 Extratropics OpenIFS experiments 54
5.5 OpenIFS small and large Pacific experiment 57
5.6 Linear combination of OpenIFS experiments 59
5.7 Impact of climate change on the Indian Ocean experiment 65
5.8 Impact of climate change on the Pacific Ocean experiment 67

6.1 Stratospheric conditions in ERA5, SEAS5, and OpenIFS 72
6.2 Ensemble stratospheric conditions 73
6.3 U10 from C3S models in DJF 2019/2020 75

7.1 Northern Hemisphere wave train in 2019/2020 78
7.2 V200 from C3S models in DJF 2019/2020 80
7.3 Wavetrain composite in a large ensemble 82
7.4 Large ensemble composite AO 83
7.5 AO indices in the large ensemble 84

7.6 Large ensemble composite NAO 85
7.7 NAO indices in the large ensemble 87

8.1 Climatological E-Vectors in models 92
8.2 Climatological eddy acceleration 93
8.3 ERA5 mean flow and eddies in 2019/2020 94
8.4 SEAS5 mean flow and eddies in 2019/2020 96
8.5 OpenIFS control experiment mean flow and eddies in 2019/2020 . . . 98
8.6 OpenIFS IO only experiment mean flow and eddies in 2019/2020 . . . 100
8.7 OpenIFS Pacific only experiment mean flow and eddies in 2019/2020 101

9.1 Southern Hemisphere anomalies in the DJF season 108
9.2 Southern Hemisphere anomalies in months with forcing from 2019/2020 110
9.3 Southern Hemisphere anomalies in months with forcing from 1981/1982 113

10.1 Differences in DJF Z500 climatological averages 116
10.2 Differences in DJF D200 and U200 climatological averages 118
10.3 Differences in DJF E-Vectors in climatological averages 119

11.1 Schematic of proposed IOD teleconnections 129

”It is likely that the early winter 2023/2024 will exhibit a positive NAO, influenced by the positive IOD, while the ENSO influence on the late winter will lead to a negative NAO.” (Tim Hempel, October 2023)

Abbreviation	Long name
IOD	Indian Ocean Dipole
NAO	North Atlantic Oscillation
AO	Arctic Oscillation
ENSO	El Niño Southern Oscillation
IO	Indian Ocean
MJO	Madden-Julian-Oscillation
SSW	Sudden Stratospheric Warming
ECMWF	European Centre for Medium-Range Weather Forecasts
ERA5	ECMWF reanalysis version 5
SEAS5	ECMWF's seasonal forecasting system version 5
OpenIFS	ECMWF's open version of the Integrated Forecasting System
C3S	Copernicus Climate Change Service
UKMO	UK Met Office
DWD	German Weather Service
CMCC	Euro-Mediterranean Center on Climate Change
Météo-France	French Weather Service
MMM	Multi-Model Mean
hc	hindcast
IC	initial conditions
BC	boundary conditions
DJF	December-January-February
ND	November-December
JF	January-February
SON	September-October-November
NH	Northern Hemisphere
SH	Southern Hemisphere
SST	Sea Surface Temperature
TP	Total Precipitation

Chapter 1

Outline

This thesis investigates teleconnections on seasonal timescales, with the focus placed on the atmospheric teleconnection from the Indian Ocean to the North Atlantic region. I investigate the boreal winter season 2019/2020 as a prime example of a year with an Indian Ocean Dipole event but without ENSO. The following questions are investigated:

- Why is the winter season 2019/2020 worth researching and what are its special features?
- Why do seasonal forecast models agree in their forecast of this winter and what are commonalities between models?
- How does different tropical SST forcing from 2019/2020 impact the atmospheric state in the OpenIFS model?
  - Is SST forcing in the Indian Ocean region enough to significantly impact the AO/NAO?
  - Does a combination of multiple ocean regions still show the impact of the IOD on the AO/NAO?
  - How does the climate change signal impact the teleconnections from the Indian Ocean?
- What teleconnection pathways are identifiable in 2019/2020?
  - Does the teleconnection pathway to the North Atlantic involve the stratosphere and how well is it represented in models?

  - What is the role of the Rossby wave train from the Indian Ocean to the North Pacific and from there to the North Atlantic?
  - What is the role of eddy, mean-flow interactions as a teleconnection mechanism between the North Pacific and North Atlantic?

- What is the sensitivity of the Southern Hemisphere to Boundary- and Initial-Condition forcing in 2019/2020?

- Three different methods are used to define the climatological average of the model. How large are the differences between these possible climatological averages?

Chapter 2

Introduction

This chapter describes the fundamental climate processes of the Indian Ocean, its known teleconnections to the Northern Hemisphere, and the background conditions of the winter 2019/2020. It serves as a base from which the research in this thesis is conducted.

On seasonal timescales remote regions of the climate system can be connected to each other. Wallace and Gutzler (1981 [83]) found that the Northern Hemisphere extratropical pressure in the high latitudes is anti-correlated with the mid latitudes. They called this phenomenon teleconnections and identified with it the North Atlantic Oscillation (NAO), the Arctic Oscillation (AO), and others. Since then a lot of different teleconnections have been identified between different regions of the world. One of the strongest and most researched ones is the teleconnection between the tropical Pacific (El Niño Southern Oscillation (ENSO)) and the North Atlantic region (see chapter 2.1.1 or Butler et al., 2014 [9] for tropospheric and Domeisen et al., 2018 [14] for stratospheric teleconnections).
The research on seasonal teleconnections is largely focused on the boreal winter season (December-February (DJF)). In DJF the tropical Pacific has the largest variance with ENSO peaking in this season (Webster, 2020 [86]). At the same time the boreal winter is the season where the NAO is most predictable (O'Reilly et al., 2018 [59]; Scaife et al., 2014 [68]). This co-occurrence of highest variance in the Pacific and high predictability in the North Atlantic region is no coincidence since there are teleconnection pathways from the Pacific towards the Atlantic. These teleconnections serve as a link from the seasonally well predictable tropics to the less well predictable extratropics and can help to increase the forecast skill in the extratropics.
In seasonal forecasts a lot of models and analyses face the so-called "signal-to-noise paradox" (Scaife and Smith, 2018 [70]; Weisheimer et al., 2024 [88]; Hardiman et al.,

2022 [26]). Especially in the North Atlantic area, seasonal forecast models tend to be under-confident evident in a very large ensemble spread. While the variance of the ensemble is often correct in the models, the ensemble spread in each year is too large and the ensemble mean values are much lower than the observations. This difference in the amplitude of the ensemble mean in the signal-to-noise paradox has an implication on many skill scores. For example, the root-mean-squared error will show larger errors in a forecast with the signal-to-noise paradox, while a correlation score will show a much better forecast. A possible reason for the signal-to-noise paradox are too weak teleconnections (Weisheimer et al., 2024 [88], Garfinkel et al., 2022 [20]) and too weak interactions between eddies and the mean flow (Hardiman et al., 2022 [26]).
The signal-to-noise paradox is present in this thesis as well, often evident in the much too weak ensemble mean. However, depictions of the full ensemble show that most times the ensemble envelopes the observation and that ensemble members with larger amplitudes than the observations exist.

The Indian Ocean and Atmosphere interact on a large range of timescales (Webster, 2020 [86]); from sub-seasonal phenomena such as the Madden-Julian-Oscillation (Madden and Julian, 1971 [47]) to centennial phenomena such as the Indian Ocean warming (Gnanaseelan et al., 2020 [21]). The climate modes on these timescales can be at times of a similar strength to the ones that govern the Pacific, albeit in a smaller basin (Webster et al., 1999 [87]). In the following I will first discuss the different relevant processes in the tropical and extratropical regions. Afterwards, I show the main features of the boreal winter season 2019/2020. The main focus of this thesis is on the seasonal timescale December to February (DJF).

2.1 Seasonal

This section describes processes on the seasonal timescale in the Indian Ocean region, the Pacific, and North Atlantic region.

2.1.1 El Niño Southern Oscillation

The El Niño Southern Oscillation (ENSO) is a planetary scale oscillation with a frequency of about 2-5 year, first shown by Sir Gilbert Walker in 1924 (Walker, 1924 [81]; Bjerknes, 1969 [6]; Webster, 2020 [86]). As a coupled ocean-atmosphere

oscillation it involves changes in the ocean (like Sea Surface Temperature (SST)) and in the atmosphere (like areas of increased convection) in the tropical Pacific (Webster, 2020 [86]; or https://www.climate.gov/enso). In the neutral phase of ENSO, high SSTs and convection rates persist in the western Pacific and over the Maritime Continent. During an El Niño (positive phase of ENSO), the area of highest SST and convection shifts towards the central and eastern Pacific (CP and EP El Niño: Kao and Yu, 2009 [39]; Takahashi et al., 2011 [75]), while during a La Niña (negative phase of ENSO) the high SST and convection rates in the western Pacific are increased.

To explain the quasi-cyclic nature of ENSO, two theories have been proposed. The recharge-discharge oscillator theory describes a continuous flow of warm surface water from east to west during neutral and La Niña conditions (Wyrtki, 1985 [91]; Meinen and McPhaden, 2000 [51]). In this theory, a warm water pool in the western tropical Pacific is (re-) charged during neutral and La Niña conditions and discharged during El Niño conditions where the warm water pool moves towards the central and eastern Pacific. An alternative theory is the delayed oscillator theory (Suarez and Schopf, 1988 [74]; Battisti and Hirst, 1989 [4]). In this theory, an El Niño event triggers slow westward travelling oceanic Rossby waves that reflect off the western boundary as equatorial Kelvin waves. When these upwelling Kelvin waves reach the central and eastern Pacific, they influence the depth of the thermocline resetting the conditions towards neutral and La Niña conditions.

It is likely that both mechanisms play an important role in the evolution of El Niño and La Niña transitions and their interactions are still being discussed (Izumo et al. 2024 [36]).

In boreal winter (December-February) the variance of ENSO and its impacts are much larger than in boreal summer (Webster, 2020 [86]). ENSO events have far reaching impacts on seasonal climates (Horel and Wallace, 1981 [31]; Trenberth et al., 1998 [79]; Domeisen et al., 2018 [14]), reaching other tropical oceans (Klotzbach, 2011 [42]), and both Northern and Southern high latitudes (e.g. NAO: Fraedrich and Mueller, 1992 [18]; SAM: Lim et al., 2013 [45]). These teleconnections propagate both via the troposphere (Butler et al., 2014 [9]) and the stratosphere (Domeisen et al., 2018 [14]). A more in-depth analysis of ENSO and its teleconnections can be found in (e.g. Webster, 2020 [86]; Domeisen et al., 2018 [14]; Butler et al., 2014 [9]).

2.1.2 Indian Ocean Dipole

The Indian Ocean Dipole (IOD) is a coupled ocean-atmosphere climate mode in the tropical Indian Ocean with its strongest amplitude in boreal autumn (SON) (Guo et al., 2015 [24]). Common definitions of the IOD are the SST or precipitation anomaly difference between the western and eastern Indian Ocean (e.g. Saji et al., 1999 [66] or Molteni et al., 2015 [55]). The Dipole Mode Index (DMI e.g. DMI definition from NOAA: https://psl.noaa.gov/gcos_wgsp/Timeseries/DMI/) is defined as the SST anomaly difference between the western Indian Ocean (wIOD = $10°N$ - $10°S$ and $50°E$ - $70°E$) and the eastern Indian Ocean (eIOD = $10°N$ - $0°$ and $90°E$ - $110°E$) (e.g. see boxes in Figure 2.2). A positive IOD event occurs when wIOD - eIOD > 0 i.e. the SST anomaly in the western Indian Ocean is higher than in the eastern Indian Ocean. Conversely a negative IOD event occurs when the difference between western and eastern Indian Ocean is negative. The temperature and pressure difference between the eastern and western Indian Ocean is usually smaller than the differences in the tropical Pacific, but extreme IOD events like the 97/98 IOD can reach similar strengths across the smaller basin (Webster et al., 1999 [87]).

The Total Precipitation (TP) anomaly difference between the same boxes is used as an alternative IOD definition to the SST one. Molteni et al. (2013 [54]) argue that it is preferable to define the IOD from the precipitation difference between east and west instead of the SST difference, since the precipitation is more closely related to the atmospheric dynamics of the region. Their analysis shows more consistent teleconnection patterns when using precipitation instead of SST. The IOD defined from precipitation agrees in most years with the IOD defined from SST, but is more dynamically linked. Again, anomalies in the eastern Indian Ocean are subtracted from the western Indian Ocean and a positive residual is defined as a positive IOD and vice versa. In the DJF 2019/2020 investigated here, the IOD was in a positive state both from the SST definition as well as the precipitation definition (see Chapter 2.3).

In the following, the mechanisms of the IOD will be explained using the example of the strong IOD event in autumn and winter of 1997/98. The event has been thoroughly discussed by Webster et al. (1999 [87]) and Webster (2020 [86]) and this Introduction of the IOD mechanics is largely based on their analysis. They show that the IOD is a coupled ocean-atmosphere phenomenon that is to a large degree independent of ENSO.

In the boreal summer of 1997, the northward monsoon winds in the western Indian Ocean were weaker than normal, while the northward winds in the eastern Indian

Ocean were stronger (Figure 2.1 a). These anomalous winds led to a reduced ocean upwelling in the western Indian Ocean and enhanced upwelling in the eastern Indian Ocean, resulting in a deeper thermocline in the west and a shallower thermocline in the east. The anomalous thermocline created an SST gradient with warmer temperatures in the west and colder ones in the east.

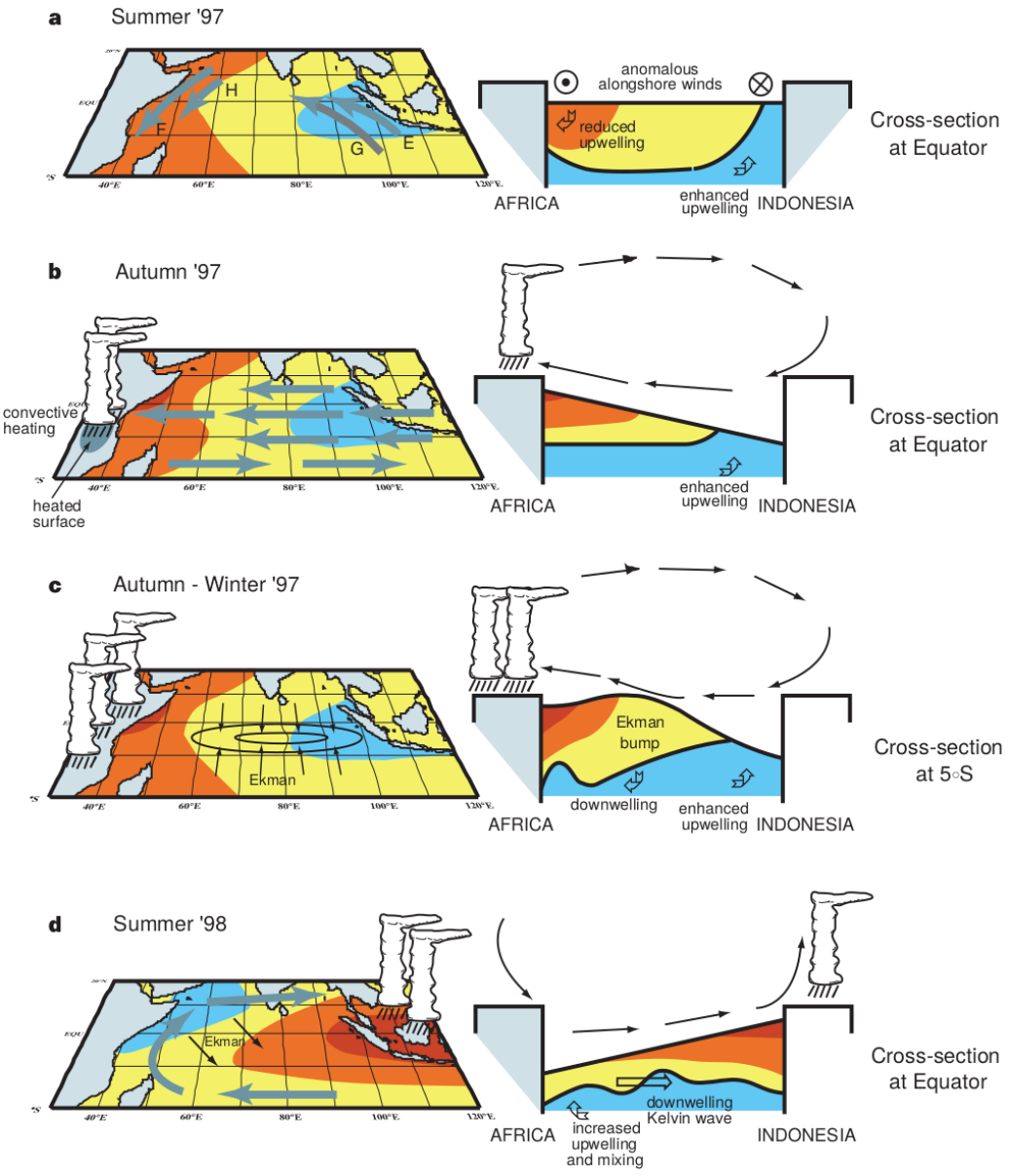


Figure 2.1: **Schematic depiction a strong IOD event** in 1997/98. Figure taken from Webster et al. (1999). **a)** shows the conditions in summer 1997 right at the onset of the IOD event. The SST and wind anomalies promote an intensification of convection in the west and decrease in the east. In autumn 1997 **b)**, the IOD is fully developed and in its strongest state with convection in the west and equatorial winds that force warm water towards the west. **c)** towards late autumn and winter, the warm water bump in the west is largest and some equatorial Rossby and Kelvin waves develop in the ocean (which will reset the IOD). In the following summer 1998 **d)** the conditions have reversed with most convection and warm water now in the east.

In the autumn a positive precipitation anomaly developed over the western Indian

Ocean and eastern Africa (Figure 2.1 b). This precipitation anomaly is associated with strong convection, low sea level pressure and higher pressure in the upper troposphere that led to an anomalous circulation pattern over the Indian Ocean. Low level easterlies and high level westerlies developed and over Indonesia convection is replaced by subsidence. The low level easterlies at the equator forced an oceanic surface water transport towards the west. These equatorial easterlies increase the west-east SST gradient and again enhanced cold upwelling in the east. South of the equator anomalous westerly winds balanced the easterlies at the equator (Figure 2.1 b). Together the equatorial easterly winds and the westerly winds further south created an Ekman transports in the ocean that led to a zone of convergence and high sea surface height (SSH) slightly south of the equator (Figure 2.1 c). In late autumn and winter, this SSH anomaly travelled westward as an oceanic Rossby wave. This wave transported again water from east to west and helped sustain the warm anomaly in the west longer into the autumn and winter season. The IOD event declined and reversed in late winter, spring, and summer of the next year (1998) (Figure 2.1 d). The Rossby wave that was present in autumn and winter reflected of the African coast as a equatorial Kelvin wave propagating eastward. Additionally, following an IOD event there is a high chance of a strong summer monsoon with stronger upwelling off the African coast and colder SSTs. The convective area over Indonesia also reestablishes itself and with it the low level westerly winds over the Indian Ocean that drive water at the equator from west to east, creating a shallower thermocline in the west and a deeper one in the east.

It has to be noted that the winter 1997/98 experienced one of the strongest El Niño events on record. A strong El Niño also leads to more subsidence over Indonesia which very likely contributed to the strength of the IOD event in that year. Other years, like the 2019/2020 winter show that IOD events can develop without an ENSO event in the same year. The special case of the 2019/2020 winter is discussed more in this Thesis, as it offers a chance to analyse the IOD with minimal interference from ENSO.

2.1.3 Timing of Indian Ocean Dipole teleconnections

Typically seasonal teleconnections to the North Atlantic Oscillation (NAO) are investigated in the boreal winter season (DJF), as the NAO is most stable in this season. This season fits well for investigation of teleconnections between the El Niño Southern Oscillation (ENSO) and the NAO, since ENSO generally also has its maximum amplitude in this season (Kirtman and Shukla, 2000 [40]). For the IOD however, the

DJF season is not the season with the largest variance. As the previous chapter discusses, the IOD developes in boreal summer, matures in autumn, and usually decays in winter (Xu et al., 2021 [92]) (only very strong IOD events last into late winter). This means that the IOD is strongest in the SON season and it is already decaying in DJF, so that only very strong IOD events will have an obvious teleconnection in DJF mean. Abid et al. (2023 [1]) and Joshi et al. (2021[38]) show in ERA5 and model experiments that teleconnections from the Indian Ocean dominate in early winter (ND), while ENSO teleconnections dominate the late winter (JF). Abid et al. (2023 [1]) show that there is a significant impact from western Indian Ocean precipitation anomalies (western region of the IOD) onto the NAO in early winter. A positive precipitation anomaly (positive IOD) projects onto the positive phase of the NAO. They also show that removing the signal from the Indian Ocean region decreases the NAO forecast skill more than removing ENSO skill in early winter. Thus, when traditional definitions of the winter season are used, more of the ENSO teleconnection is captured than from the IOD if both ENSO and IOD occur in the same year. This makes years important when only the IOD is active and ENSO is in a neutral phase, as these years offer an opportunity to investigate the IOD teleconnection in detail without the interference of ENSO in the DJF season. As shown below (Chapter 2.3), the winter 2019/2020 is a year with a strong IOD without ENSO.

2.1.4 Co-occurring IOD and ENSO

Most years when the IOD is in a strong phase, ENSO is also in a strong phase (or arguably when ENSO is in a strong phase then the IOD is also in a strong phase). A positive IOD event and El Niño both share a shift of the Walker circulation away from the climatological mean over the Maritime Continent (Klein et al., 1999 [41]; Wang and Wang, 2014 [85]). In a developing El Niño state, the convection over the Maritime Continent is suppressed. This increased subsidence can lead to a simultaneous El Niño and positive IOD state (Fischer et al., 2005 [17]). While the convection over the Maritime Continent is decreased, the convection is increased over the western Indian Ocean and over the central Pacific in a combined positive IOD/ El Niño year. As described above, in years with both ocean regions active it is more difficult to investigate the teleconnections from the IOD as they get overshadowed by ENSO teleconnections in DJF mean. Therefore, I investigated ECMWF's CERA-20C reanalysis of the 20.th century to see how often IOD and ENSO co-occur (Table 2.2). Every year in the 109 winters between 1901 and 2010 is separated into a positive/neutral/negative IOD and El Niño/neutral/La Niña conditions. Selecting this

		IOD SST SON			
		+	0	-	
ENSO	+	20	10	2	32
	0	2	23	13	38
	-	4	14	20	38
		26	47	35	109

Table 2.2: **IOD and ENSO events between 1901-2010** in CERA-20C. IOD index calculated from SST in SON and ENSO index calculated from Niño3.4 DJF, both separated into positive, neutral, and negative phase. Diagonal are the years where both IOD and ENSO are in the same phase. Colours illustrate the relative number of years the combination occurs. High number of occurrence is green, medium is yellow, and low number of occurrence is red.

way shows that in most years, IOD and ENSO co-occur (diagonal in Table 2.2). During neutral IOD years, some positive and negative ENSO events occur, but the number of IOD events in neutral ENSO phase is very small. During neutral ENSO, some negative IOD's occur (enhanced climatological state with more precipitation over the maritime continent), but very few positive IOD's exist without positive ENSO (2019/2020 is not included here). This skew towards the same phase of ENSO and IOD makes the exact teleconnections from the Indian Ocean difficult to research. Nevertheless, a solid understanding of the Indian Ocean teleconnection will help the understanding of the combined ENSO-IOD system as well.

2.1.5 The North Atlantic Oscillation

The North Atlantic Oscillation (NAO) as a dipole of sea level pressure (MSL) was discussed as early as Defant (1924 [13]) and Walker and Bliss (1936 [82]). Investigating station data these studies find the generally high pressure over the Azores region and the generally low pressure over the Iceland region to be anti-correlated. This dipole is especially evident in the boreal winter from December to February (DJF). Wallace and Gutzler (1981 [83]) show a more in-depth analysis of the NAO, with more available years and using the 700 - 1000 mb thickness difference between Iceland and Oslo. They show that the NAO is connected with the Aleutian Low and is part of northern high latitude low pressure system.

Another common way to compute the NAO is to calculate the MSL (or Z500) difference of a larger area in the high- and mid-latitudes or as the first EOF of MSL (or Z500) over the North Atlantic (Hurrell, 1995 [33]; Hoerling et al., 2001 [28]).

The variability of the NAO is of major importance to the winter climate in Europe

and over the Atlantic (Hurrell et al., 2003 [34]). It influences the temperature and precipitation over large areas and changes the storm track across the North Atlantic (Scaife et al., 2008 [69]). It is therefore important to understand all factors that influence the NAO.

2.1.6 Monsoon systems

The summer and winter monsoons play an important role on almost all timescales in the Indian Ocean. For the case of the IOD, the strength of the Indian/ East Asian monsoon in boreal summer can precondition the IOD in autumn. An in depth explanation of the monsoon system in the Indian Ocean can be found in "Dynamics of the Tropical Atmosphere and Ocean" by Webster (2020 [86]), that also serves as the main reference for this section.

Two monsoon systems surround the Indian Ocean, the Indian/East Asian monsoon and the Australian monsoon. The Indian monsoon is the strongest monsoon system on Earth. In summer and winter the Intertropical Convergence Zone (ITCZ) over the Indian Ocean is located far off the equator (north in boreal summer and south in winter). This shift of the ITCZ changes the position and strength of the Hadley cells and the associated wind in the upper and lower troposphere. In summer (JJA) and winter (DJF) the changes of the Hadley cells are so large that winds cross the equator, from south to north in summer and from north to south in winter. The strong convection that is associated with the ITCZ is located over India. In boreal summer the air accumulates heat and moisture over the ocean, that lead to the strong convection and precipitation over northern India and East Asia. In addition, the location of the Himalayas creates a barrier for the winds that have to rise up to pass them. This makes India and East Asia a region with the highest amount of precipitation on Earth in boreal summer.

In winter the central Asian high pressure system is again very pronounced and winds cross the equator in the Somalian Jet from north to south. In this season, the winds are coming from the continent and are cold and dry, creating the dry season over India and East Asia.

The seasonally varying Somalian Jet creates the Somali current in the ocean, the largest ocean current to seasonally change its direction. The reversing winds have implications for the Sea Surface Temperature (SST) in the western Indian Ocean. At the coast upwelling prevails in boreal summer and downwelling in winter. This impact of the winds on the SST has an influence on other climate modes in the Indian Ocean like the IOD (see below).

These changes in the wind and the large cross equatorial pressure gradient lead to regions where the zero line of absolute vorticity (η) lies far off the equator. This can be as far as $10°N$ in boreal summer and $8°S$ in winter. Between the $\eta = 0$ line and the equator, is a region where $\eta/f < 0$ (f being the Coriolis parameter), these regions are inertially unstable, leading to more convection due to this instability (Tomas and Webster, 1997 [77]). For the IOD these inertially unstable regions are important for the onset of strong precipitation anomalies in the eastern and western Indian Ocean.

2.1.7 Southern Annular Mode

The Southern Annular Mode (SAM) represents the Z500 (or MSL) dipole between the southern mid-latitudes ($40°S$) and high-latitudes ($65°S$) (Gong and Wang, 1999 [22]). The SAM is mostly zonally symmetric with these two centres of action split into bands. The first is in the southern mid-latitudes between approx. $30 - 45°S$ and the second one is around the South Pole from approx. $60°S$ to $90°S$. In the climatological average, the southern centre is governed by lower pressure, with on average higher pressure in the mid-latitudes. Similar to the AO and NAO, the SAM can be separated into two phases, in the positive phase a positive pressure anomaly persists in the mid-latitudes with a the negative anomaly in the high-latitudes. In the negative phase of the SAM, the anomalies are reversed. This pressure dipole can shift the climatological mid-latitude westerly jet towards higher or lower latitudes (on average around $50°S$) (e.g. Fyfe, 2003 [19], and Marshall, 2003 [49]).
The SAM is commonly computed as the first EOF of Z500 in the Southern Hemisphere extratropics or with station based MSL data around Antarctica at $60°S$ and $90°S$ (Gong and Wang, 1999 [22]).

2.1.8 Rossby wave train

Rossby and collaborators (1939 [65]) found stationary weather systems over the United States associated with un-moving high and low pressure systems in both summer and winter months. They found that perturbations from the zonal mean structure propagate westward in the absence of a mean flow using concepts discussed in Bjerknes (1937 [5]). The dispersion relation of Rossby waves shows this propagation very clearly as:

$$c = \frac{\omega}{k} = U - \frac{\beta}{k^2 + l^2} \tag{2.1}$$

In the absence of a mean flow U, the phase speed of Rossby waves (c) is always negative, since the β-plane (β) and the zonal and meridional wavenumbers (k and l) are always positive (e.g. Holton and Hakim, 2012 [30]). This means that the Rossby phase speed is always westward. In the real atmosphere, the mean flow is rarely small and Rossby waves can be stationary or travel eastward in the jet.

The Rossby wave source discussed in Sardesmukh and Hoskins (1988 [67]; below and their equation 4) gives an indication of where Rossby waves originate.

$$S = -v_\chi \cdot \nabla\zeta - \zeta D \tag{2.2}$$

Where v_χ is the divergent component of the wind and ζ is the absolute vorticity. Here $-v_\chi \cdot \nabla\zeta$ is the advection of absolute vorticity by the divergent flow and $-\zeta D$ gives the vortex stretching (Nie et al., 2019 [56]). This method can be used to identify where the conditions for Rossby wave generation are favourable.

2.2 Side note on Sub-Seasonal timescale

Even though sub-seasonal processes are not the focus of this thesis, studies have shown teleconnections from the Indian Ocean region to the North Atlantic on the sub-seasonal timescale (e.g. Cassou, 2008 [10]; Lin et al, 2010 [46]; Skinner et al, 2022 [72]). This shows that teleconnections from the Indian Ocean can exist.

On the sub-seasonal timescale, the most important climate mode in the Indian Ocean is the Madden-Julian-Oscillation (MJO), discovered by Madden and Julian (Madden and Julian, 1971 [47]; Madden and Julian, 1994 [48]). They describe the MJO as 40-50 day large-scale tropospheric oscillation, originating in the Indian Ocean travelling eastward along the equator. An MJO event is characterised by an eastward travelling region of strong convection and anomalous subsidence to the east and west of the convection (Madden and Julian, 1994 [48]; and Waliser et al., 2009 [80]). The MJO cycle usually does not have a clear start or end. After the defined last phase of the cycle is reached, the oscillation usually starts again with a developing convective region over the Indian Ocean.
Several studies have investigated the teleconnection from the MJO in the Indian and

Pacific Ocean to the northern mid- and high-latitudes. Ferranti et al. (1990 [16]) find a connection between oscillations of the Outgoing Longwave Radiation (OLR) in the Indian and Pacific Ocean and the NAO. The MJO in the Indian and Pacific Ocean acts as a source of anomalous heating and convection, leading to divergence in the upper troposphere above the centre of the MJO. This divergence acts as a Rossby wave source that excites Rossby waves travelling into the extratropics (Sardeshmukh and Hoskins, 1988 [67]). In the mid-latitudes, these Rossby waves enter the mid-latitude jet and propagate eastward in this background flow. In reanalysis data, Matthews et al. (2004 [50]) find an atmospheric pattern over the Pacific that resembles the Pacific North American pattern (PNA). The positive PNA is characterised by anomalous low pressure over the Aleutian Low and higher pressure over Canada and around Hawaii. The PNA response during an MJO events modifies the strength of the Pacific jet and transports the MJO signal to higher latitudes. Using model experiments Ferranti et al. (1990 [16]) show that extratropical forecasts 11-20 days ahead are improved when the tropical regions are relaxed to the true conditions at every timestep. In these experiments they focused again on different OLR conditions associated with different MJO phases, showing that there is an important connection from the tropics that impacts the forecasts in the northern mid- and high-latitudes.

Cassou (2008 [10]) expanded on this analysis by linking MJO phases to specific North Atlantic regimes 10-15 days after the MJO. They find that in the NDJFM (November-March) months between 1974 and 2007, 10 days after phase 3 of the MJO, the occurrence of an NAO+ is increased by 60%, while the occurrence of NAO- is 40% lower. For phase 6 of the MJO, they find the opposite with a 70% higher occurrence of NAO- and a slightly lower number of NAO+ (Figure 3 in Cassou, 2008 [10]). These two phases of the MJO show the opposite signal in the Indian Ocean, while there is strong convection in phase 3, there is subsidence in the same region in phase 6 (Figure 1 and Cassou, 2008 [10] their Figure 2). The fact that these opposite signals over the Indian Ocean align with opposite anomalies over the North Atlantic, strengthens the hypothesis that certain phases of the MJO influence the NAO.

Analysing composites from different MJO phases (again phase 3 and phase 6) over North America and the North Atlantic, Cassou (2008 [10]) find different responses of the northern mid- to high-latitudes to different MJO phases (Cassou, 2008 [10] their Figure 4). After phase 3 MJO, they find a Rossby wave train from the Pacific, crossing North America and entering the North Atlantic storm track. This anomalous wave is connected to anticyclonic synoptic-scale wave breakings that are associated with NAO+. After a phase 6 MJO, they find no wave travelling eastward and a

reduction in anticyclonic wave breaking leading to a higher chance of NAO-.
The results from the mentioned papers of the MJO teleconnection to the NAO shows that the Indian Ocean region can excite teleconnections to the North Atlantic that influence the weather in Europe. Of special importance for these teleconnections are a Rossby wave train from the Indian Ocean and the interaction with the mid-latitude jet. On seasonal timescales (DJF average) the effects of the MJO average out. The results from this thesis will show that the teleconnection mechanisms that are important on the sub-seasonal timescales also present on seasonal teleconnections and form a link between Indian Ocean and North Atlantic.

2.3 Background conditions of 2019/2020 in ERA5

This section discusses the state of the autumn and winter 2019/2020. I use ERA5 to show the most prominent anomalies and introduce the phenomena that I will focus on in this thesis.

2.3.1 Tropical anomalous conditions

Anomalous tropical conditions can have a large influence on the extratropical climate on seasonal timescales (Hoerling and Kumar, 2002 [29]). In the autumn (SON) and winter (DJF) of 2019/2020 a strong tropical anomaly developed in the Indian Ocean (Wang et al., 2020 [84]). Warmer than average temperatures in the western Indian Ocean and colder temperatures in the east established an IOD event in autumn. In the west, a horseshoe pattern of high SSTs is contrasted by a strong negative SST anomaly in the east (SON Figure 2.2). The negative SST anomaly stretches from the Indian Ocean into the Pacific, but is strongest in the Indian Ocean off the coast of Sumatra. The IOD index (defined as the SST difference between the black boxes in Figure 2.2) was in a very positive state in this autumn (IOD index of ≈1.4 (e.g. ECMWF's DMI index 2019/2020: https://charts.ecmwf.int/products/seasonal_system5_climagrams_sst?base_time=201908010000&index_type=Indian%20Ocean%20Dipole)).
The other tropical ocean basins show smaller and less coherent anomalies (especially ENSO is in a neutral/weak positive state (NOAA ENSO index: https://origin.cpc.ncep.noaa.gov/products/analysis_monitoring/ensostuff/ONI_v5.php)).
The SST heating dipole in the Indian Ocean is connected to the region of strongest convection and precipitation (see Introduction IOD 2.1.2). Considering the precipitation anomaly (Total Precipitation (TP)), the dipole in the Indian Ocean is even more

pronounced than the SST dipole (Figure 2.2). Here, the Indian Ocean region shows by far the largest anomalies with more precipitation in the west and a dry anomaly in the east. Again, the dry anomaly stretches across the Maritime Continent, but the strongest anomaly is centred over the eastern Indian Ocean. The Pacific basin shows only a weak precipitation anomaly that resembles a northward shifted ITCZ. Over the Atlantic, similar to the SST, no large precipitation anomalies are observable. Upper level divergence (here D200 Figure 2.2) is a more direct indicator for tropical upper level dynamics and is closely related to convection. In the tropics, the D200 anomalies reflects the previously described signals of SST and precipitation. The increased SST and precipitation over the western Indian Ocean is reflected by anomalous upper level divergence, with more convergence centred in the cold and dry regions of the eastern Indian Ocean. The other tropical ocean basins show less strong and coherent signals compared to the Indian Ocean. Considering these variables, the extratropics show less strong and coherent anomalies in SON 2019. A more in depth look into the Northern Hemisphere extratropical anomalies in the winter is in section 2.3.2.

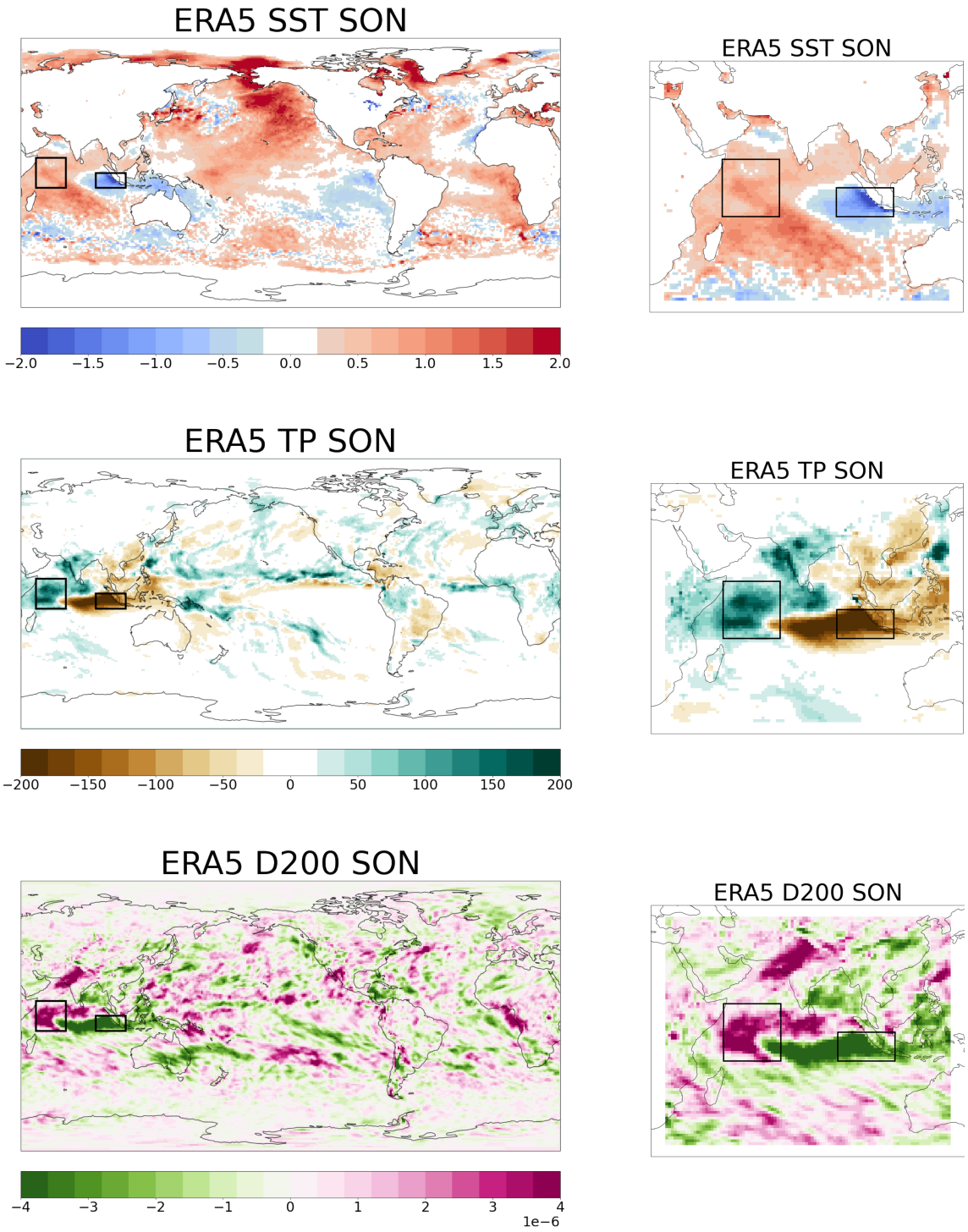


Figure 2.2: **Anomalous conditions in SON 2019** in ERA5. **Left** for global conditions and **Right** for the Indian Ocean region. **Top** is SST [K], **Middle** is TP [mm/month], **Bottom** is D200 [1/s]. Black boxes indicate the two regions used to define the IOD index. Anomalies are calculated against the 1981-2020 climatological average.

As the IOD typically has its greatest amplitude in SON (e.g. Webster 2020 [86]), the strength of the IOD is expected to weaken in DJF. Still, the IOD of 2019/2020 lasted into winter with a dipole still clearly visible in the seasonal DJF average of precipitation and upper level divergence (Figure 2.3).

In the DJF average the SST dipole pattern of the IOD is much weaker with only slightly higher temperatures in the west than in the east (Figure 2.3). Compared to the autumn, a main difference in the Indian Ocean SST is the absence of the cold anomaly in the eastern Indian Ocean. While the positive SST anomaly in the west stayed similar, and even increased, the cold anomaly in the east is warmed into a positive anomaly. Even though the SST dipole in DJF is much weaker, the dipole still exists in the precipitation (Figure 2.3). A large area in the western Indian Ocean shows anomalously large amounts of precipitation (and convection), while the precipitation over the Maritime Continent is suppressed. This is supported again by the upper level divergence (D200 Figure 2.3) that shows the divergence over the western Indian Ocean and convergence over the Maritime Continent.

Over the tropical Pacific, some El-Niño-like precipitation is evident with positive precipitation anomalies shifted towards the central Pacific and subsidence over the Maritime Continent. Since the SST anomaly in the Pacific is smaller than a typical El Niño (Niño3.4 ≈ 0.5°C including warming from climate change (NOAA ENSO index: https://origin.cpc.ncep.noaa.gov/products/analysis_monitoring/ensostuff/ONI_v5.php)), some of the atmospheric El Niño signal in 2019/2020 is likely linked to the strong IOD and their shared centre of action over the Maritime Continent. The potential teleconnections from the anomalies over the Pacific are further discussed in this thesis (chapter 5.2).

In the tropical Atlantic sector, the precipitation and divergence anomalies are again small in DJF, despite the SST anomalies being very positive. This indicates that the teleconnections from the tropical Atlantic are likely not strong, this is further investigated in ERA5 teleconnections and model experiments (OpenIFS model experiments 5.2).

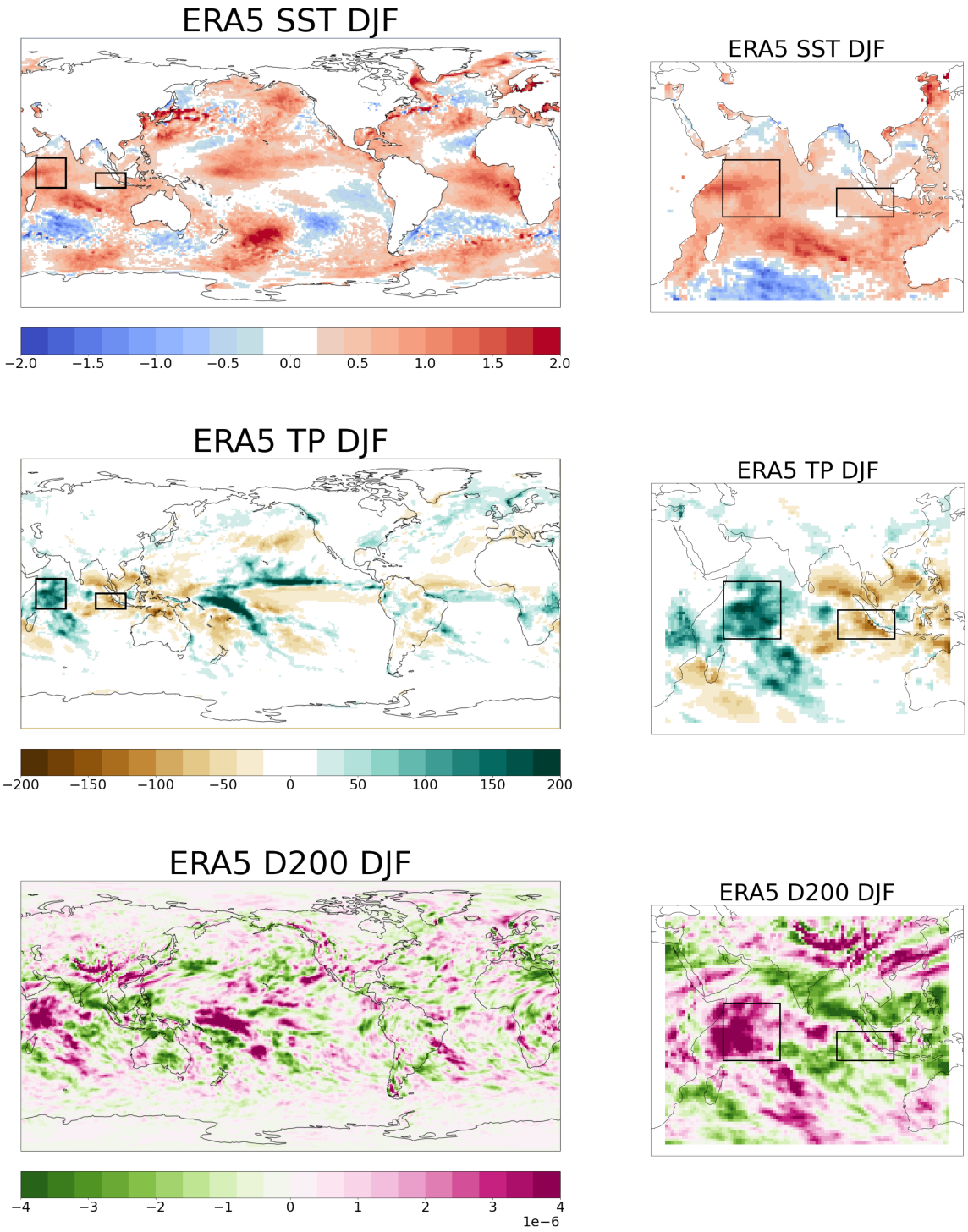


Figure 2.3: **Anomalous conditions in DJF 2019/2020** in ERA5. **Left** for global conditions and **Right** for the Indian Ocean region. **Top** is SST [K], **Middle** is TP [mm/month], **Bottom** is D200 [1/s]. Black boxes indicate the two regions used to define the IOD index. Anomalies are calculated against the 1981-2020 climatological average.

2.3.2 Northern Hemisphere anomalous conditions

In the winter 2019/2020, not only the tropics were in an anomalous state, but also the extratropics with strong signals over the entire Northern Hemisphere. A special focus is placed on the seasonal climate over the North Atlantic and Europe, which was in a particular warm and wet state (Hardiman et al., 2020 [27]).
First, I investigate the ERA5 geopotential height at 500 hPa (Z500 Figure 2.4 a) and the meridional wind at 200 hPa (V200 Figure 2.4 b). In DJF 2019/2020 the Arctic Oscillation (AO) was in a very positive state. The Z500 anomalies (Figure 2.4 a) show a strong coherent negative anomaly over the pole with especially negative centres over Greenland, north- eastern Europe and Alaska. Meanwhile, the mid-latitudes are characterised by strong positive Z500 anomalies spanning most longitudes. These positive anomalies are centred over Japan, south of Alaska, the east coast of North America, and south- western Europe. Only over central and western Asia some deviations from this annular structure are detectable. Over the Arabian peninsular and northern India some negative Z500 anomalies are evident. Together the general high over the lower latitudes and the low at the higher latitudes form a positive AO in this winter that is especially pronounced in the North Atlantic sector. The strong meridional gradient over the Atlantic and the resulting positive NAO had a large influence on the winter weather in Europe by increasing the heat and moisture transport from the Atlantic towards northern Europe (see below).

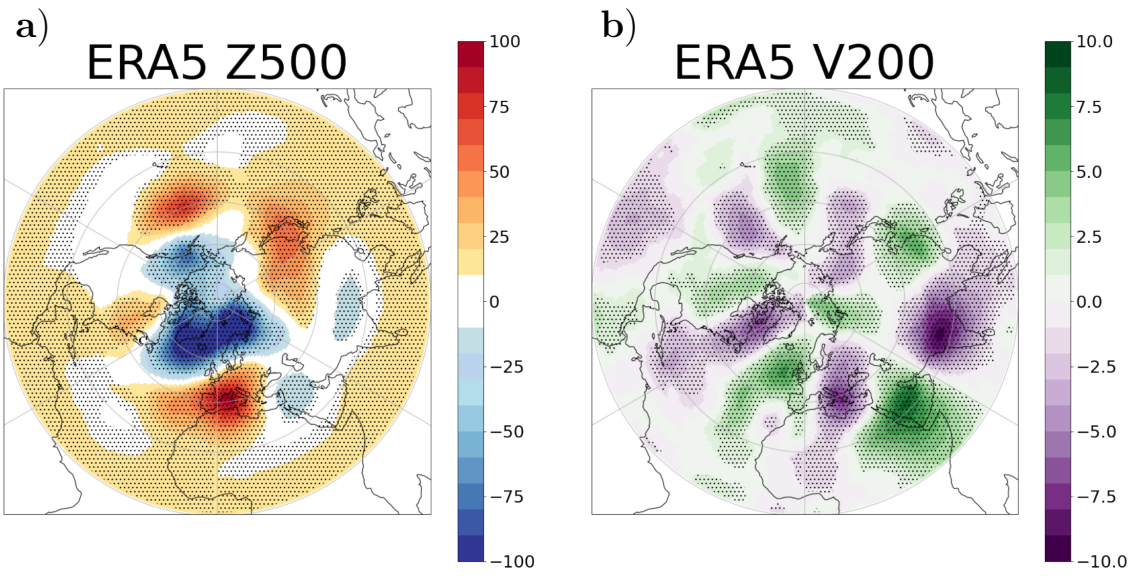


Figure 2.4: **Northern Hemisphere anomalies in DJF 2019/2020** in ERA5. **a)** Z500 [m] and **b)** V200 [m/s]. Anomalies are calculated against the 1981-2020 climatological average. Stippling denotes significant areas calculated with a 2-sided Student's t-test at 5%

At the same time, a strong quasi-stationary Rossby wave train is evident in the upper tropospheric meridional winds (V200), crossing most of the mid-latitudes. The connection of this wave train to the NAO has been investigated by Hardiman et al. (2020 [27]). They show in model experiments that reversing the strong SST dipole in the Indian Ocean also removes the wave train and reverse the positive AO signal. This wave train will be further discussed in this thesis as a teleconnection mechanism between the Indian Ocean dipole and the NAO (Rossby wave train teleconnection).

The strong positive NAO led to an exceptional winter in Europe as all of Europe experienced temperatures well above the climatological average (even with the linear trend from climate change removed) (T2M Figure 2.5 a). As a whole, Europe experienced its warmest winter on record (Hardiman et al., 2020 [27]). This temperature anomaly is weakest over the British Isles and Iberia, and stronger over Scandinavia. Even though there are local differences, the signal is still consistent positive over all of Europe. The temperature signal over Europe corresponds to a strong positive NAO (see Z500 anomalies), which brings milder winter air from the Atlantic (especially to norther Europe).
The precipitation anomaly over Europe shows a similar impact of the NAO with a North-South divide (TP Figure 2.5 b). While northern Europe has increased pre-

cipitation, southern Europe and the Mediterranean area are dryer than usual. The strongest precipitation anomalies are over Norway with a strong positive signal and around Italy with a strong negative signal. The precipitation and temperature anomalies of the 2019/2020 winter in Europe are close to the canonical expected NAO signal (e.g. MetOffice NAO description: https://www.metoffice.gov.uk/research/climate/seasonal-to-decadal/gpc-outlooks/ens-mean/nao-description)

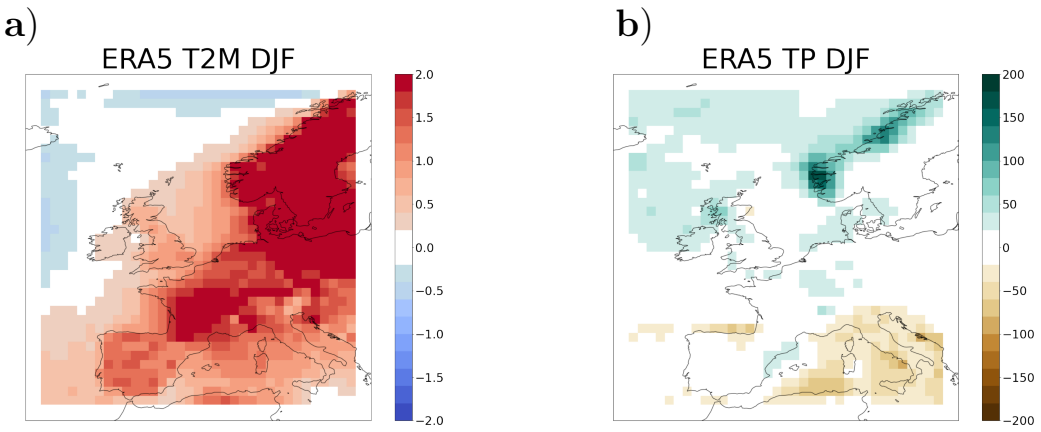


Figure 2.5: **European anomalies in DJF 2019/2020** in ERA5. **a)** 2 metre temperature [K] and **b)** total precipitation [mm/month]. Anomalies are calculated against the 1981-2020 climatological average. Stippling denotes significant areas calculated with a 2-sided Student's t-test at 5%.

Chapter 3

Methods

This chapter describes the methods, models, and data sets I use in this thesis. The methods here detailed are used throughout the thesis if not otherwise specified.

3.1 OpenIFS model

I am using ECMWF's OpenIFS model in this thesis to investigate the boreal winter conditions. All model experiments are started on the first of November and run until the first of March of the following year. The ocean boundary conditions are daily varying ERA5 SST and Sea Ice conditions of the investigated year. To obtain a climatological average of the OpenIFS model I conduct hindcasts experiments. These hindcasts consist of 5 ensemble members in every year between 1981-2020. This gives me a set of 200 members*years as a model climatology. I conduct a control forecast for 2019/2020 with 100 members, while all experiments are conducted with 25 members each.

The OpenIFS is a uncoupled model built on a slightly older version of the operational integrated forecasting system (IFS) from ECMWF. A full description of the OpenIFS can be found from ECMWF here: https://confluence.ecmwf.int/display/OIFS/OpenIFS+User+Guide. The model cycle of the OpenIFS I am using is 43r3 with a resolution of TL159L60. The TL159 reduced linear grid has a horizontal resolution that is equivalent to 1.125°. More information about the horizontal structure can be found here: https://confluence.ecmwf.int/display/OIFS/4.3+OpenIFS%3A+Horizontal+Resolution+and+Configurations. In the vertical the model is unevenly split into 60 levels with the lowest at 1013 hPa and the highest at 0.2 hPa. A detailed description of the model levels can be found here: https://confluence.ecmwf.int/display/UDOC/L60+model+level+definitions.

The ensembles are created through the combination of initial condition perturbations

and Stochastically Perturbed Parametrisation Tendencies (SPPT; Buizza et al., 1999 [7]; Palmer et al., 2009 [61]). Singular vectors are used to create the perturbed initial conditions (Leutbecher and Palmer, 2008 [43]). All model runs are initialised on the 01.November and run the NDJF season. After ≈30 days the variance of the ensemble plateaus having reached its maximum spread (not shown). Different regions of the globe are differently impacted by initial condition perturbations and SPPT. In the tropics the IC perturbations are small and the SPPT has a large impact on the variance growth of the ensemble. In the extratropics the IC perturbations are larger than in the tropics and the variance grows much faster from them, while the SPPT is the same in the extratropics and in the tropics. In the experiments discussed in this Thesis I use the combination of IC perturbation and SPPT to achieve the best ensemble spread.

For an even larger control forecast, I use the OpenIFS@Home. The OpenIFS@Home is part of the "ClimatePrediction.net" (ClimatePrediction.net webpage: https://www.climateprediction.net/). Their system of distributed computing allows the computation of a large ensemble simultaneously on home computers. This reduces the computing costs for large ensembles by a lot. However, it does not reduce the storage space needed for the post-processing and later analysis of the ensemble. A notable difference between the OpenIFS@Home experiment and the local Oxford experiment is that it was not feasible to create 2000 different IC perturbations for the OpenIFS@Home ensemble. Instead, I use 200 different IC perturbations with 10 different SPPT sets for each of the IC perturbations to create the 2000 member ensemble. In all other aspects, the OpenIFS@Home experiment is designed to be as similar as possible to the Oxford run OpenIFS control experiment. A direct comparison between the Oxford OpenIFS control experiment and the OpenIFS@Home is not possible, since the forecasts are not bit reproducible on different machines. A statistical analysis of the results shows that the OpenIFS@Home and the Oxford control OpenIFS are very close to each other.

3.2 OpenIFS sensitivity experiments

I created the OpenIFS experiments using the Initial- and Boundary-Conditions from the OpenIFS control forecast, ERA5, and ECMWF's Metview tool (https://confluence.ecmwf.int/display/METV/Metview). Metview is able to work with ECMWF's GRIB fields, which the model requires as input. Additionally, Metview is able to read and write reduced gaussian grids which some of the boundary condition

files use.
As an example I will describe the creation of the Indian Ocean only experiment (see results of this experiment in OpenIFS experiments 5.2):
For this experiment I only perturb the boundary conditions the model is using. I load the BC used from the control experiment (hnw4) into Metview (ICMCLhnw4INIT) and overwrite the SST and Sea Ice (CI) conditions (of the first day) everywhere with a climatological average from ERA5 (from that specific day). Afterwards I add the control experiment SST (and CI) conditions in the Indian Ocean region back to the file with a 5° relaxing boundary. The boundary is necessary to prevent sharp edges in the BC. I repeat this process for every time step of the BC forcing (1 day forcing frequency). As the last step I save and rename the new experiment with a new experiment ID (ICMCLhnx3INIT). For this experiment all other conditions (atmospheric IC, land IC, external forcing) stay the same as in the control experiment. Since all ensemble members share the same BC, this process only needs to be done once for the BC perturbation experiments.
Experiments with different IC, work similarly, with the added complication that the process needs to be repeated for every ensemble member to retain the IC ensemble perturbation.

3.3 ECMWF model overview

This section gives an overview over the ECMWF model setup used in this Thesis. This does not replace the specific information given in individual chapters, but serves as a general overview on the model components.

Name	Resolution	ensemble size	cycle	coupling	Ocean model	start date	BC perturbations	IC perturbations
SEAS5	TCO319L91	51	43r1	single executable	NEMO ORCA025z75	01.11.	No	No
uncoupled SEAS5	TCO319L91	25	43r1	No	ERA5 BC	01.11.	No	No
OpenIFS control	TL159L60	100	43r3	No	ERA5 BC	01.11.	No	No
OpenIFS hindcast	TL159L60	5	43r3	No	ERA5 BC	01.11.	No	No
OpenIFS experiments	TL159L60	25	43r3	No	ERA5 BC	01.11.	SST and CI	Only chapter 9 Table 9.1

Table 3.1: **ECMWF model overview**. Information about SEAS5 and the uncoupled SEAS5 from Stockdale et al., 2018 [73]., Johnson et al., 2019 [37]. and Mogensen et al., 2012 [53].

The SEAS5 and uncoupled SEAS5 generally share the same characteristics with the difference of the coupling and the lower ensemble member number in the uncoupled SEAS5. The information here for SEAS5 and the uncoupled SEAS5 is the same for their respective hindcasts between 1981-2020 and the winter 2019/2020. For the OpenIFS, the hindcast between 1981-2020 has 5 ensemble member, but generally the same setup as the forecast of 2019/2020 with 100 ensemble members and ERA5 IC and BC (called here control forecast). The individual OpenIFS experiments have differing BC and IC perturbations, but are conducted with the same model as the control experiment and 25 members each.

3.4 Significance calculation

To test the significance of the anomalies in ERA5 I am using a Student's t-test with a 5% limit (Wilks, 2019 [90]). The significant values obtained with this method are statistically different from the climatological distribution at the 5% level.
For model ensemble runs and composite analyses I am using a two sided bootstrapping test with 1000 iterations with a 5% limit (Wilks, 2019 [90]). To test significance, I select random ensemble members from random years of the hindcast period until I have a new "ensemble" with with same size I wish to test. From this new "ensemble" I create a new "ensemble mean". This process is repeated 1000 times and the real ensemble (the one that is to be tested) is ranked within the 1000 ensemble means (every grid point individually). If the anomaly from the real ensemble is in the top or bottom 2.5%, the grid point is classified as significant. This shows the regions where the real ensemble mean is to 5% likelihood not due to a random selection and where the composite selection is likely due to a physical connection.
As a comparison, I used a Student's t-Test with a 5% limit for the model ensembles as well, but I found that bootstrapping gave me a better understanding of the uncertainty of the variables involved.

3.5 E-Vectors

To determine the strength of the interaction between short lived eddies and the mean flow, I am using the E-Vectors described in Hoskins et al. (1983 [32]) and Equation 3.6. The E-Vectors are based on the Eliassen-Palm flux (e.g. Andrews and McIntyre 1976 [3]), but can be used on time averages three dimensional fields. To derive the E-Vectors, Hoskins et al. (1983 [32]) start with the horizontal velocity correlation

tensor **C**, separated into the isotropic and anisotropic parts.

$$\mathbf{C} = \begin{pmatrix} \overline{u'^2} & \overline{u'v'} \\ \overline{u'v'} & \overline{v'^2} \end{pmatrix} = \begin{pmatrix} K & 0 \\ 0 & K \end{pmatrix} + \begin{pmatrix} M & N \\ N & -M \end{pmatrix} \tag{3.1}$$

with

$$K = \frac{1}{2}(\overline{u'^2 + v'^2}); M = \frac{1}{2}\overline{u'^2 - v'^2}; N = \overline{u'v'} \tag{3.2}$$

where K is the eddy kinetic energy. Here the two parts (M and N) of the later E-Vectors are evident. u and v, the zonal and meridional wind at a level (here 200 hPa), respectively. Primes (u') denote 2-6 day bandpass filtered data calculated using a Lanczos filter [90]. Overbars ($\overline{u}$) denote the seasonal average. With the eddy vorticity $\zeta' = v'_x - u'_y$ and with non-diverging eddies, the eddy vorticity can be written as:

$$\overline{v'\zeta'} = (-M_y + N_x, -M_x - N_y) \tag{3.3}$$

The divergence of this can be written as:

$$\nabla \cdot \overline{v'\zeta'} = (-2M_{xy} + N_{xx} - N_{yy}) \tag{3.4}$$

If we then assume that the eddies are elongated in the meridional direction (which is the case for the high frequency eddies), we can neglect N_{xx} resulting in:

$$\nabla \cdot \overline{v'\zeta'} = (-2M_{xy} - N_{yy}) = \partial_y \nabla \cdot \mathbf{E} \tag{3.5}$$

or

$$\mathbf{E} = (-2M, -N) = (\overline{v'^2 - u'^2}, -\overline{u'v'}) \tag{3.6}$$

Since the mean absolute vorticity (ξ) can be written as:

$$(\partial_t + \overline{v} \cdot \nabla)\xi + f\overline{D} + \nabla \cdot \overline{v'\zeta'} = \mathbf{k} \cdot \nabla \times \overline{\mathbf{F}} \tag{3.7}$$

With the divergence (D), the frictional force (F). The E-Vectors appear as a momentum flux in this equation (as the $\nabla \cdot \overline{v'\zeta'}$).

Equations are from Hoskins et al. (1983 [32]). In general a diverging E-Vector field is equivalent to energy flux from the eddies into the mean flow, while convergent fields show areas where eddies decrease the westerly mean flow. Drouard et al. (2013 [15]) show how the E-Vectors are associated with the latitude of the North Atlantic jet and the phase of the NAO (especially the meridional component of the E-Vectors). While Rivière and Drouard (2015 [64]) show in two different winters the how eddy,

mean-flow interactions in the North Pacific can precondition the North Atlantic jet into a certain phase.

3.5.1 Eddy feedback

An alternative way of calculating the interaction between the eddies and the mean flow jet is to calculate the eddy feedback parameter (EFP) as shown in Hardiman et al. (2022 [26]). The calculation of the EFP is again based on the Eliassen-Palm flux (Andrews and McIntyre 1976 [3]). Following Hardiman et al. (2022 [26]) I calculate the eddy zonal acceleration first (their equation 1) using 200 hPa daily wind data from 1981-2020.

$$\frac{\nabla \cdot \mathbf{F}_H}{\rho a \cos\phi} = \frac{d(\overline{u'v'}\cos(\phi)^2)}{d\phi} \tag{3.8}$$

Where ρ is the density, a is the Earths radius, and ϕ is the latitude. This zonal acceleration parameter is calculated from the daily wind data at 200 hPa in the DJF season 1981-2020. To obtain the u' and v' one can either subtract the zonal average from the full wind or use a high pass filter. I compared a 2-6 day band pass filter to the zonal mean method and fund only very minor differences. Because the calculation is quicker and the one used in Hardiman et al. (2022 [26]), the calculation shown are the ones with the zonal mean removed. The daily deviations from the average are then averaged over the DJF season. To calculate the EFP from this eddy acceleration, specific areas are averaged (discussed in chapter 8.1) and correlated (over time) with the zonal mean jet in these regions. The squared correlation is the EFP in the data set. This calculation acts as a divergence calculation of the meridional part of the E-Vectors discussed above.

Chapter 4

Forecasts of 2019/2020

In this chapter I discuss the forecasts of the winter 2019/2020 from multiple seasonal forecasting models and compare them to ERA5. Of particular interest is the high agreement between many of these forecasting models (and ERA5) in the 2019/2020 DJF season, with most models being able to accurately reproduce the main features. Of special note is the very accurate forecast of Z500. This uncommon agreement between the models is an indication of a predictable component in the climate system that well represented in the models.

First the ECMWF's SEAS5, the uncoupled SEAS5, and the OpenIFS control forecast are discussed and compared to the forecast skill of these models to other years. Afterwards other seasonal forecast models are discussed to get a broader view of different forecasts for this winter.

4.1 ECMWF model forecast

The winter 2019/2020 forecasts of the ECMWF models (SEAS5, uncoupled SEAS5, and OpenIFS control) is compared to the hindcast period of 1981-2020. In the following, I call the OpenIFS run with initial conditions and boundary conditions from ERA5 the "control forecast". For each model, the ensemble mean from 2019/2020 is compared to the ensemble mean from the other years of the hindcast period. It has to be noted here that a higher forecast skill in the OpenIFS is expected for the winter 2019/2020 since the number of ensemble members is larger (e.g. Scaife and Smith, 2018 [70]).
The Z500 fields from the models are evaluated first to get a overview of the mid-tropospheric forecast. The forecast skill is separated into three parts, namely:

- For the entire globe.
- For the Northern Hemisphere extratropics (north of 30°N)
- For the Southern Hemisphere extratropics (south of 30°S)

The forecast skill is evaluated as weighted field correlations between the different models and ERA5. Additionally, I rank the field correlation from the winter 2019/2020 to all other 40 years in the hindcast period of each model to give context of how good the forecast is compared to other years. So the rank is x/40, means the 2019/2020 forecast is the x best out of the 40 years.

Region/Model	SEAS5	uncoupled SEAS5	OpenIFS
Global	0.70 (05/40)	0.72 (06/40)	0.72 (04/40)
NH extratropics	0.64 (05/40)	0.68 (06/40)	0.81 (02/40)
SH extratropics	0.79 (03/40)	0.75 (06/40)	0.75 (04/40)

Table 4.1: **ECMWF model forecast skill of Z500** in DJF 2019/2020 and comparison to the hindcast 1981-2020 period. **Top** row globally, **Middle** row Northern Hemisphere extratropics (30-90°N), and **Bottom** row Southern Hemisphere extratropics (30-90°S).

The forecasts for the winter 2019/2020 are good across the different models and hemispheres compared to many other years of the hindcast period (top $\sim 10-15\%$). The OpenIFS and uncoupled SEAS5 show slightly better global skill due to them having observed SST boundary conditions, but this winter is also one of the best forecasted years in SEAS5 (Table 4.1). This high agreement between models and ERA5 is especially noteworthy, since there was no ENSO event in 2019/2020, which is usually associated with a very high extratropical forecast skill (Sharmila et al., 2023 [71]). For example, the winter 1997/1998 that had the strongest El Niño event in the hindcast period, also has the highest forecast skill, with a global field correlation between the models and ERA5 of ~ 0.9.
Compared to the global forecast, the Northern Hemisphere extratropics are forecasted slightly worse in both SEAS5 and uncoupled SEAS5, but still in the top 15%. Again, the OpenIFS and uncoupled SEAS5 show a slightly higher skill, showing that the information of the exact SST and Sea-Ice conditions helps the forecast accuracy. For the OpenIFS, this is the second best forecast in the hindcast period (inflated due to the large ensemble size). The higher correlation in the OpenIFS compared to the SEAS5 and uncoupled SEAS5 is caused by the slightly better forecast of the centres of action of the Z500 field. The Z500 anomalies in all models, shows a spatially high

agreement with ERA5 (Figure 4.1). The lower amplitude of the anomalies in the models is expected due to the forecasts being ensemble means, while ERA5 is just one realisation (Scaife and Smith, 2018 [70]). The positive anomaly over the tropics is partially related to the non-linear aspect of climate change. Over the Northern Hemisphere extratropics, all models and ERA5 show a positive Arctic Oscillation with the NAO being in a strong positive phase as well. A major difference between SEAS5 and ERA5 is that SEAS5 (Figure 4.1 b) shows different anomalies over the central and east Pacific. Where ERA5 (Figure 4.1 a), the uncoupled SEAS5 (Figure 4.1 c) and the OpenIFS (Figure 4.1 d) shows a positive anomaly over the Aleutian cyclone area, SEAS5 shows a negative anomaly extending towards the pole. This difference has large implications for the teleconnections in SEAS5 and will be further discussed in chapter [Rossby wave train 7].

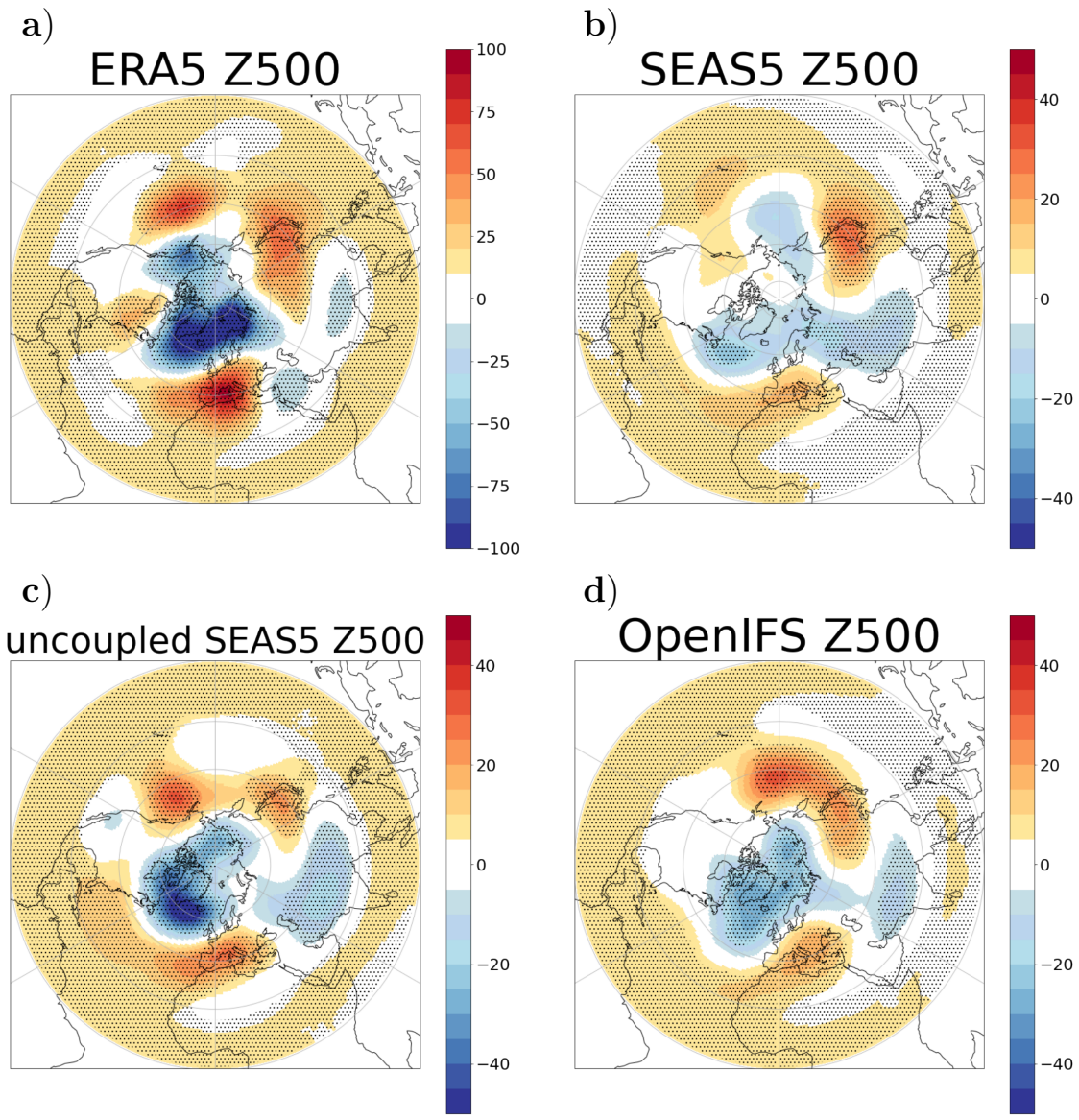


Figure 4.1: **Z500 from ECMWF models in DJF 2019/2020** compared to ERA5. **a)** ERA5, **b)** SEAS5, **c)** uncoupled SEAS5, **d)** OpenIFS control forecast [m]. Anomalies are calculated against the 1981-2020 climatological average. ERA5 stippling denotes significant areas calculated with a 2-sided Student's t-test at 5%. Model stippling denotes significance and is calculated with a 2-sided bootstrapping at 5%.

For the North Atlantic regions it is evident that the ensemble mean of both the OpenIFS and SEAS5 model manage to capture the positive NAO. However, the magnitude of both ensemble means is lower than the one of ERA5. To show that this is not a general bias and that ensemble members exist with an NAO of the correct (or greater) magnitude I investigated the NAO from Z500 in each ensemble member of the OpenIFS control forecast and SEAS5 (Figure 4.2). It is evident that

many ensemble members of both the OpenIFS and SEAS5 show a too weak (or even negative) NAO, but it is also clear that some members from both models manage to capture (or exceed) the strong positive NAO. The ensemble mean NAO (dashed lines in Figure 4.2) shows a much lower NAO index in both models (but in the correct positive phase) compared to ERA5 (cyan line). This is in agreement with the fields of Z500 depicted in Figure Figure 4.1, where both models showed a positive NAO with a lower magnitude. The large spread of the ensemble is expected in a under-confident region like the North Atlantic, but the fact that individual members of both models captured the real strength of the NAO is good for the confidence in these forecasts. The lower magnitude of the ensemble is not desirable, but common for extratropical (especially North Atlantic) forecasts. This phenomenon is linked to the signal to noise paradox discussed in Scaife et al. 2018 [70].

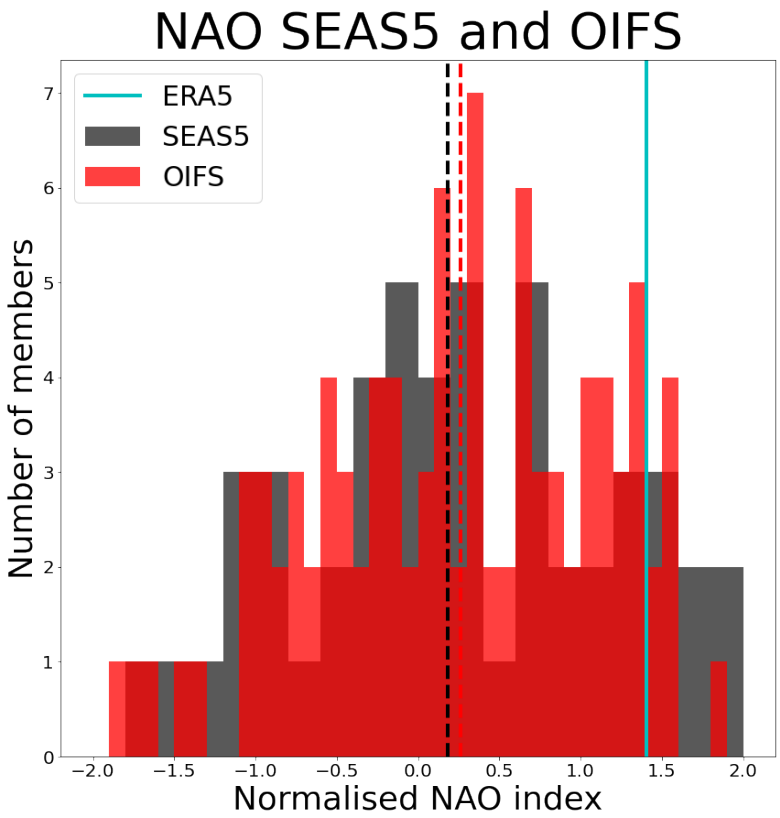


Figure 4.2:
NAO in 2019/2020 in OIFS and SEAS5 members compared to ERA5. The normalised NAO index is calculated from the Z500 difference between a northern and southern region of the North Atlantic. The northern region is defined as $60 - 80°$N and $10 - 40°$W and the southern box as $30 - 50°$N and $10 - 40°$W. Dashed lines indicate the ensemble mean and the cyan line indicates the ERA5 NAO. Anomalies are calculated against the 1981-2020 climatological average.

4.2 C3S model forecast performance

Since all the models described here are from ECMWF and are built from the same base, it is important to evaluate the forecast of 2019/2020 from other models as well. For this purpose I use the Copernicus C3S models (namely UKMO, DWD, CMCC, Météo-France) (C3S Documentation and Data: https://confluence.ecmwf.int/display/CKB/C3S+Seasonal+Forecasts%3A+datasets+documentation). Since the common hindcast period of these models is 1993-2016, I compare the anomalies form 2019/2020 to this hindcast period (anomalies for ERA5 and SEAS5 redone for the 1993-2016 period).

The tropical rainfall (Total Precipitation TP) anomalies are generally well forecasted in the C3S models. The major signals in ERA5 are in the Indian and Pacific Ocean in DJF 2019/2020 (Figure 4.3 a). The Indian Ocean shows the strong positive IOD, while the Pacific has some positive precipitation anomalies in the western Pacific and north of the equator. The C3S multi-model-mean (MMM Figure 4.3 b), reproduces the clear positive IOD and the positive anomaly north of the equator in the Pacific. The major difference between the C3S MMM and ERA5 is the positive anomaly in the west Pacific that extends towards the south. In fact not just the MMM, but all seasonal forecast models miss this signal (compare all Figure 4.3). Another difference is the too strong north-south characteristic of the IOD in most forecast models, compared the more clear east-west signal in ERA5. The model that resembles ERA5 most in this aspect is the UKMO (Figure 4.3 d) that has a mostly east-west component. Nevertheless, the fact that these models manage to reproduce the strong positive IOD, is important for the origin point of the IOD teleconnection and a correct forecast of the Northern Hemisphere.

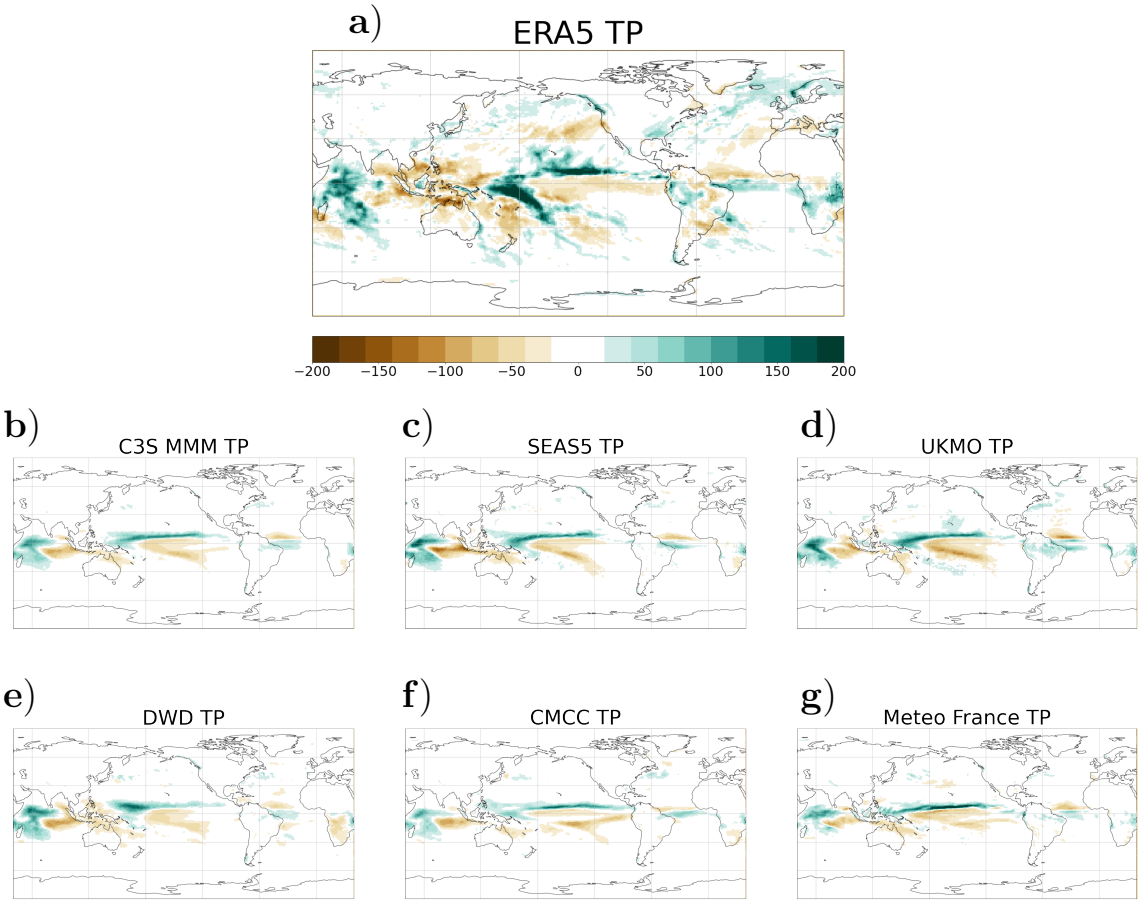


Figure 4.3: **TP from C3S models in DJF 2019/2020** compared to ERA5. **a)** ERA5, **b)** C3S multi-model mean, **c)** SEAS5, **d)** UKMO, **e)** DWD, **f)** CMCC, **g)** Météo France [mm/month]. Anomalies are calculated against the 1993-2016 climatological average. ERA5 stippling denotes significant areas calculated with a 2-sided Student's t-test at 5%. Model stippling denotes significance and is calculated with a 2-sided bootstrapping at 5%.

For the DJF season 2019/2020, most C3S models managed to forecast the positive AO/NAO (compare Figure 4.4). This high agreement between the different seasonal forecast models is uncommon and indicates mechanisms that are well represented in all of these models. The Z500 of the C3S multi-model-mean (MMM Figure 4.4 b) shows similar features compared to ERA5 (Figure 4.4 a). The negative anomaly over the North Pole and the polar North Atlantic is weaker compared with ERA5, but the AO and NAO are both still in a positive phase. As discussed for the ECMWF models, the smaller amplitude is due to the ensemble nature of the C3S, while ERA5 is just one realisation (Scaife and Smith, 2018 [70]). Individual ensemble members reproduce a similar strength AO/NAO signal as ERA5. One notable difference be-

tween the MMM and ERA5 is over Alaska. Where ERA5 shows a significant negative anomaly, the MMM shows a (not significant) positive anomaly. This difference becomes more evident when the individual models are compared to ERA5.
Most individual models are able to reproduce the positive AO well, with most of them also getting the NAO correctly. SEAS5 (Figure 4.4 c), UKMO (Figure 4.4 d), and Météo-France (Figure 4.4 g) all show a well forecasted positive NAO with positive anomalies over south western Europe and a negative center over- and to the south of Greenland. The forecast from DWD (Figure 4.4 e) still shows a positive NAO, but the negative centre extends too far towards Europe. One model that shows some incorrect results over the polar region is the CMCC (Figure 4.4 f), where the anomaly is slightly displaced and in the wrong phase (positive) over Greenland. The anomalies of CMCC are mostly insignificant over the polar regions and even though the subtropics are forecasted correctly (partly due to the non linear climate change signal), the NAO is not in a positive phase.
The models that reproduce the AO and NAO best are the UKMO and SEAS5, but even these models have some problems over Alaska. All these models fail to reproduce the negative Z500 anomaly over Alaska, with the UKMO (Figure 4.4 d) model coming closest with a mostly zero anomaly. The effects of this incorrect prediction over Alaska are further investigated in the chapter discussing the Rossby wave train.
Overall, the C3S models forecast the Northern Hemisphere well and there is a good agreement between the multi model mean and the ERA5 spatial patterns. This high forecast skill is likely related to strong tropical anomalies (in 2019/2020 the strong positive IOD). The C3S models do not only forecast the Northern Hemisphere well, but also the Southern Hemisphere with the strong negative SAM (all models except Météo-France forecast a negative SAM). The Southern Hemisphere anomaly is discussed in more detail in chapter [initial condition impact on the Southern Hemisphere 9].

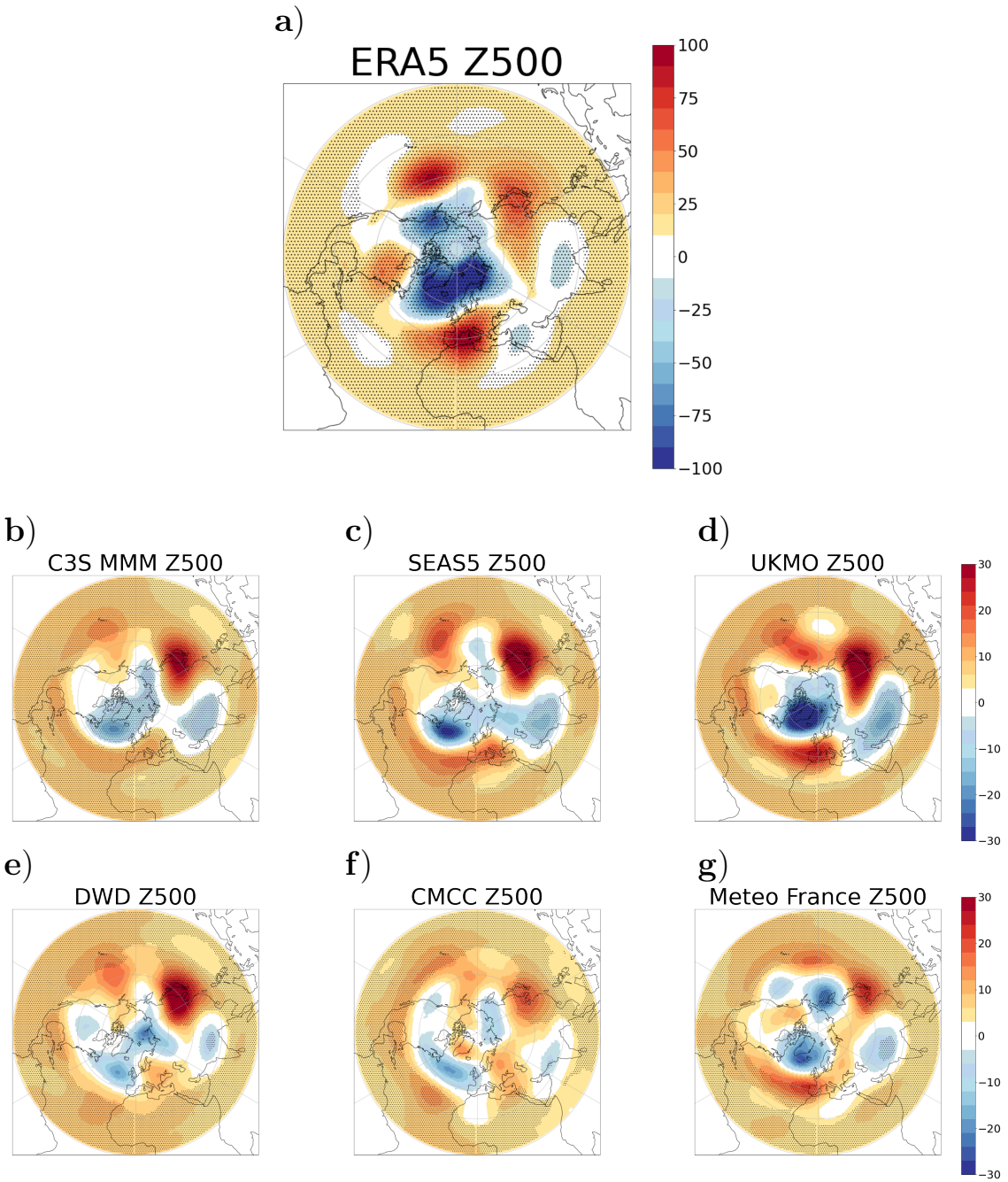


Figure 4.4: **Z500 from C3S models in DJF 2019/2020** compared to ERA5. **a)** ERA5, **b)** C3S multi-model mean, **c)** SEAS5, **d)** UKMO, **e)** DWD, **f)** CMCC, **g)** Météo France [m]. Anomalies are calculated against the 1993-2016 climatological average. ERA5 stippling denotes significant areas calculated with a 2-sided Student's t-test at 5%. Model stippling denotes significance and is calculated with a 2-sided bootstrapping at 5%.

Chapter 5

OpenIFS model experiments

Here, I investigate model experiments conducted with the OpenIFS to identify the atmospheric response to ocean conditions in 2019/2020. In a control experiment, I show that the OpenIFS is able to reproduce the major atmospheric features of 2019/2020. An experiment with only the 2019/2020 SSTs in the Indian Ocean region shows that these SSTs are enough to get a positive AO/NAO in the model. This is even the case when a linear climate change trend is removed from the SSTs. Interestingly, linear combinations of the ocean experiments yield different results to experiments with multiple ocean regions active, pointing to a non-linear atmospheric response to the ocean conditions.

5.1 OpenIFS control forecast

The previous chapter compared the Z500 of the OpenIFS control to ERA5, SEAS5, and the uncoupled SEAS5. It showed that the OpenIFS control does a good job reproducing the major Z500 features in 2019/2020. Here, I add to this analysis by investigating other tropospheric variables to have more confidence in the ability of the OpenIFS to reproduce the main features of the 2019/2020 winter. For this purpose I am using Z500, T850, TP as tropospheric measures and V200 as the measure of the quasi-stationary Rossby wave train (the stratospheric forecasts of SEAS5 and OpenIFS are discussed later in a separate chapter [Stratosphere in reanalysis and forecast 6]).

As discussed previously, OpenIFS forecast (middle column of Figure 5.1) of the Z500 field (top row) shows a high agreement with both ERA5 (left column) and SEAS5 (right column). The major features of the positive AO/NAO and the negative SAM are present in both models, albeit with lower magnitude than in ERA5 (ERA5 scale

is double the scale of the models due to the lower ensemble mean of the models (e.g. Scaife and Smith, 2018 [70])). In the NH both models manage to reproduce the positive height anomaly over Japan and Europe. The OpenIFS does a better job at correctly forecasting the height anomalies over the Aleutian region and the east coast of America. It also manages to reproduces the shape and strength of the negative anomaly more accurately. These deficiencies in SEAS5 are likely related to deficiencies in the quasi-stationary Rossby wave train in SEAS5 (this will be discussed further in chapter [Rossby wave train teleconnection 7]). In the Southern Hemisphere, both models reproduce the negative SAM, but the centre of the high anomaly is shifted westward from the Antarctic Peninsular towards the Ross Sea. Compared to other years, both models show a very accurate forecast of the Z500 field in DJF 2019/2020 (as discussed In chapter [Forecast skill of 2019/2020 4]).

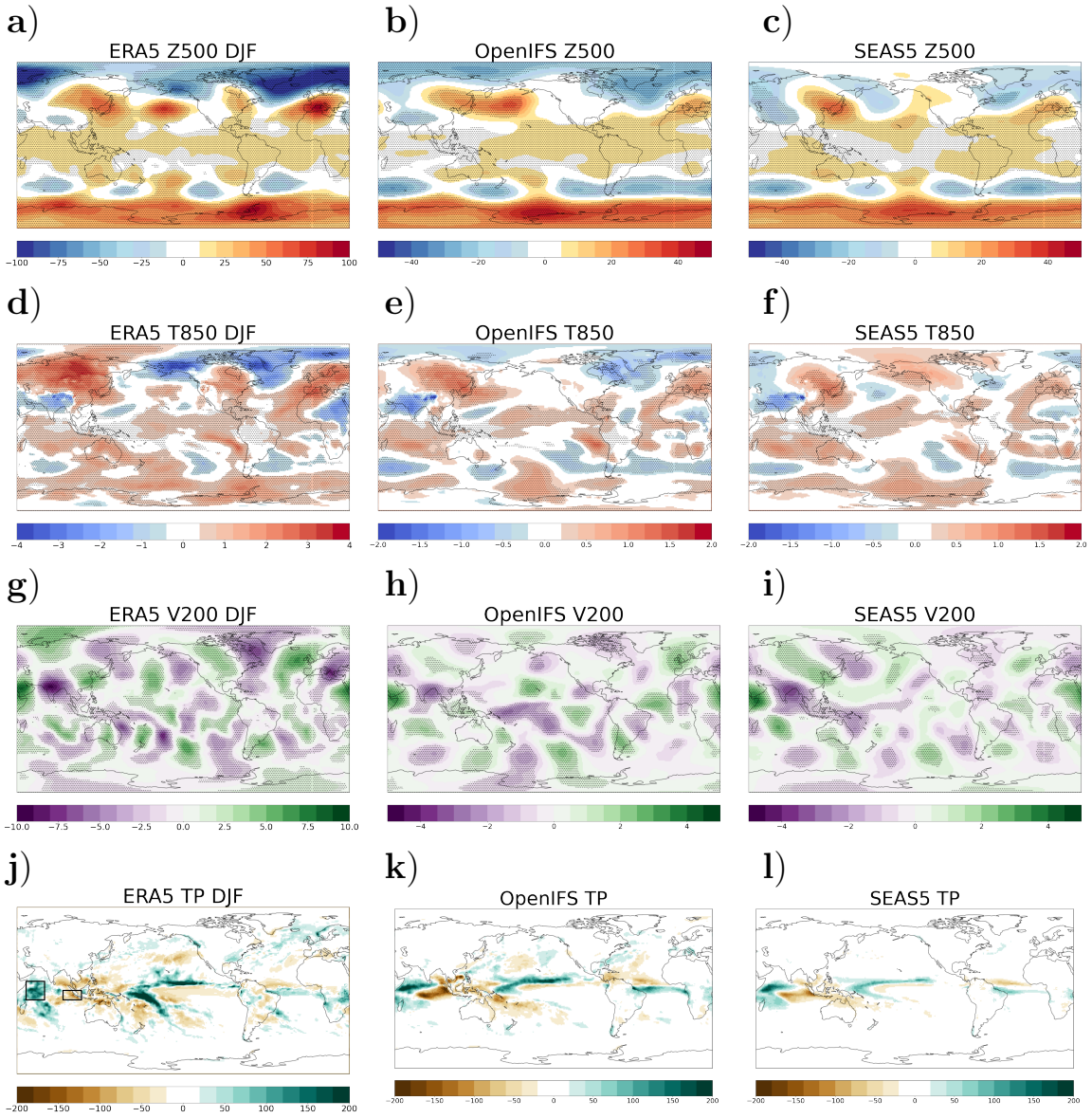


Figure 5.1: **OpenIFS comparison to SEAS5 and ERA5** in DJF 2019/2020. **Left** ERA5, **Middle** OpenIFS, and **Right** SEAS5. **Top** row Z500 [m], **Second** row T850 [K], **Third** row V200 [m/s], and **Bottom** row TP [mm/month]. Anomalies are calculated against the 1981-2020 climatological average. ERA5 stippling denotes significant areas calculated with a 2-sided Student's t-test at 5%. Model stippling denotes significance and is calculated with a 2-sided bootstrapping at 5%.

The temperature at 850hPa (T850, **second** row Figure 5.1) is used as another variable to evaluate the skill of the OpenIFS and SEAS5 forecasts compared to ERA5. The anomalies of the models in 2019/2020 generally agree well with the reanalysis. The most noticeable deviations (apart from the magnitude) are over Alaska and Antarctica in both models. Over Alaska the negative temperature anomaly in ERA5 has the

wrong sign in the models, with the models forecasting a positive anomaly instead. This difference over Alaska is likely related to the differences in the Z500 and wind fields between the models and ERA5. Over Antarctica, the positive T850 anomaly is smaller in the models than in ERA5 (even considering the ensemble mean) and shifted in longitude. Nevertheless, both models manage to forecast most of the T850 field of the 2019/2020 winter.

A quasi-stationary Rossby wave train is described in Hardiman et al. (2020 [27]) as the major teleconnection that connected the Indian Ocean to the NAO in 2019/2020. The wave train is evident in the V200 anomaly (**third** row Figure 5.1) in ERA5. Emanating from the Indian Ocean, ERA5 shows a pathway of the wave train crossing the North Pacific. Over the North Pacific, the wave train splits into a part that reflects towards the equator and a stronger part that crosses North America into the North Atlantic region. Over the North Atlantic, this second path projects onto the positive phase of the NAO.

The ensemble mean of the OpenIFS model (Figure 5.1 h) manages to reproduce some of the wave train, but the wave train over the Pacific and North America is shifted in latitude. This shift is likely connected to the incorrect forecast over Alaska (in Z500 and T850). The OpenIFS only shows a partial wave train in the eastern Pacific and a weak signal crossing North America. The southward reflecting part of the wave train is similarly weak. The same is not the case in the SEAS5 wave train (Figure 5.1 i). The wave train in the ensemble mean of SEAS5 starts off stronger and aligns spatially well with ERA5, but in the eastern Pacific it completely reflects southward. In contrast to the OIFS and ERA5, the SEAS5 wave train does not split, is much weaker over the east Pacific, and does not cross North America. This raises the question how SEAS5 predicted the NAO correctly while not predicting the quasi-stationary Rossby wave train correctly. The different teleconnection mechanisms in ERA5 and the models are further discussed in this work in chapter [Rossby wave train teleconnection 7] (for the wave train) and chapter [Stratosphere in reanalysis and model 6] (for the stratosphere). Additionally, an alternative teleconnection pathway via shifts in the mid-latitude jet and eddy, mean-flow interactions is discussed in chapter [Eddy, mean-flow interactions 8].

The origin point of the quasi-stationary wave train is the Indian Ocean region, which shows a strong precipitation dipole between east and west (as discussed in chapter 2.3.1). In ERA5 (Figure 5.1 j) the dipole is characterised by enhanced convection and rainfall in the western Indian Ocean and some over the central Pacific. Over the Maritime Continent convection and rainfall are reduced. Both the OpenIFS (Figure

5.1 k) and the SEAS5 (Figure 5.1 l) forecasts manage to capture the general precipitation patterns of 2019/2020. With increased precipitation in the western- and reduced precipitation in the eastern Indian Ocean both models show a positive IOD. The SEAS5 precipitation in both the Indian Ocean and the Pacific has slightly lower anomalies compared to ERA5, but the patterns are still mostly correct. Compared to ERA5, the OpenIFS and SEAS5 IOD shows a slightly more meridional structure versus the more zonal pattern in ERA5. Overall, both models manage to capture the precipitation anomalies of 2019/2020 adequately.
From the comparison above, I conclude that the OpenIFS does a good job in reproducing the main features of 2019/2020 and that I can use the OpenIFS to conduct experiments changing the forcing of this winter.

5.2 OpenIFS experiments

In their paper, Hardiman et al. (2020 [27]) concluded from a reversed IOD experiment that the IOD has a strong influence on the quasi-stationary Rossby wave train and the AO/NAO. To investigate the active teleconnections in DJF 2019/2020 in more detail I am using model experiments with perturbed SST and Sea Ice (CI) conditions. Since the OpenIFS shows a good ability to forecast the conditions in 2019/2020, I am confident that these perturbation experiments do show realistic aspects of the climate system. The perturbation experiments are conducted as described in the Methods chapter 3.2. Since the focus of these experiments is mainly on the Northern Hemisphere, the following plots are mostly centred on the North Pole.
In the first perturbation experiment (Indian Ocean only (IO only), left column in Figure 5.2), the lower boundary conditions (SST and CI) are set to climatological (1981-2020) average everywhere except for the Indian Ocean region (Figure 5.2 a). In the Indian Ocean, the SST and Sea Ice (CI not present in the IO) are left as the ERA5 conditions of 2019/2020. All other initial conditions (IC) and external forcing is left the same as the control experiment. The assumption here is that almost all seasonal anomalies in this experiment are caused by the 2019/2020 boundary condition anomalies in the Indian Ocean. A more detailed discussion of using climatological average SSTs is in chapter ([Differences in hindcasts 10). The results of this IO only experiment are compared to the control forecast and to ERA5. It has to be noted that all fields here are DJF averages, so while the SST does not show a clear dipole

structure in DJF, the November and December still showed a stronger east-west gradient (as seen in the SON mean in ERA5 2.2).
The total precipitation in this experiment (Figure 5.2 d) shows strong anomalies in the Indian Ocean sector, that agree well with the ones observed in the winter 2019/2020 in the Indian Ocean (compare to Figure 2.3). Outside the Indian Ocean, the precipitation anomalies from this experiment are small, with a slight northward shift of precipitation in the Pacific. In the Indian Ocean there is a clear east-west dipole visible in the precipitation anomalies, with less precipitation in the east and more in the west. This strong precipitation dipole is close to a canonical positive IOD event and acts as the origin for the teleconnection from the Indian Ocean. These teleconnections are evident in the Northern Hemisphere extratropics and are discussed next.
The main signal of the Z500 field in the IO only experiment in the Northern Hemisphere (Figure 5.2 g) is the positive AO/NAO. This positive AO is in very good agreement with the ERA5 in DJF 2019/2020 (Figure 5.1 a; Figure 4.4 a). The AO has a strong negative centre over Greenland and over Alaska, while positive anomalies are over the Aleutian region, off the east coast of America and over western Europe. The strength of the positive AO in the IO only experiment is greater than in the control experiment (see previous chapter 5.1) and the negative anomaly over Alaska is spatially closer to the ERA5 conditions. The negative anomaly over the Tibetan Plateau is also stronger in this experiment. This low over the Tibetan Plateau is connected to the subtropical westerly jet and precipitation anomalies over India (Yadav et al., 2013 [93]). The fact that the SST anomalies in the Indian Ocean region are enough to reproduce most features of the Z500 field from the 2019/2020 winter shows that the IOD had a strong influence on this winter. Additionally, since the control forecast shows weaker anomalies it is likely that teleconnections from other ocean basins weakened the impact of the IOD in the control forecast (this is also true when a 25 member subset of the control experiment is used).
The Rossby wave train that is discussed in Hardiman et al. (2020 [27]) and is evident in ERA5, is also evident in the IO only V200 (Figure 5.2 j). However, the phase and frequency of the wave train is different between the model experiment and ERA5. Where in ERA5, the signal was wave' 4 like, the signal in the IO only experiment is wave' 3 like. The main difference is over the North Pacific, which is evident in both Z500 and V200. The Z500 signal in ERA5 shows 2 centres of action (one in the west and one in the east), while the experiment only shows one high (centred over the central North Pacific). This difference is also evident in the wave train. The wave train in the IO only experiment has stronger anomalies in the eastern and

western North Pacific and none in the central North Pacific. Still, this difference has little impact on the conditions in the North Atlantic region for Z500 and V200. This indicates that either the wave train is not important as a teleconnection to the North Atlantic, or that reduced frequency in the model experiment averages out and the IOD teleconnection also works with a different frequency wave train. The wave train is discussed in more detail in chapter [Rossby wave train teleconnection 7].

In conclusion, the IO only experiment manages to reproduce a lot of important Northern Hemisphere features from just the forcing of the Indian Ocean. This is a strong indicator that the Indian Ocean Dipole played a large role in the winter conditions of 2019/2020.

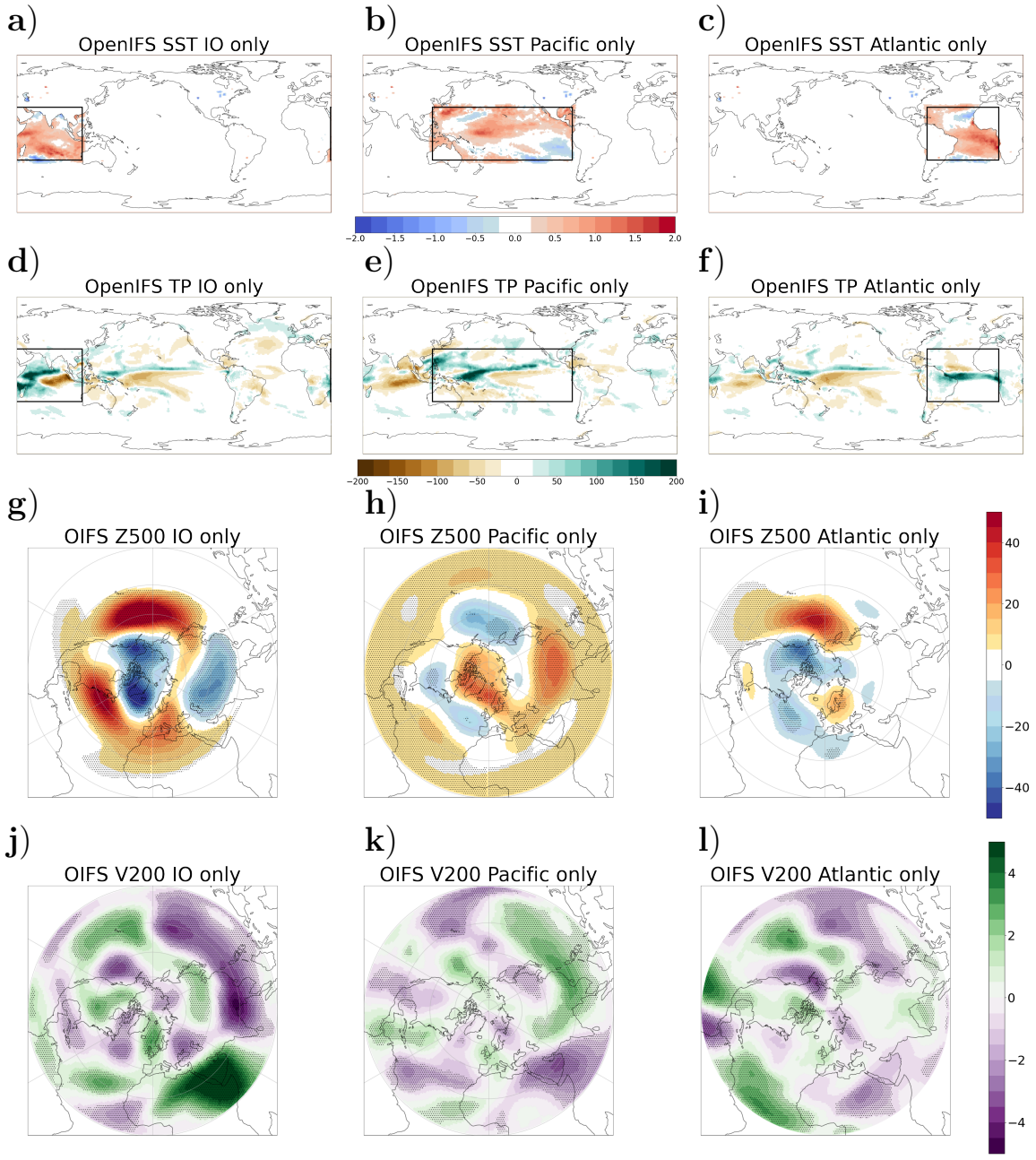


Figure 5.2: **OpenIFS tropical ocean experiments** for the DJF winter 2019/2020. **Left** Indian Ocean only, **Middle** Pacific Ocean only, and **Right** Atlantic Ocean only. **Top** row SST [K], **Second** row TP [mm/month], **Third** row Z500 [m], and **Bottom** row V200 [m/s]. Anomalies are calculated against the 1981-2020 climatological average. Stippling denotes significance and is calculated with a 2-sided bootstrapping at 5%.

To investigate the impact of other ocean basins on the winter 2019/2020 conditions and to test whether the IC of the November could have played a role, more experiments are conducted with perturbations in other ocean basins.
In the second perturbation experiment (Pacific Ocean only, middle column in Figure 5.2), the SST (top row) in the tropical Pacific Ocean is left as the 2019/2020 BC, while everywhere else the SST is set to climatological average. The large area of increased SST (due to climate change) has a significant impact the Z500 field.
The precipitation in the Pacific only experiment is mostly concentrated in the Pacific region, with some impact on the eastern Indian Ocean, that shows a dry anomaly (second row Figure 5.2 e). Similar to the SST in the Pacific only experiment, the precipitation is stronger and slightly shifted towards the central Pacific. This resembles a weak central Pacific El Niño. The tropical Atlantic only shows very small precipitation anomalies as a response to the anomalous SSTs in the Pacific in this experiment.
Both the Z500 (third row Figure 5.2 h) and the V200 (bottom row Figure 5.2 k) fields show a signal that is almost opposite to the previous Indian Ocean only experiment. In the Z500 a negative AO/NAO is evident with negative Z500 anomalies over the mid-latitude Atlantic and the Aleutian region, while a high is centred over the Arctic and the Tibetan Plateau. This is reflected in the V200 anomaly (bottom row Figure 5.2 h) that shows a wave train in this Pacific only experiment that is again almost opposite to the Indian Ocean only experiment, as it has over many regions the opposite phase. Similar to the Z500 anomalies, the V200 wave train shows lower magnitudes in the Pacific only experiment, compared to the IO only experiment. This is likely since the anomalies in the Pacific were low compared to the ones in the Indian Ocean in the winter 2019/2020. However, the structure of the Pacific only experiment is close to what is expected from a year with a weak El Niño signal, which is basically what this experiment is. With the effect of climate change over the climatological average, the small positive signal in the tropical Pacific becomes a moderate El Niño event. This effect of an artificial El Niño is removed in the experiments in chapter [Impact of climate change on the IOD event of 2019/2020 5.4].
The fact that the results from the Pacific only experiment show the opposite to the ERA5 and the control forecast show that it was very likely not the SSTs in the Pacific or the IC that led to the strong positive AO/NAO.

The impacts of the tropical Atlantic Ocean only experiment (right column Figure 5.2) are smaller than both other tropical ocean experiments. The precipitation anomalies

are the lowest from these three experiments and only at the western coast of North America shows significant Z500 and V200 anomalies. This is an area where many of the C3S forecasts struggled to reproduce the negative Z500 anomaly over Alaska. So even though the Atlantic didn't have large impacts on the Northern Hemisphere, the impact on the region around Alaska might be important to get the correct forecast in this area. However, since the Indian Ocean only experiment also manages to reproduce this area well it is not clear how large the influence of the Atlantic in this winter was in reality. Since there is no large signal in the NAO region, these experiments indicate that the tropical Atlantic did not play a large role in the NAO conditions in the 2019/2020 winter.

To leverage the ensemble nature of the experiments I investigated the NAO index in each ensemble member in the experiments compared to the control experiment (Figure 5.3). The NAO index is calculated in the same way as in Figure 4.2 as the Z500 difference between two boxes in the North Atlantic (north $60-80°$N and $10-40°$W; south $30-50°$N and $10-40°$W). The comparison between the ensemble members in the control experiment and the Indian Ocean only experiment (Figure 5.3 a) shows a shift in both the ensemble mean and the individual members of the Indian Ocean only experiment towards a more positive NAO. This is in agreement with the ensemble mean Z500 field of the IO only experiment (Figure 5.2 g) that showed an even more positive NAO than the control experiment (Figure 4.1 d). This even stronger positive NAO is likely the result of the removal of other conflicting ocean basins in the IO only experiment. Although the ensemble mean and most ensemble members in the IO only experiment show a positive NAO, some members still have a neutral or negative NAO.
Compared to this, the ensemble in the Pacific only experiment is shifted towards a more negative NAO (Figure 5.3 b), again in both the ensemble mean and the individual ensemble members. In this experiment only few members show a positive NAO, in agreement with the ensemble mean field (Figure 5.2 h). In the Atlantic only experiment (Figure 5.3 c), the ensemble is more neutral with only a small shift towards a negative NAO. In Figure 5.2 most of the variables (including Z500) did not show large anomalies in the ensemble mean, which is here reflected in the individual ensemble members.
The NAO in the experiments is shifted towards a more positive (IO only) or negative (Pacific and Atlantic only) phase, but the overall shape of the ensemble is still well

defined and appears as expected. The differences between the tropical ocean experiments and the control experiment are largest in the IO and Pacific only experiment and show roughly the same magnitude (compared to the control experiment).

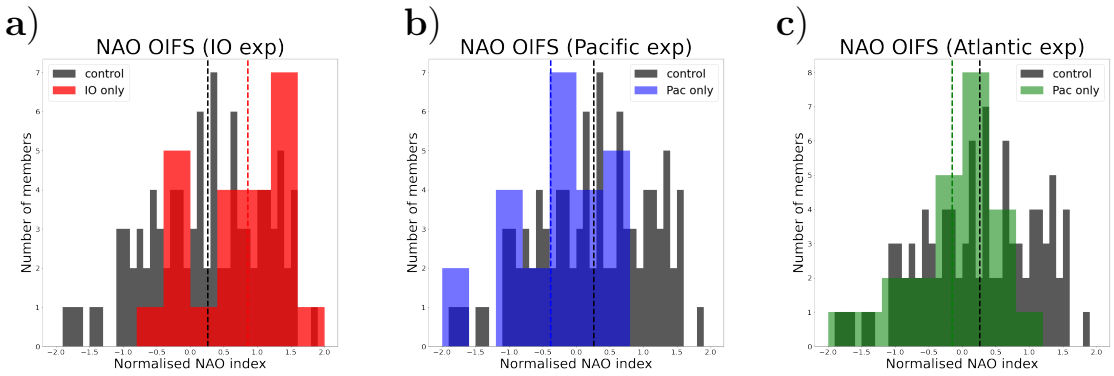


Figure 5.3: **OpenIFS NAO in experiments** for the DJF winter 2019/2020. **Left** Indian Ocean only, **Middle** Pacific Ocean only, and **Right** Atlantic Ocean only. The normalised NAO index is calculated from the Z500 difference between a northern and southern region of the North Atlantic. The northern region is defined as $60 - 80°$N and $10 - 40°$W and the southern box as $30 - 50°$N and $10 - 40°$W. Dashed lines indicate the ensemble mean and the cyan line indicates the ERA5 NAO. Anomalies are calculated against the 1981-2020 climatological average.

Studies have suggested an impact from the NH extratropics onto the NAO (Czaja and Frankignoul, 2002 [11], and Han et al., 2016 [25]). To test the impact of the Northern Hemisphere extratropics and Southern Hemisphere extratropics, I conducted two additional model experiments for the boreal winter 2019/2020. In these two experiments I set the SSTs north of 30°N to the 2019/2020 conditions (Figure 5.4 a) and the SSTs south of 30°S to the 2019/2020 conditions (Figure 5.4 b). As in the previous experiments, the SSTs outside these regions are set to the climatological average. These two model experiments show some Z500 anomalies in the Northern Hemisphere (Figure 5.4 d - e), but these anomalies are generally smaller and show less coherent structure compared to the tropical ocean experiments (Figure 5.2). Similarly, the V200 anomalies from both experiments (Figure 5.4 g - h) both do not show clear Rossby wave trains.

As an alternative to the IO only experiment, I conduced an experiment where I reversed the SST anomalies in the Indian Ocean region (i.e. I subtracted the SST anomaly of 2019/2020 in the Indian Ocean region twice from the real 2019/2020 SST conditions (Figure 5.4 c)). This reversed SST experiment shows a negative AO/NAO signal in the Northern Hemisphere (Figure 5.4 f). This result is in agreement with

the previous results form the IO only experiment (Figure 5.2), showing the opposite NH response to the opposite Indian Ocean SSTs. It is also in agreement with the experiment from Hardiman et al. (2020 [27]). However, a difference is evident in the Rossby wave train (V200 Figure 5.4 i). While over the Indian Ocean, a dipole of the V200 is evident, this wavetrain is not evident propagating across the North Pacific. A more in depth analysis of the Rossby wave train is in chapter [Rossby wave train teleconnection 7].

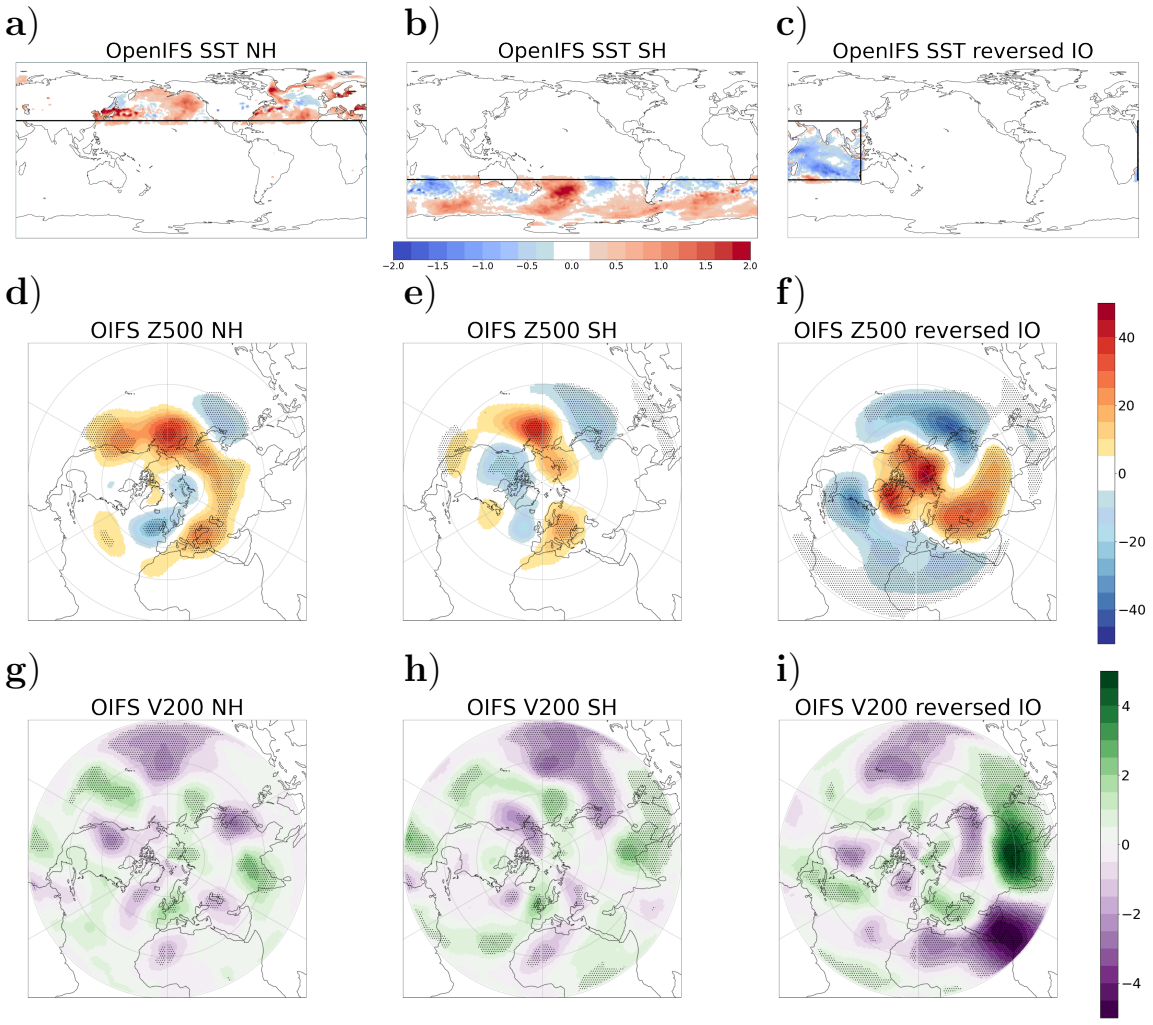


Figure 5.4: **Extratropics OpenIFS experiments** for the DJF winter 2019/2020. **Left** Northern Hemisphere, **Middle** Southern Hemisphere, and **Right** reversed IOD. **Top** row SST [K], **Second** row Z500 [m], **Third** row V200 [m/s]. Anomalies are calculated against the 1981-2020 climatological average. Stippling denotes significance and is calculated with a 2-sided bootstrapping at 5%.

5.3 Combination of tropical drivers

The Indian Ocean only, Pacific Ocean only, and Atlantic Ocean only experiments discussed above show that the Indian Ocean has the strongest influence on the Northern Hemisphere in 2019/2020. The results of the IO only experiment are also closest to the observed conditions in ERA5. However, these experiments do not answer the question how impacts of the individual ocean basins interact with each other and combine. To answer this question, this chapter investigates model experiments with multiple ocean regions set to 2019/2020 and compares the results to linear combinations of results from individual ocean basin experiments.

As a small aside, I first investigate the impact of the size of the SST perturbation in the Pacific experiment (i.e. does the large size of the Pacific experiment SST perturbation have an impact on the results). For this purpose I compare the Pacific only experiment (left column Figure 5.5) to a second experiment where I only set the SST conditions in the Niño 4 box to 2019/2020 conditions (right column Figure 5.5), as this box is centred around the very weak El Niño of this winter. Comparing the precipitation and Z500 anomalies from this small Pacific experiment to the larger Pacific only experiment (compare Figure 5.5 left and right), it is evident that the anomalies are stronger in the experiment that uses the smaller region of 2019/2020 SST. Even though the region is more confined, the precipitation anomalies over this region and even outside are stronger. This might seem counter intuitive as one could expect a smaller perturbation to have a smaller response. However, the zonal SST gradient is larger in the small Pacific experiment. While in the larger Pacific only experiment, positive SST anomalies stretch over most of the tropical Pacific, the SST anomalies in the small Pacific experiment are (by design) concentrated in the Niño 4 region. This leads to a clearer shift of the Walker circulation and a more concentrated precipitation signal. Similarly, the Northern Hemisphere Z500 anomalies are stronger in the small Pacific experiment. Especially the Aleutian region shows a much more negative anomaly related to the stronger precipitation anomaly in the tropical Pacific. The Arctic and the North Atlantic region also show stronger anomalies, leading to a more positive AO/NAO. This shows that the size of the anomalous SST region is not linearly linked to the strength of the teleconnection.

Further non-linear behaviour between the SST boundary forcing and the atmospheric response is observable in the combined ocean basin experiments (Figure 5.6). Here, I

have run an experiment with the both the Indian Ocean and the small Pacific Ocean set to 2019/2020 and everywhere else to climatological average. I compare the results from this experiment to the linear combination of the model output from the IO only and small Pacific only experiment. I have repeated the method for the larger Pacific area experiment, but no large differences to the results shown here are observable. I therefore only show the results using the smaller Pacific only experiment.

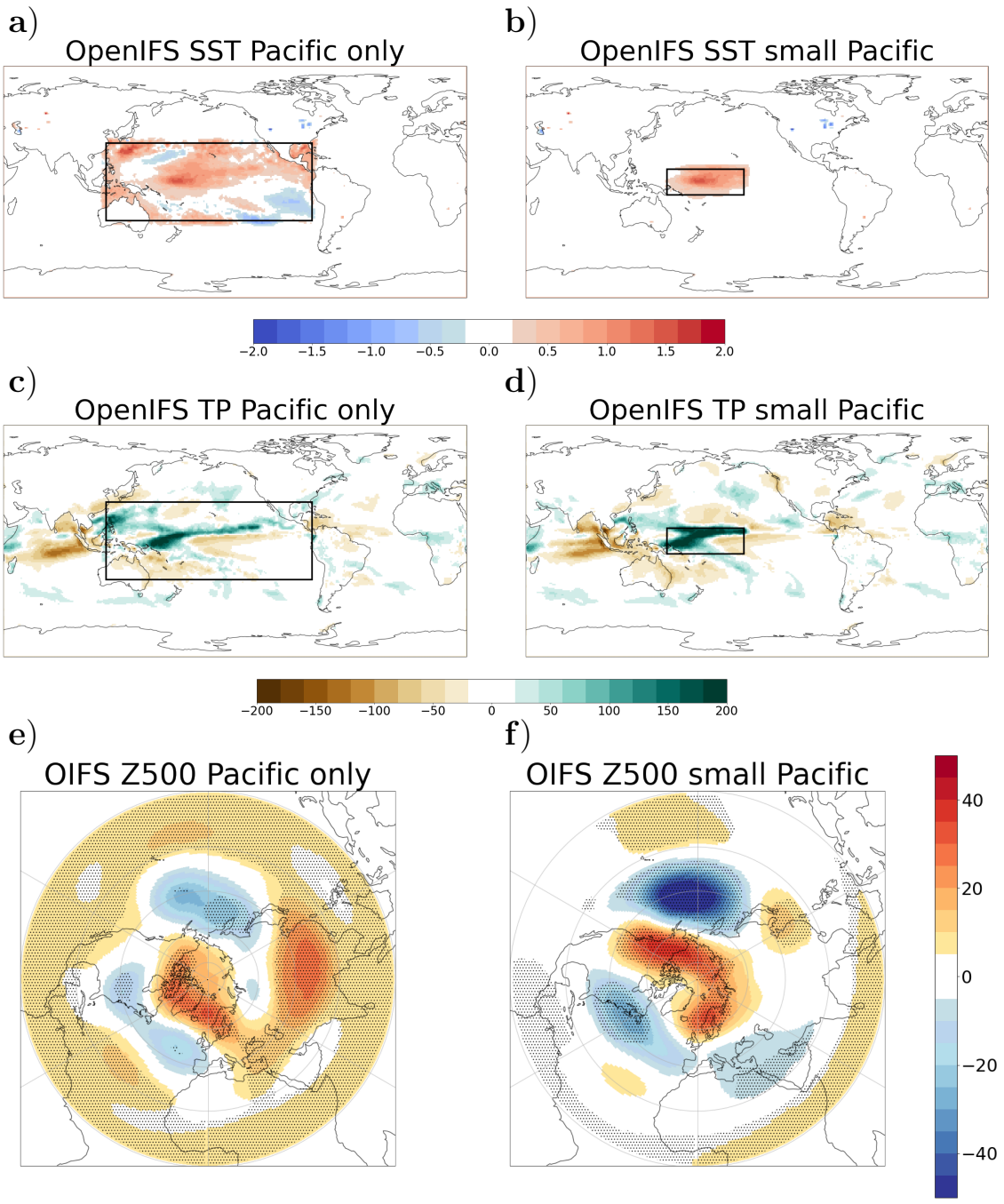


Figure 5.5: **OpenIFS small and large Pacific experiment** for the DJF winter 2019/2020. **Left** Pacific Ocean only and **Right** small Pacific Ocean only. **Top** row SST [K], **Second** row TP [mm/month], and **Bottom** row Z500 [m]. Anomalies are calculated against the 1981-2020 climatological average. Stippling denotes significance and is calculated with a 2-sided bootstrapping at 5%.

Here, I show the experiment with with the Indian Ocean and the smaller Pacific Ocean SST from 2019/2020 and everywhere else set to climatological average (left column Figure 5.6). The precipitation anomaly from the combined IO and small Pacific experiment (Figure 5.6 b) shows both positive precipitation anomalies in the western Indian Ocean, as well as in the central Pacific. The two positive anomalies are separated by an area of subsidence over the maritime continent, that is slightly stronger than it was in the individual IO and small Pacific experiments. As a contrast to this experiment I linearly combine the results from the IO only and small Pacific only experiment (middle column Figure 5.6). If the signal from Indian Ocean and Pacific are independent of each other, it would be expected that the linear combination of the model output is the same as the combined experiment. This is not the case however. The linear combination of IO only and small Pacific Ocean shows a similar pattern of tropical precipitation anomalies, but the magnitude of the anomalies is lower. Some of this lower magnitude can be explained since anomalous SSTs in the two individual experiments have precipitation anomalies centred in the two individual basins (Indian Ocean and Pacific (Figure 5.2 and Figure 5.5). The non-local teleconnection patterns show much larger differences between the linear combination and the combined experiment, where not only the magnitude, but also the anomaly patterns differ.

The Z500 anomalies from the combined IO + small Pacific experiment (left column Figure 5.6) still show a positive AO/NAO, but with some differences compared to the IO only experiment (Figure 5.2 d). The largest difference between the combined IO + small Pacific experiment and the IO only experiment is the split of the Aleutian anomaly. Where the IO only experiment has a strong consistent positive Z500 anomaly over the entire North Pacific, the combined IO + small Pacific experiment shows a split of the positive anomaly into a western and eastern part. This split of the positive anomaly is closer to the real conditions observed in ERA5 (Figure 5.1 a), which also show a split of the high (although the split high is located further south). Overall the combined IO + small Pacific experiment results are closer to the IO only experiment than to the small Pacific experiment (compare left column Figure 5.6 to left column Figure 5.2 and right column Figure 5.5). This is especially the case for the North Atlantic region and the low over central Asia, which strongly resemble the IO only experiment. The size of the two anomalous regions is unlikely to have played a large role, since I recreated the experiment with the larger Pacific region + IO and the results were even more in favour of an Indian Ocean impact.

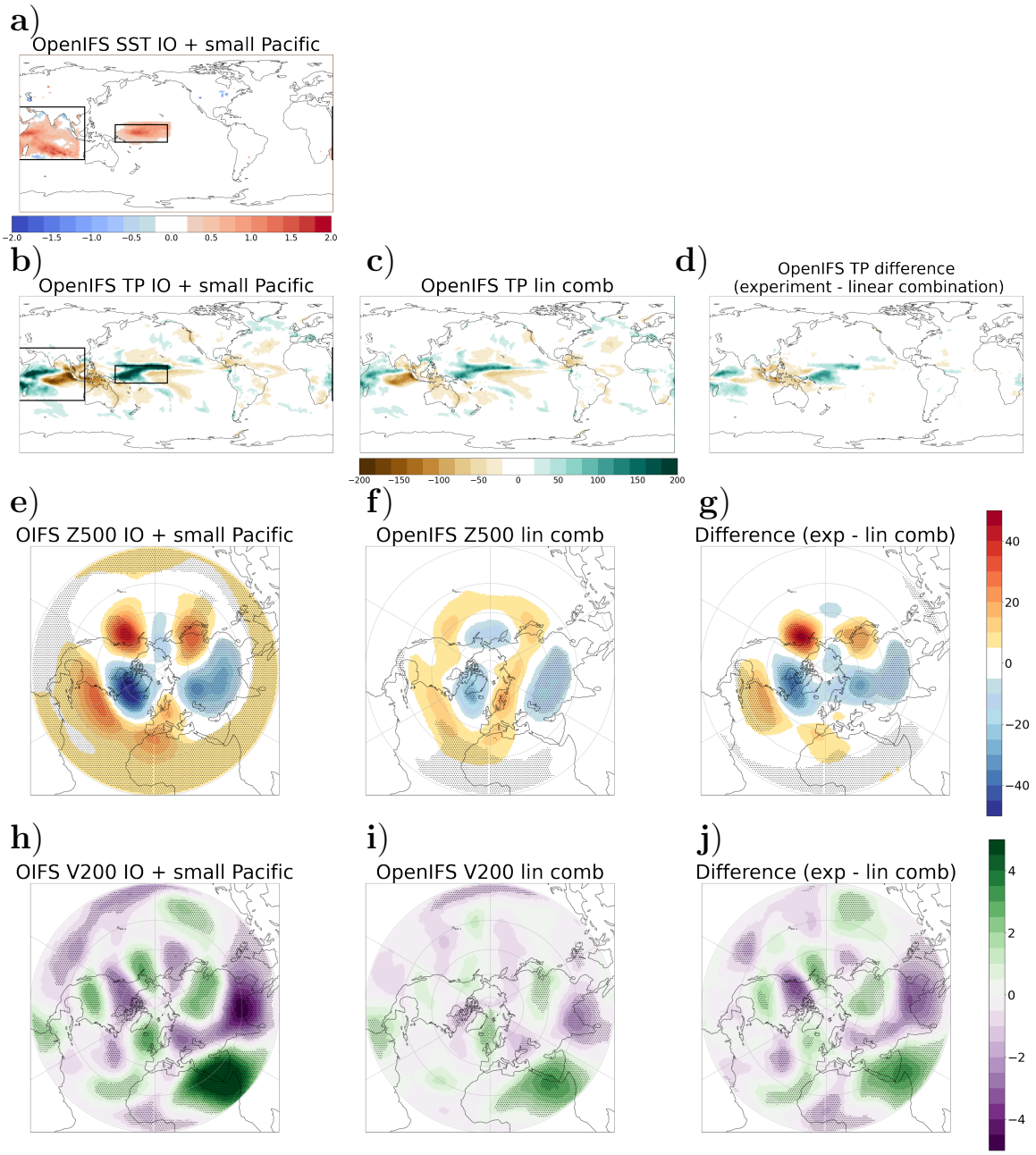


Figure 5.6: **Linear combination of OpenIFS experiments** for the DJF winter 2019/2020. **Left** OpenIFS model experiments IO + small Pacific, **Middle** Linear combination of the IO only experiment and small Pacific only experiment results, and **Right** Difference between the IO + small Pacific experiment and the linear combination of results (left - middle). **Top** row SST [K], **Second** row TP [mm/month], **Third** row Z500 [m], and **Bottom** row V200 [m/s]. Anomalies are calculated against the 1981-2020 climatological average. Stippling denotes significance and is calculated with a 2-sided bootstrapping at 5%.

The linear combination of IO only and small Pacific only (middle column Figure 5.6) shows a very small positive AO/NAO. However, since the anomalies from the small Pacific only experiment are nearly as large (and opposite) as the ones from the IO only experiment, the linear combination shows very weak signals. The linear combination of these two experiments does not show large areas of significant Z500 anomalies and in fact, the difference between the combined IO + small Pacific and the linear combination (right column Figure 5.6) is in most areas larger than the linear combination. The meridional wind anomalies at 200 hPa (bottom row Figure 5.6) show similar results to the Z500 results. The wave train in the combined IO + small Pacific experiment is again closer to the 2019/2020 one observed in ERA5 (Figure 5.1 g) than the one in the IO only experiment. The combined experiment shows a wave 4 like structure similar to ERA5, where the IO only showed a wave 3 like structure (compare Figure 5.1 and Figure 5.6). This is linked the split of the Z500 anomaly in the North Pacific, that is a single large anomaly in the IO only experiment. However, the wave train in the combined experiment reflects more towards the south at the west coast of North America than the one in ERA5. This problem of the model wave train reflecting southward in model runs is further discussed in chapter [Rossby wave train teleconnection 7]. The linear combination of the wave train of IO only and small Pacific (bottom middle Figure 5.6) shows only very weak anomalies in the extratropics. This is not surprising since the Indian Ocean and Pacific wave trains are expected to have different/opposite phase. Therefore, most of the signal is here in the difference (nonlinear part(Figure 5.6 j)) where the Indian Ocean teleconnection dominates.
The fact that the linear combination of the two experiments shows significant differences compared to the combined experiment, shows that the two teleconnections from the Indian Ocean and the Pacific do not interact purely linearly with each other. In the case of the combined experiment, the impact from the Indian Ocean is stronger than the one from the Pacific and the NH extratropical signal is closer to the IO only experiment, than to the Pacific only (or small Pacific). This gives a possible explanation for the lack of historical observations of the teleconnection from the Indian Ocean. When in most years with both ENSO and IOD active the ENSO signal is stronger, the extratropical signal is dominated by the ENSO teleconnection rather than the one from the IOD. In some years, like 2019/2020, when the IOD is strong and the ENSO signal is small, this interaction reverses and the signal from the Indian Ocean dominates over that from the Pacific and a positive IOD can lead to a positive AO/NAO.

All tropical ocean basins combined still show the signal from the IOD, but the anomalies are weaker than in the IO only experiment and closer to the control forecast (not shown).

5.4 Impact of climate change on the IOD event of 2019/2020

The previous chapters show a strong consistent impact of the IOD onto the Northern Hemisphere winter in 2019/2020. However, studies have shown that the strength of teleconnections can vary on decadal (O'Reilly, 2018 [57]) and centennial (Merkel, et al. 2010 [52]) timescales due to the background climate. Even for more well known teleconnections such as the ENSO teleconnections it is uncertain how they will change under climate change (Alizadeh, 2023 [2]). In the following I am conducting model experiments to simulate colder different background climates for the IOD 2019/2020. In the OpenIFS IO only model experiment (Figure 5.2), the strong impact of the IOD on the AO/NAO does not only depend on the strength of the dipole or the absence of an ENSO event, but also on the background climate change. This chapter analyses the previously discussed teleconnections in different climatic backgrounds. A special focus is placed on the IOD in colder climate, where the teleconnections are less strong than in 2019/2020.

To test the impact of the IOD (and other tropical oceans) onto the atmospheric conditions in different climate states, the experiments discussed before are repeated with adjusted SSTs. For example, in the Indian Ocean only experiment a constant factor is subtracted from the Indian Ocean region (named: reduced IO only). While the strength and shape of the dipole itself are retained using this method, the overall temperature is brought towards the 1981-2020 average. To conduct this experiment I calculate the linear SST trend in the Indian Ocean region (black box in Figure 5.7). I then subtract half of the trend to adjust for the climate change impact, simulating as if the 2019/2020 IOD had happened in 2000 (half way between 1981 and 2020). This way, the SST's in the reduced IOD only experiment in the Indian Ocean match the climatological average (1981-2020) SST outside the Indian Ocean. For these experiments I only removed the linear trend of the climate change signal between 1981-2020, therefore the nonlinear increase of climate change, as well as the impact of the Indian Ocean Dipole still remain in the SST.
To investigate the difference between the experiments with climate change (e.g. IO only) and the ones without climate change (e.g. reduced IO only) I analyse the D200, Z500, and V200 fields of the corresponding experiments and their difference. The divergence at 200 hPa (D200) shows a dipole in the Indian Ocean in both the IO only experiment (second row Figure 5.7) and in the reduced IO only experiment.

Both experiments have a centre of increased divergence in the western Indian Ocean contrasted by an area of increased convergence over the maritime continent. The difference between the two model experiments is in the magnitude of the divergence. The IO only experiment (left column Figure 5.7) shows generally more divergence over the western Indian Ocean and less over the eastern Indian Ocean compared to the reduced IO only experiment (middle column Figure 5.7). The difference between the two experiments (right column Figure 5.7) resembles an IOD pattern, showing that the atmospheric circulation is influenced not just by the dipole, but also the absolute SST maximum. This change in the strength of the upper level divergence has an impact on the state of the Northern Hemisphere. Compared to the IO only (Figure 5.7 f), the reduced IO only (Figure 5.7 g) Z500 shows a less strong AO/NAO signal. However, most of the prominent features that are present in the IO only experiment, are also evident in the reduced IO only experiment. That includes the negative Z500 anomaly over the Arctic, the high over the Aleutian region and the two highs over eastern North America and western Europe. The difference between these two experiments (right column Figure 5.7) shows a positive AO/NAO signal that is spatially quite close to the anomaly patterns observed in both IO only and reduced IO only experiment. This shows that for the Indian Ocean teleconnections to the Northern Hemisphere, not just the strength of the dipole (west - east) is important, but also the maximum SST in the Indian Ocean region. Analysing the quasi-stationary Rossby wave train in the two experiments (bottom row Figure 5.7) it becomes evident that the wave train is not weaker in the reduced IO only experiment. From the analysis of the Z500 fields and the weaker AO/NAO one could assume that a weaker AO/NAO (thought to be influenced by the wave train) is connected to a weaker wave train as well. These experiments show the opposite however. The wave train in the reduced IO only experiment is slightly stronger over the North Pacific and North America. One noticeable difference between the two wave trains is, that the reduced IO only wave train misses the positive anomaly over Japan, where the wave train is shifted.

The comparison of the two model experiments, considering upper level divergence and Z500 paints a relatively clear picture for the involved dynamics. Reducing the average SST of the perturbed Indian Ocean area also reduces the upper level divergence dipole over the Indian Ocean. This change of the circulation weakens the impact on the AO/NAO leading to a less strong signal over the Northern Hemisphere. The fact that the wave train does not get weaker in the reduced Indian Ocean only experiment

indicates that the wave train is at the very least not the only teleconnection mechanism between the Indian Ocean region and the North Atlantic.

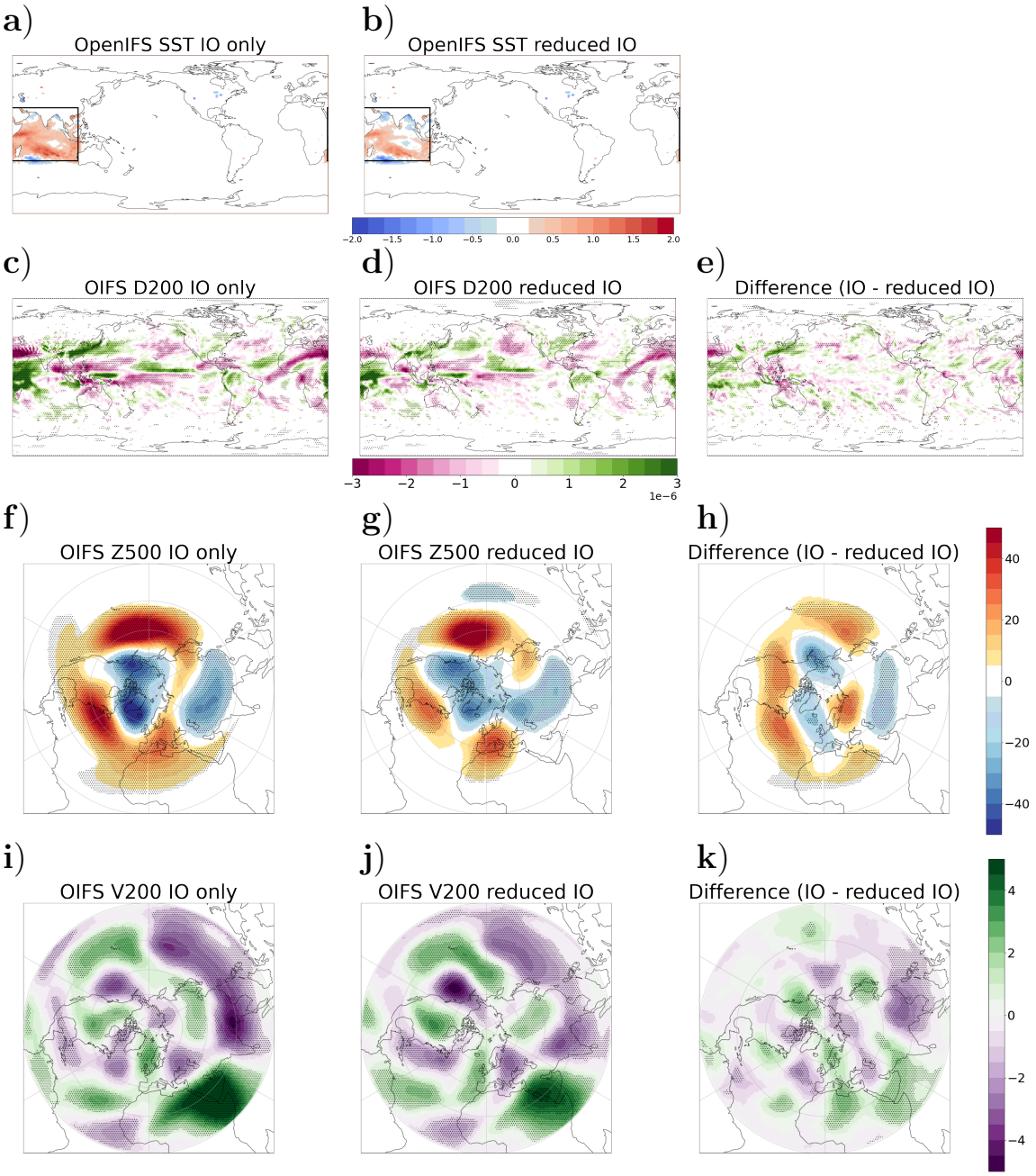


Figure 5.7: **Impact of climate change on the Indian Ocean experiment** for the DJF winter 2019/2020. **Left** Indian Ocean only, **Middle** reduced Indian Ocean only, and **Right** difference between the Indian Ocean only and the reduced Indian Ocean only experiment (left - middle). **Top** row SST [K], **Second** row D200 [1/s], **Third** row Z500 [m], and **Bottom** row V200 [m/s]. Anomalies are calculated against the 1981-2020 climatological average. Stippling denotes significance and is calculated with a 2-sided bootstrapping at 5%.

Conducting an equivalent experiment with a reduced Pacific only, shows equivalent results. In the same manner as the previous experiment, the SSTs in the reduced Pacific experiment are adjusted to counteract climate change (compare Pacific only SST and reduced Pacific SST top row Figure 5.8). The reduced Pacific only experiment shows generally lower extratropical Z500 anomalies than the normal Pacific only experiment.
Since the ENSO event of 2019/2020 was not strong, even the normal Pacific only experiment does not show very strong upper level divergence anomalies (D200 second row Figure 5.8). The upper level divergence that is observed in the reduced Pacific only experiment (Figure 5.8 d) is also small. The difference between these two experiments (Figure 5.8 e) shows some reduction of divergence over the Pacific ocean and some reduction of convergence over the Indian Ocean, but the differences are small compared to the ones observed in the Indian Ocean experiments. A similar response can be observed in the Z500 fields (third row Figure 5.8). As discussed before (chapter [OpenIFS experiments 5.2]) the Pacific only experiment shows a weak negative NAO. This weak signal is now weakened even further in the reduced Pacific only experiment (Figure 5.8 g). Over the North Atlantic region, the pattern of Z500 still resembles a negative NAO, but the anomalies are very low and not significant. The difference between the two experiments (Figure 5.8 h), shows a weak negative NAO like signal with a negative anomaly over the Aleutian region. The V200 wave train in the reduced Pacific experiment (Figure 5.8 j) is very weak and not significant in the North Pacific area or over North America. This is different from the Pacific only experiment (Figure 5.8 k) where a wave train from the tropical Pacific to the North Pacific and towards the North Atlantic is still observable.

The fact that in the Pacific case, there is a slight weakening of all divergence, wave train, and Z500 anomalies between the normal Pacific only and reduced Pacific only experiment is different from the Indian Ocean experiments. In the Indian Ocean experiments, both the divergence and the Z500 fields weakened, but the wave train stayed the same between the two experiments. This indicates that while the wave train is important for the Pacific as a teleconnection to the mid- and high-latitudes, it is less important for the Indian Ocean teleconnections. The reduced Pacific only experiment shows again, that absolute maximum SST values play a role in addition to the pattern of SST anomalies.

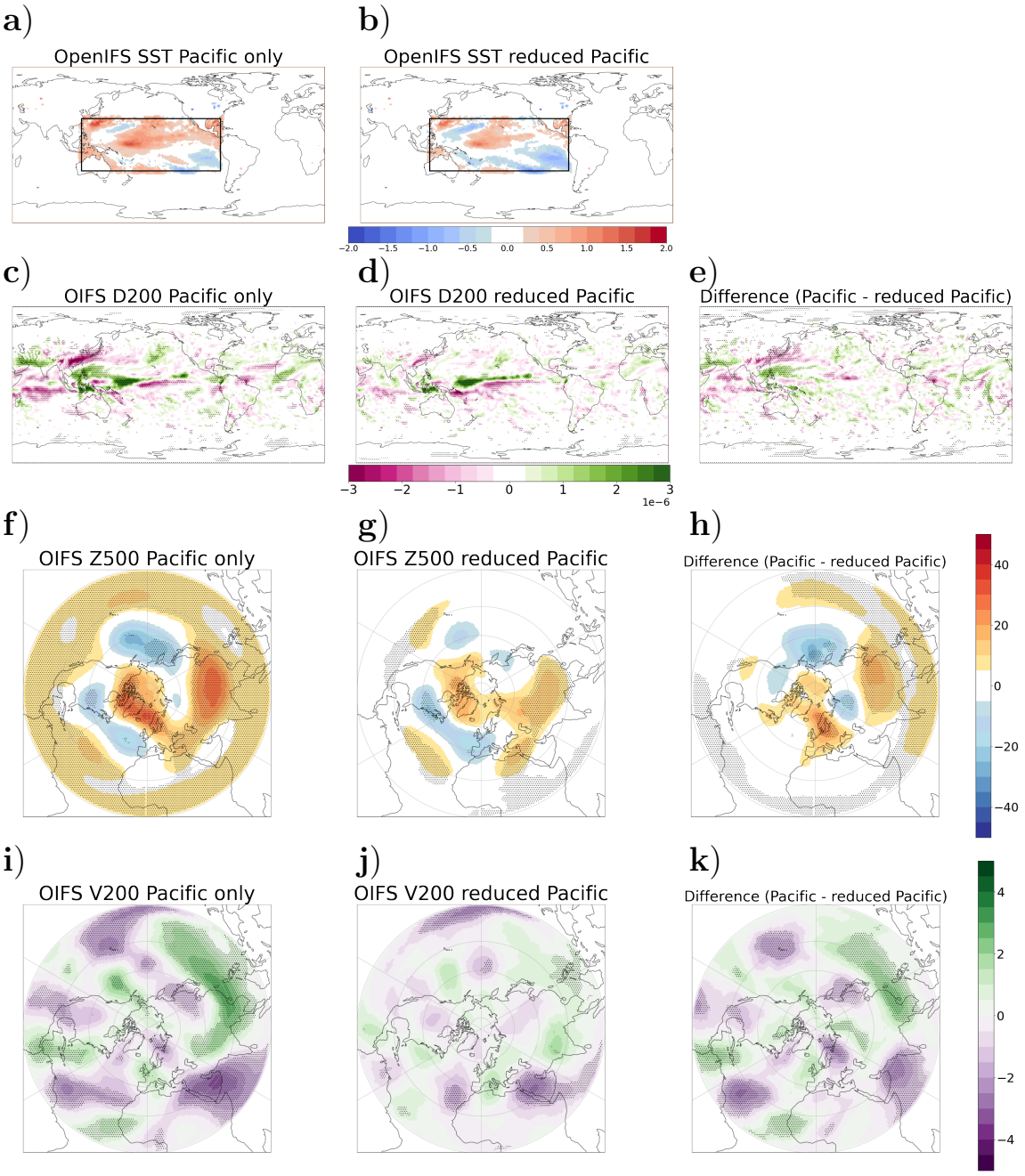


Figure 5.8: **Impact of climate change on the Pacific Ocean experiment** for the DJF winter 2019/2020. **Left** Pacific Ocean only, **Middle** reduced Pacific Ocean only, and **Right** difference between the Pacific Ocean only and the reduced Pacific Ocean only experiment (left - middle). **Top** row SST [k], **Second** row D200 [1/s], **Third** row Z500 [m], and **Bottom** row V200 [m/s]. Anomalies are calculated against the 1981-2020 climatological average. Stippling denotes significance and is calculated with a 2-sided bootstrapping at 5%.

In the Southern Hemisphere only small/insignificant differences between the model experiments are observable (not shown). An analysis of the Southern Hemisphere anomalies is in chapter [Initial condition impact on the Southern Hemisphere 9]. Experiments with only half of the climate change signal removed show a signal that is in between the experiment with climate change and the experiment without. Since these intermediate experiments do not show any new signals, they are not discussed in more detail and not shown in this thesis.

The experiments conducted with the OpenIFS show that:

- The OpenIFS control forecast is able to reproduce many of the 2019/2020 features and can be used to conduct perturbation experiments.
- An experiment with SSTs from 2019/2020 in the Indian Ocean and climatological SSTs everywhere else is able to reproduce most of the Northern Hemisphere features of DJF 2019/2020.
  - This includes a positive AO/NAO.
  - The wave train in this experiment is different to the one observed in ERA5, but the anomalies in the North Atlantic are still similar.
- A moderate El Niño experiment produces the opposite anomalies to the Indian Ocean only experiment. Since this experiment and the Indian Ocean experiment use the same initial conditions from 01.11.2019, it can be inferred that the IC did not drive the positive NAO.
- The anomalies from the tropical Atlantic are small and there is no significant NAO signal in the ensemble mean of this experiment.
- The combination of Indian Ocean and Pacific experiment shows that the Indian Ocean impact dominates in the winter 2019/2020.
- A reduction of the SST field to remove climate change reduces the impact of the IOD onto the Northern Hemisphere Z500 field, but the impact still exists.
- While the Z500 field gets weaker in the reduced IO only experiment, the wave train does not. This indicates that other teleconnection mechanisms exist.

As a whole, these experiments show the large importance of the IOD for the winter 2019/2020 and that winter IOD events can have impacts on the NAO.

Chapter 6

Stratosphere in reanalysis and forecast

In this chapter, I analyse the stratosphere as a teleconnection pathway between the IOD and the NAO in 2019/2020. In the 2019/2020 winter season, the Northern Hemisphere polar stratosphere was in a strong positive state. A stratospheric pathway has been proposed as a teleconnection mechanism between the IOD and the NAO (Hardiman et al., 2020 [27]). However, both the SEAS5 and the OpenIFS do not manage to reproduce major stratospheric features, but forecast the troposphere well. From this analysis, I find that it is unlikely that the stratosphere had a strong impact on the Northern Hemisphere winter 2019/2020.

This chapter aims to evaluate the impact of the polar stratosphere as a teleconnection between the IOD and the NAO in 2019/2020. Hardiman et al. (2020 [27]) identified the stratosphere as an important teleconnection pathway, similar to the ENSO teleconnection via the Stratosphere (Domeisen et al., 2018 [14]). Hardiman et al. (2020 [27]) argue that the reduced strength of the Aleutian cyclone leads to less disruption of the polar vortex and a stronger stratospheric polar vortex. This signal then travels into the troposphere in January impacting the NAO.
To investigate this pathway in more detail I first use ERA5, SEAS5, and the OpenIFS stratospheric fields and afterwards the other C3S model forecasts of U10.

6.1 Analysis of stratospheric forecasts

The ensemble mean stratospheric forecasts of the OpenIFS and SEAS5 are compared to ERA5 for the winter 2019/2020. For this purpose I use the 10 hPa zonal wind (U10) and 10 hPa geopotential height anomalies (Z10) as indicators of the strength

of the stratospheric polar vortex. Earlier chapters (chapter [ECMWF model forecasts 4.1]) noted the skill of these two systems is high in the troposphere and especially in forecasting the NAO in this winter.

The ERA5 U10 stratospheric anomalies of DJF 2019/2020 (Figure 6.1 a) are characterised by strong easterlies in the tropical latitudes and westerlies in the polar regions. This wind patterns relate to an easterly QBO phase and a strong stratospheric polar vortex. The U10 forecasts of both the SEAS5 (Figure 6.1 b) and the OpenIFS (Figure 6.1 c) show major deficiencies in the representation of the U10 anomalies in this winter. While SEAS5 manages to reproduce the phase of the tropical anomalies correctly (negative QBO, albeit with a much reduced amplitude), large differences are evident in the mid- and high-latitudes. SEAS5 shows an incorrect weak stratospheric polar vortex with anomalous westerlies in the polar latitudes. The mid-latitudes are also showing the opposite phase of the wind anomalies with easterlies, instead of westerlies in ERA5. By comparison, the OpenIFS U10 anomalies (Figure 6.1 c) are similar to ERA5 in the polar- and mid-latitudes with a strong stratospheric polar vortex, but the OpenIFS fails to reproduce the negative phase of the QBO.
These errors in the stratospheric forecast do not just exist in the ensemble mean. Investigating the individual ensemble members of SEAS5 and the OpenIFS control experiment shows the problems with their forecast of the stratospheric polar vortex (SPV) and QBO in more detail (Figure 6.2). The QBO index here is calculated from the 10 hPa zonal mean wind anomalies between 5° N and 5° S. The SPV is calculated from 10 hPa zonal mean wind anomalies between $30 - 90°$ N.
While in the tropics none of the ensemble members manage to accurately capture the strength of the negative QBO, SEAS5 is in an overall negative state with a negative ensemble mean. The OpenIFS on the other hand predicted an overall positive state of the QBO with only few members showing a slightly negative QBO. This is in agreement with the with the global pattern of the QBO discussed above. The individual members of the models for the SPV show a very different picture. The spread of the ensemble in both models is much larger with ensemble members of both models exceeding the strength of the ERA5 SPV. This also means that a lot of ensemble members are in the opposite phase to the SPV from observations. This is especially true for SEAS5, which shows even the ensemble mean with a negative SPV. The OpenIFS does get the general phase of the SPV correctly, but is still much too weak in the ensemble mean. This under-confidence of both models about the SPV is a sign of the signal-to-noise paradox in seasonal forecasts of the Northern Hemisphere

(Scaife and Smith 2018 [70].

The geopotential height at 10 hPa (Z10) in SEAS5, and OpenIFS show problems as well. Again, ERA5 (Figure 6.1 d) shows a positive AO that is slightly shifted towards Eurasia with a strong positive anomaly over North America. The OpenIFS (Figure 6.1 f) is able to mostly reproduce these features, with the largest difference being that the positive anomaly over North America extends far into the North Atlantic and towards Europe. The SEAS5 Z10 (Figure 6.1 e) on the other hand shows a positive anomaly over the pole that is in agreement with the SEAS5 U10 of this winter, but opposite to the ERA5 Z10. From the Z10 it is not clearly possible to distinguish easterly and westerly phases of the QBO.
It is notable that both SEAS5 and OpenIFS manage to get a very well forecasted troposphere, despite these large deficiencies in the stratosphere.

Since the OpenIFS is not able to reproduce the tropical stratosphere correctly, there would be little confidence in the results from any other experiments with this model.

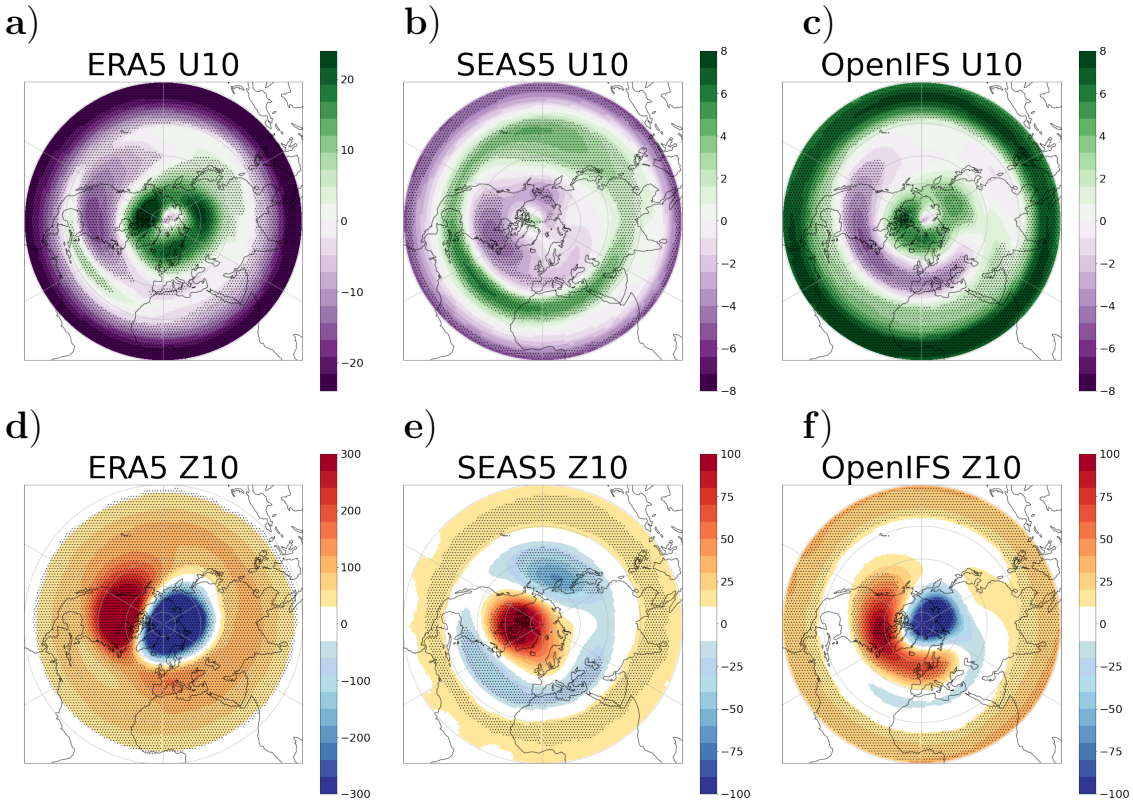


Figure 6.1: **Stratospheric conditions in ERA5, SEAS5, and OpenIFS** in the DJF winter 2019/2020. **Left** ERA5, **Middle** SEAS5, and **Right** OpenIFS control forecast. **Top** row U10 [m/s] and **Bottom** row Z10 [m]. Anomalies are calculated against the 1981-2020 climatological average. ERA5 stippling denotes significant areas calculated with a 2-sided Student's t-test at 5%. Model stippling denotes significance and is calculated with a 2-sided bootstrapping at 5%.

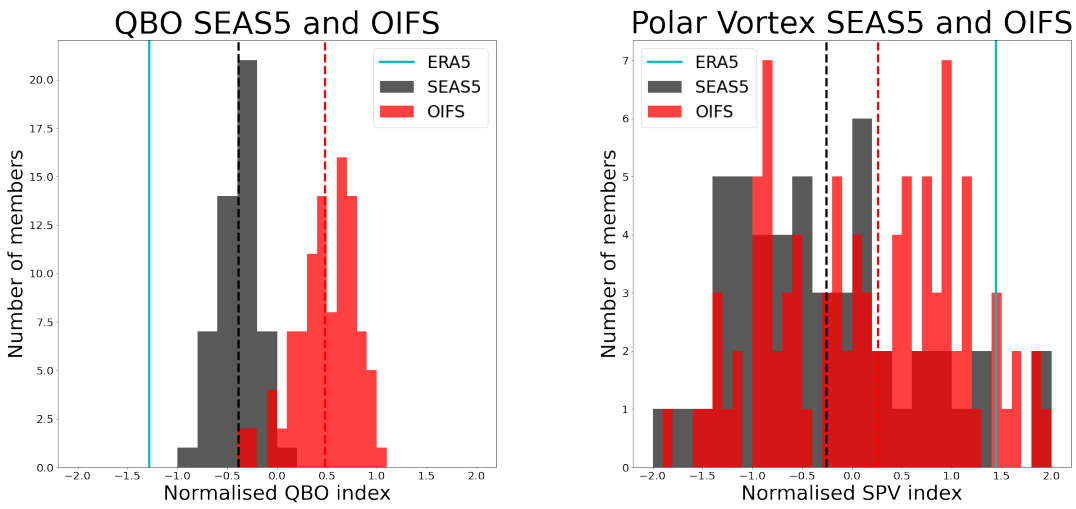


Figure 6.2: **Ensemble stratospheric conditions** from SEAS5 and the OpenIFS compared with ERA5 in the DJF winter 2019/2020. **Left** QBO conditions and **Right** Stratospheric Polar vortex conditions.

A larger range of forecasts is available from the Copernicus C3S models. Similar to Chapter 4.2 I analyse here the C3S multi-model mean, SEAS5, UKMO, DWD, CMCC, and Météo France forecasts and compare them to ERA5 in the DJF 2019/2020 (Figure 6.3). The model forecasts from the different centres shows a larger range of stratospheric forecasts and give an estimation whether a high stratospheric skill is necessary for the high observed tropospheric skill in the C3S.
As described before, the two main features of the stratosphere in ERA5 are the strong polar vortex and the easterly QBO (Figure 6.3 a). It is immediately obvious that many of the C3S models did not forecast both features well with the best ones being the UKMO and DWD (Figure 6.3 d and e). Both of these models capture the easterly phase of the QBO and have a slightly strengthened vortex (albeit not significant) in the ensemble mean. While the CMCC forecast (Figure 6.3 f) captures the easterly QBO, it also forecasts a partially significant weak phase of the polar vortex. As discussed before, the ECMWF SEAS5 (Figure 6.3 c) does not fully capture the easterly QBO and has the wrong polar vortex. The Météo France forecast (Figure 6.3 g) shows some mid-latitude features resembling the ERA5, but both the polar and tropical latitudes show only very weak amplitudes. Combined in the C3S multi-model mean (Figure 6.3 b), the forecast does show a correct easterly QBO and also some of the mid-latitude features, but the polar regions do not show a strong polar vortex like in ERA5.

Again, considering most of these models managed to forecast the positive AO/NAO correctly, the errors in the stratospheric forecasts make it unlikely that the teleconnection from the IOD to the NAO went via the stratosphere (especially in the models). The conclusion from this analysis are:

- SEAS5 and the OpenIFS are not suitable to investigate the stratospheric impact in the winter 2019/2020.
- Many C3S models have deficiencies in the forecast of the polar stratosphere in DJF 2019/2020.
- It is unlikely that the stratosphere had a large impact on the troposphere in the 2019/2020 winter, since many models manage to forecast the troposphere well despite having problems in the stratosphere.

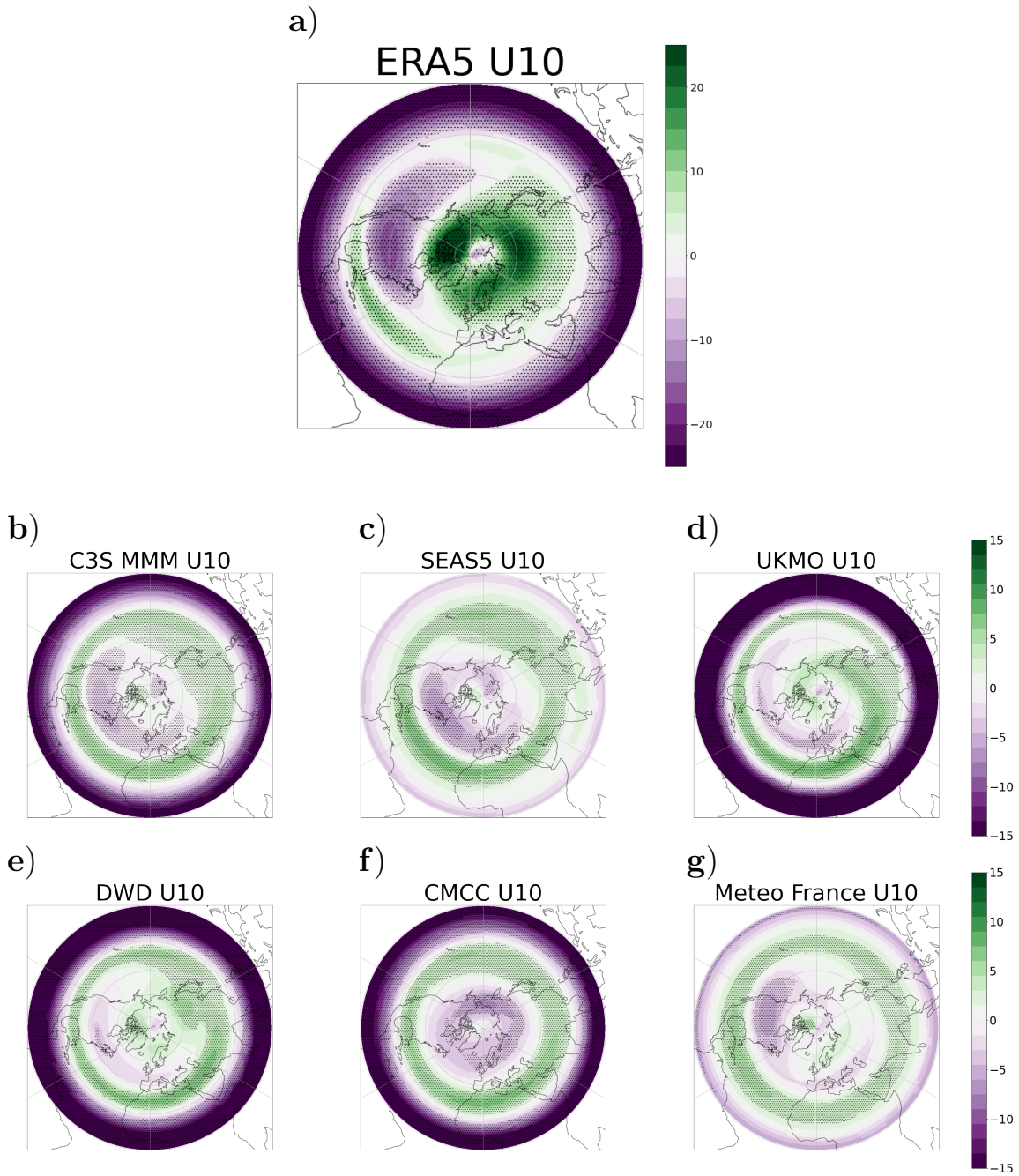


Figure 6.3: **U10 from C3S models in DJF 2019/2020** compared to ERA5. **a)** ERA5, **b)** C3S multi-model mean, **c)** SEAS5, **d)** UKMO, **e)** DWD, **f)** CMCC, **g)** Météo France [m/s]. Anomalies are calculated against the 1993-2016 climatological average. ERA5 stippling denotes significant areas calculated with a 2-sided Student's t-test at 5%. Model stippling denotes significance and is calculated with a 2-sided bootstrapping at 5%.

Chapter 7

Rossby wave train teleconnection

In this chapter, I analyse the Rossby wave train as a teleconnection pathway. I compare the wave train between models and ERA5, where it is evident that even though SEAS5 forecasts the NAO correctly, its wavetrain does not cross North America. This raises the question how the North Atlantic can be well forecasted when the teleconnection mechanism is not well reproduced. A helpful tool to investigate the connection between wavetrain and AO/NAO is the large ensemble from the OpenIFS@Home. I use this ensemble to create composites of ensemble members with a wave train that resembles ERA5. This composite helps me investigate the phase and strength of the AO/NAO in the individual members of the composite and shows how closely the wavetrain and the AO/NAO are connected. The result is that members with a ERA5-like wavetrain are slightly more likely to have a positive AO. For the NAO however, this result is even smaller and not significant. Therefore, it is unlikely that the Rossby wave train is the only teleconnection between the Indian Ocean and the North Atlantic active in DJF 2019/2020.

The quasi-stationary Rossby wave train teleconnection described by Hardiman et al. (2020 [27]) is evident in ERA5 in the meridional wind at 200hPa (Figure 7.1 a). In DJF this wave train emanates in the Indian Ocean and crosses the North Pacific and North America, reaching into the North Atlantic region where it helps establish the positive NAO. At the Pacific coast of North America, the wave train splits into a pathway that crosses North America and a second pathway that reflects back towards the equator. The equator ward pathway is weaker in ERA5 than the one over North America.
In the SEAS5 (Figure 7.1 b), the Rossby wave train emanates from the Indian Ocean and propagates into the North Pacific. From the North Pacific the SEAS5 wave train is reflected back to the equator and does not cross North America. The location of

the SEAS5 Rossby wave train fits well to ERA5 until the central north Pacific, with the last good agreement of a southward anomaly between Japan and Kamchatka. Downstream, SEAS5 shows a northward anomaly over and to the south of Alaska, the equivalent northward anomaly in ERA5 is located more in the central Pacific and further south. Instead over and south of Alaska, ERA5 shows a southward anomaly that continues into a North American northward anomaly. This area over North America shows a very clear difference in the paths of the wave trains in ERA5 and SEAS5. The ERA5 wave train leads into the North Atlantic region and projects onto the positive phase of the NAO. Meanwhile, the SEAS5 wave train continues the path from the North Pacific back southward and runs parallel to the North American coast.
The difference between the SEAS5 and ERA5 wave train over the North Pacific is also evident in the Z500 anomalies (Figure 5.1). The positive Z500 anomaly in ERA5 over the eastern North Pacific does not exist in SEAS5 and instead the negative Z500 anomaly over the Aleutians extends further southward.

The fact that the SEAS5 and ERA5 show different wave trains, but SEAS5 still manages to predict the NAO correctly indicates that the Rossby wave train teleconnection does not explain the full connection between IOD and NAO (at least in SEAS5).

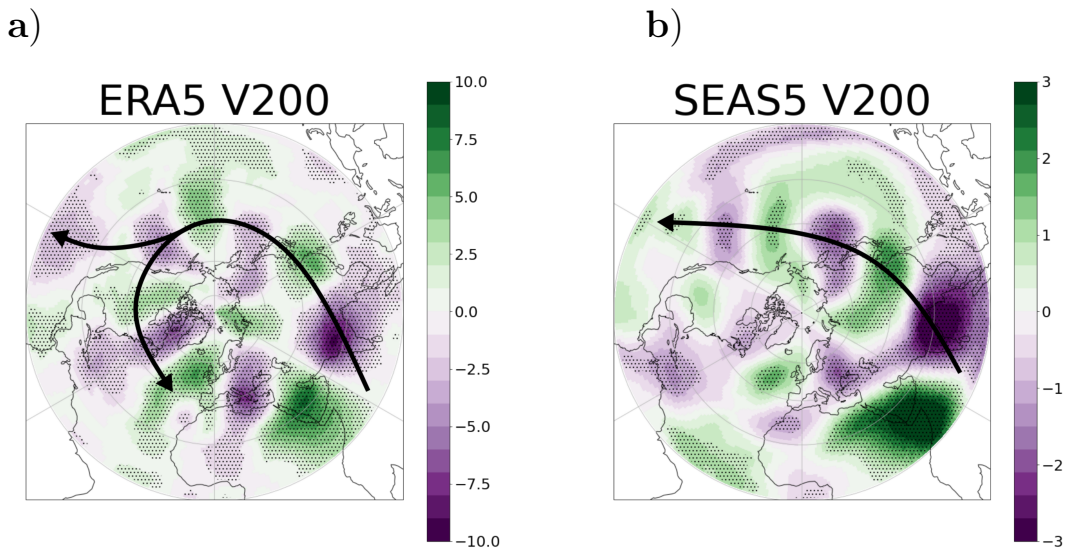


Figure 7.1: **Northern Hemisphere wave train in 2019/2020** depicted in meridional wind. DJF 2019/2020 anomalous V200 [m/s] wind in **a)** ERA5 and **b)** SEAS5. Anomalies are calculated against the 1981-2020 climatological average. Arrows symbolise the wavetrain path in ERA5 and SEAS5. ERA5 stippling denotes significant areas calculated with a 2-sided Student's t-test at 5%. Model stippling denotes significance and is calculated with a 2-sided bootstrapping at 5%.

A broader overview of the quasi-stationary Rossby wave train comes from the analysis of the C3S models individually (Figure 7.2). As before in chapter 4.2, I show the C3S forecasts separated into the different model centres and as the multi-model mean and compare them to the ERA5 conditions of 2019/2020. As discussed before, the ability of the models to accurately reproduce the Rossby wave train gives an indication of the importance of the wave train in the models.
Compared to the clear wavetrain in ERA5 (Figure 7.2 a), all models show a weaker wave train. The multi-model-mean wavetrain (Figure 7.2 b) agrees with ERA5 in the Indian Ocean sector and into the North Pacific. However, from the region of the Aleutian cyclone, the wavetrain in the MMM has a pathway further south and is much weaker (even considering the large ensemble size). Analysing the individual models, the UKMO (Figure 7.2 d) and the DWD (Figure 7.2 e) show a consistent wavetrain crossing North America (and even in these models, the amplitudes over North America are small). As discussed before, the SEAS5 (Figure 7.2 c) wave train reflects southward over the North Pacific. Both the CMCC (Figure 7.2 f) and Météo France (Figure 7.2 g) models do not manage to reproduce the wave train well. Over the Indian Ocean sector, these two models forecast a weaker wind dipole (also evident

from the weaker precipitation dipole (Figure 4.3). This too small amplitude leads to larger forecast errors over the North Pacific and both models do not have a consistent wave train crossing North America into the North Atlantic region.
Since all these models managed to reproduce the Z500 field in the North Atlantic with a good accuracy (Figure 4.4 (apart from CMCC)), I conclude that the less well forecasted wave train is likely not the only teleconnection mechanism between the IOD and the NAO in these models. To get a better statistical understanding of the connection between the wave train and the NAO, I use the large ensemble of the OpenIFS@Home.

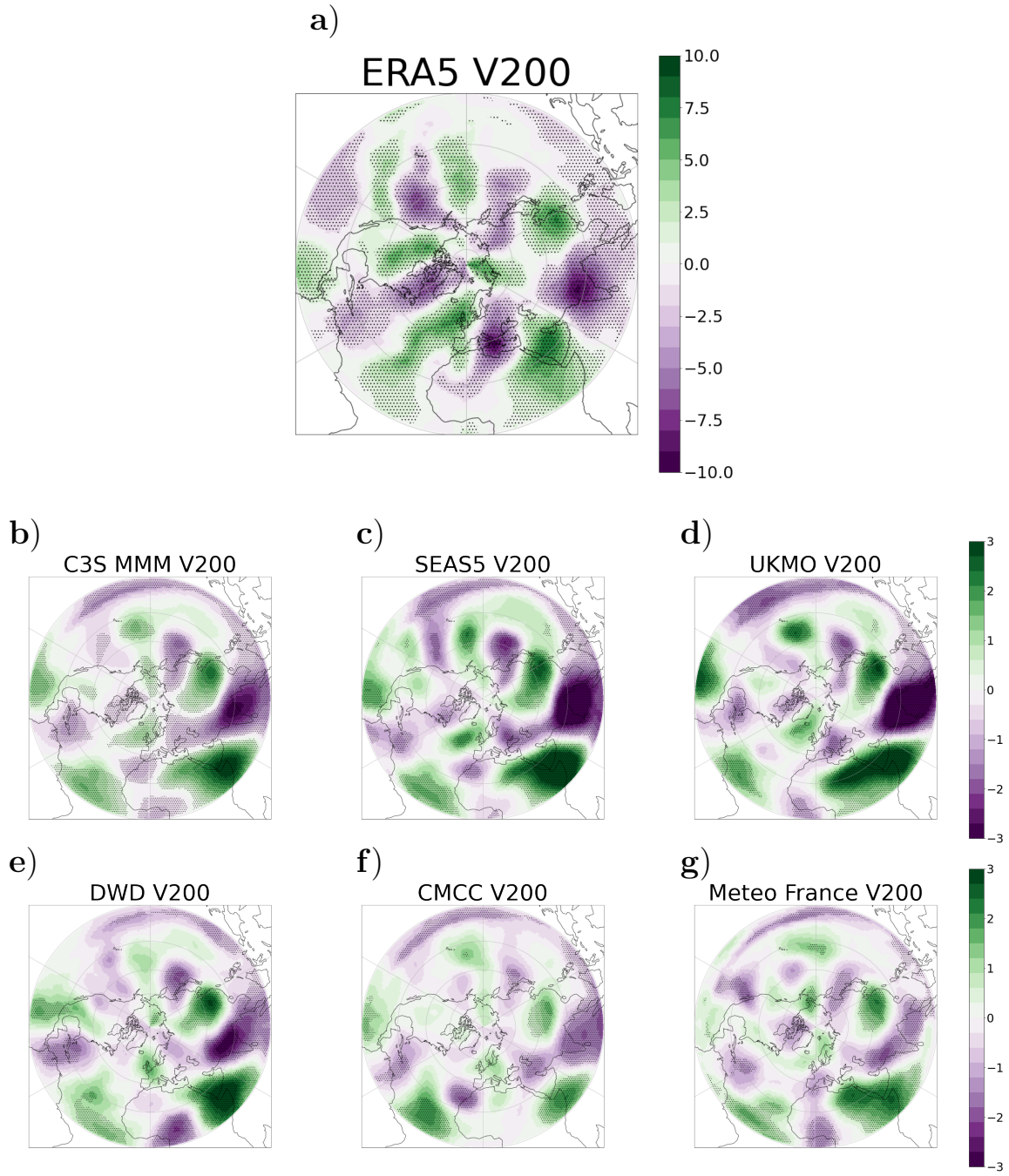


Figure 7.2: **V200 from C3S models in DJF 2019/2020** compared to ERA5. **a)** ERA5, **b)** C3S multi-model mean, **c)** SEAS5, **d)** UKMO, **e)** DWD, **f)** CMCC, **g)** Météo France [m/s]. Anomalies are calculated against the 1993-2016 climatological average. ERA5 stippling denotes significant areas calculated with a 2-sided Student's t-test at 5%. Model stippling denotes significance and is calculated with a 2-sided bootstrapping at 5%.

7.1 OpenIFS@Home control experiments

With the large ensemble of the OpenIFS@Home I investigate the statistics of the ensemble in more detail and gauge the possible extreme cases of the 2019/2020 winter. The OpenIFS@Home ensemble consists of 1613 ensemble members of the winter 2019/2020. These members are compared to the 1981-2020 hindcast run on the Oxford servers and to a 100 member run of the winter 2019/2020.
The OpenIFS@Home ensemble is initialised on the 01.11.2019 with 200 initial conditions. To create a 2000 member ensemble, each initial condition is multiplied by 10 members created through the stochastic physics parametrisations. The results analysed here consist of the 1613 members that ran successfully out of the 2000 members started. More detail about the model and the initialisation is in chapter ([Methods OpenIFS model 3.1]), where I describe the OpenIFS and the setup.

7.1.1 Composites

To analyse the connections between different parts of the climate system I am using the large size of the OpenIFS@Home ensemble to create composites of ensemble members with a particular characteristic. Here, I investigate the connection between the wave train in the North Pacific and the AO/NAO.
To test the hypothesis that the North Pacific quasi-stationary Rossby wave train has a direct influence on the NAO, I select ensemble members of the OIFS@Home that show a particularly strong/weak (ERA5 like/un-like) wave train. If the hypothesis is correct, it is expected that the composite mean of strong wave train members also shows a more positive NAO. For this purpose I compare the meridional wind at 200 hPa (V200) over the North Pacific (20-70°N, 100-230°E (regions of the V200 shown in Figure 7.3) from ERA5 to each ensemble member of the model. I use the field correlation between ERA5 (Figure 7.3 a) and each ensemble member to evaluate the similarity of the wave train between ERA5 and the model ensemble. The entire ensemble is separated into a positive composite (Figure 7.3 b), a neutral composite (Figure 7.3 c), and a negative wave train (Figure 7.3 d). Ensemble members with a field correlation of > 0.5 are combined in the positive composite, members with < -0.1 in the negative composite, and members in between in the neutral composite. The result is a roughly even split of 472 positive, 651 neutral, and 490 negative members.
Since the selection is done on V200 over the North Pacific, the composite mean V200

over the North Pacific are very different. The positive composite shows a signal that is almost identical to the ERA5 wave train in phase and magnitude. The neutral and negative composite, meanwhile, show a very weak and opposite wave train, respectively. This result is expected as the composites were selected to be this way.
The anomalous Z500 composite fields (based on the wave train selection) of the Northern Hemisphere based on the wave train selection are less clear. All composite means (Figure 7.4 b-d) show a positive AO pattern that has a similar shape to ERA5 (Figure 7.4 a), but with a weaker magnitude (similar to the full ensemble mean). While the positive wave train composite (Figure 7.4 b) shows a stronger AO with some regions being significant, the composite mean of both the neutral (Figure 7.4 c) and negative (Figure 7.4 d) wave train cases still show a positive AO. The largest differences between the composites exist over the Pacific and western America. The differences in the North Atlantic region are smaller and hard to evaluate. If the wave train was responsible for the positive AO/NAO, a more distinct composite mean would be expected and ensemble members with a weak or opposite wave train would show a neutral or negative AO/NAO.

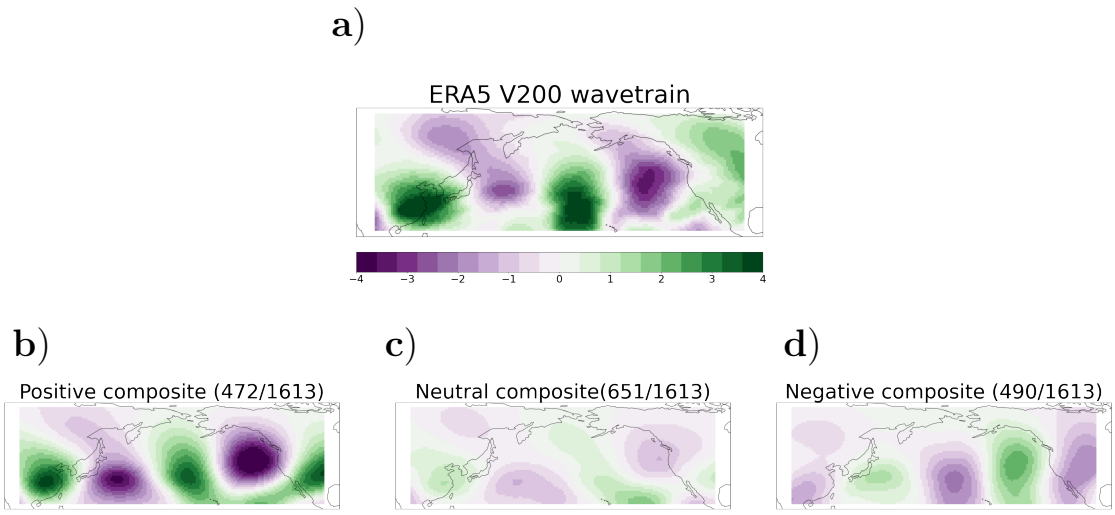


Figure 7.3: **Wavetrain composite in a large ensemble** with the OpenIFS@Home. V200 [m/s] anomaly in the North Pacific in **a)** ERA5, **b)** positive (ERA5 like) composite with 472/1613 members chosen, **c)** neutral composite with 651/1613 members chosen, and **d)** negative (ERA5 un-like) composite with 490/1613 members chosen. Anomalies are calculated against the 1981-2020 climatological average.

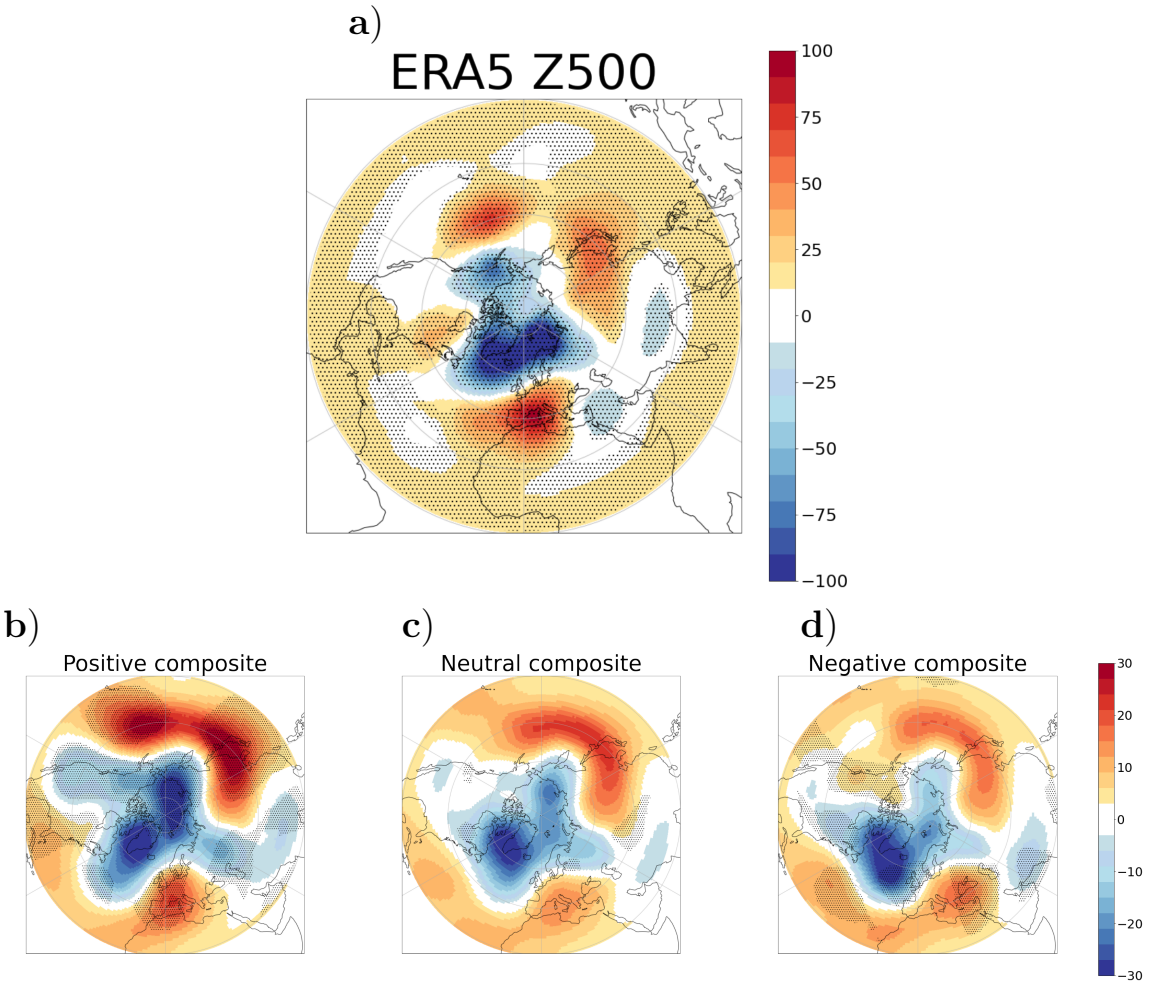


Figure 7.4: **Large ensemble composite AO** calculated from the members used to create the wave train composite (Figure 7.3). Z500 [m] anomaly in **a)** ERA5, **b)** positive (ERA5 like) composite with 472/1613 members chosen, **c)** neutral composite with 651/1613 members chosen, and **d)** negative (ERA5 un-like) composite with 490/1613 members chosen. Anomalies are calculated against the 1981-2020 climatological average. Model stippling denotes significance and is calculated with a 2-sided bootstrapping at 5%.

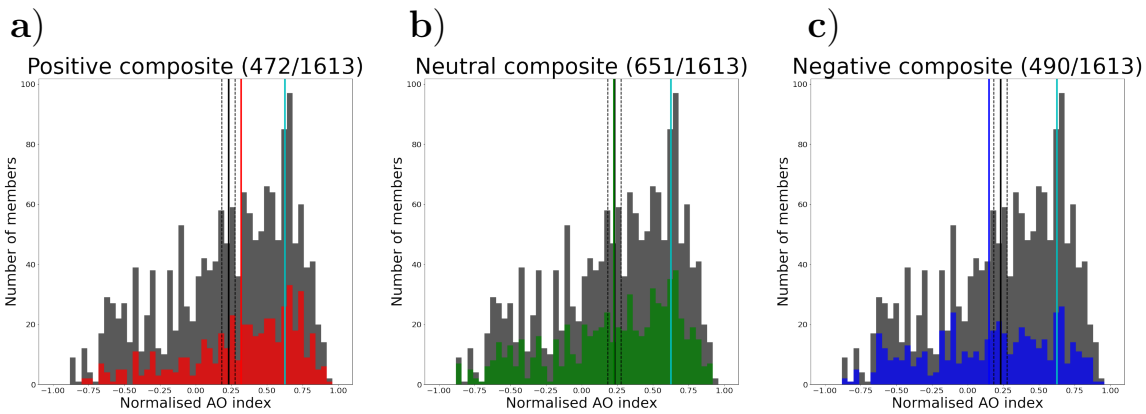


Figure 7.5: **AO indices in the large ensemble** from the OpenIFS@Home. Depiction of the scaled Arctic Oscillation index, by correlating the Z500 fields between 20°N and 90°N in 2019/2020 with the 1.EOF of that region in the hindcast in each ensemble member (grey bars). Black line is the full ensemble mean of the AO indices. Black dotted line is the 5% significance threshold from bootstrapping selecting 500 randomly chosen ensemble members. Coloured bars are the ensemble members chosen from the strength of their North Pacific wave train (Figure 7.3). **Left** for the positive composite, **Middle** for the neutral composite, and **Right** for the negative composite. Coloured lines show the composite mean of the AO from the individual composites. ERA5 2019/2020 AO as a reference is the cyan line.

To leverage the benefits of the large ensemble in a better way, I calculate the AO and NAO indices in each ensemble member, in order to display these indices in a more comprehensive way. For this purpose, the AO is calculated on the model hindcast (1981-2020) as EOF1 of Z500 between 20°N and 90°N (EOF function from Andrew Dawson https://ajdawson.github.io/eofs/latest/). The AO of each ensemble member in 2019/2020 is then calculated as the field correlation between this EOF1 and the Z500 field of each ensemble member. This method shows the AO index of all 1613 members and the composite distributions in a concise way (Figure 7.5). The mean AO of the ensemble is calculated as the mean of all ensemble AO's (or as the mean of all composite AO's). The distribution of all ensemble members (grey bars in Figure 7.5) shows a general shift towards more positive AO indices, but there are still plenty of ensemble members with a neutral and even negative AO. Since the real (ERA5) AO was positive in this winter and the full ensemble mean did manage to reproduce this signal, the individual ensemble members should tend towards a positive AO phase. The same distribution is generally true for the composites as well, but with some differences between them (coloured bars in Figure 7.5). While the positive composite shows a distribution of ensemble members slightly shifted towards more positive AO values (Figure 7.5 a), the neutral composite shows a distribution similar

to the full ensemble mean (Figure 7.5 b) and the negative composite contains slightly more ensemble members with negative AO's (Figure 7.5 c). This is also evident from the composite averages (solid coloured lines in plots), where the mean of the positive composite (red) is more positive than the full ensemble mean (black line) and lies outside the 5% interval (black dotted line). On the other hand, the negative composite mean is more negative than the full mean and also lies outside the confidence interval.

The fact that ensemble members with a positive (ERA5 like) wave train show an on average more positive AO supports the hypothesis that there is an impact of the wave train on the AO. However, since there are still members with a neutral and even negative AO in the positive composite, the wave train can not be the only driving factor of the positive AO in this winter. The conclusion of this analysis is that an ERA5 like wave train increases the likelihood of a positive AO, but is not on its own sufficient to create the positive AO.

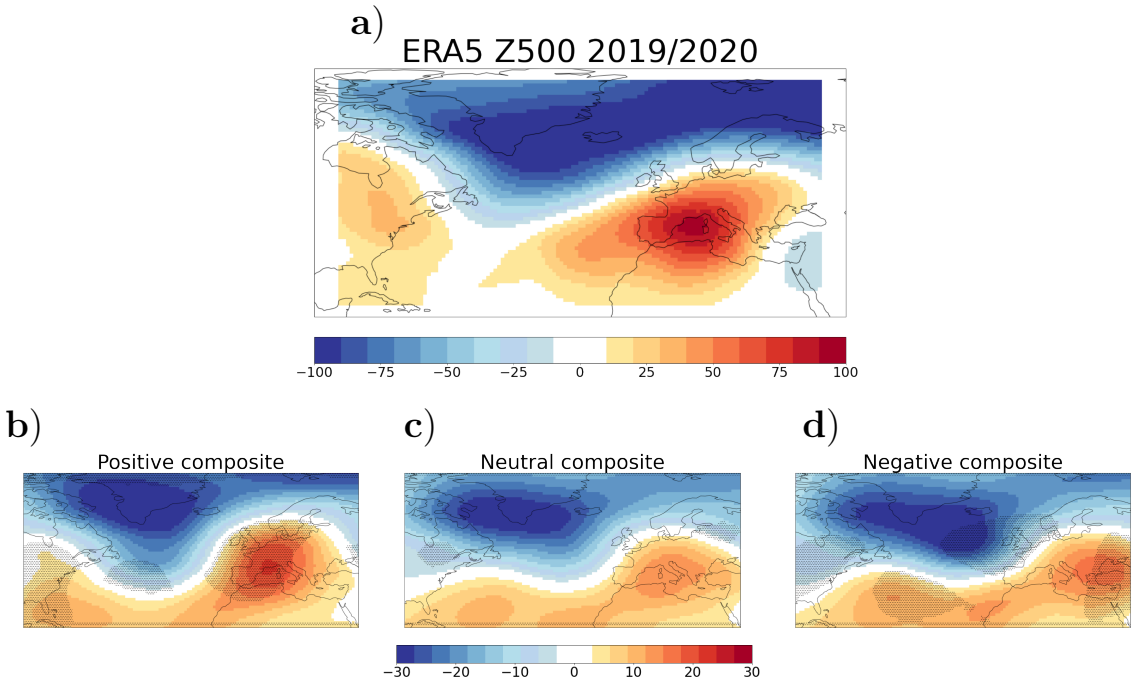


Figure 7.6: **Large ensemble composite NAO** calculated from the members used to create the wave train composite (Figure 7.3). Z500 [m] anomaly in **a)** ERA5, **b)** positive (ERA5 like) composite with 472/1613 members chosen, **c)** neutral composite with 651/1613 members chosen, and **d)** negative (ERA5 un-like) composite with 490/1613 members chosen. Anomalies are calculated against the 1981-2020 climatological average. Model stippling denotes significance and is calculated with a 2-sided bootstrapping at 5%.

The analysis is repeated for the NAO. The same composite members are selected based on the wave train. The composite mean maps of Z500 in the North Atlantic region are similar between the three composites with all of the composites having a positive NAO (Figure 7.6). As evident in the maps of the AO (Figure 7.4), the largest differences between the composites overall, are over the Pacific and North America, while the differences over the North Atlantic are smaller. This indicates that the wave train has a weaker impact on the NAO than on the whole AO. The analysis of the NAO in individual ensemble members supports the claim that the impact of the wave train is weaker on the NAO than on the full AO. The positive composite (Figure 7.7 a) still shows a slight shift towards more positive NAO indices, while the negative composite (Figure 7.7 c) contains more members with a negative NAO with the neutral composite (Figure 7.7 b) again in the middle. However, the difference is less pronounced than the difference of the AO indices. The positive and negative composite means (coloured lines in Figure 7.7) are not outside the 5% significance values anymore. This smaller NAO differences between positive and negative wave train composite shows again that more than the North Pacific Rossby wave train is responsible for the positive NAO.

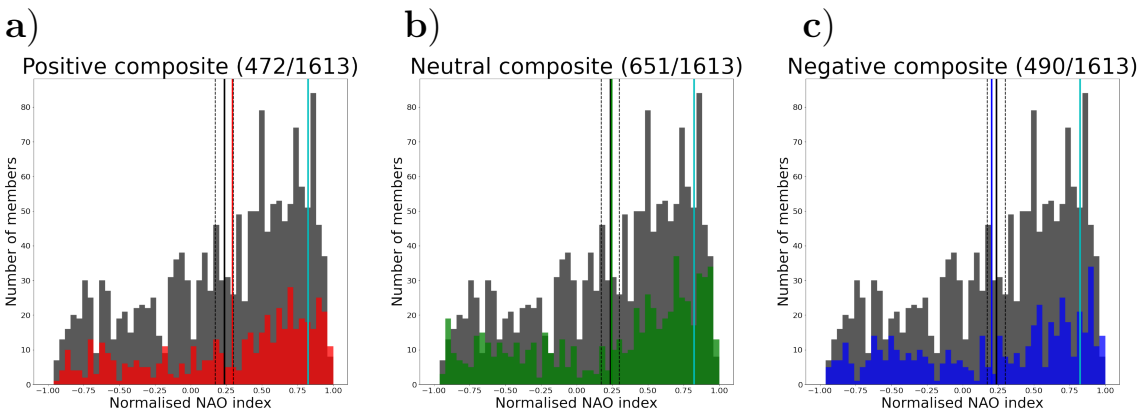


Figure 7.7: **NAO indices in the large ensemble** from the OpenIFS@Home. Depiction of the scaled North Atlantic Oscillation index, by correlating the Z500 fields between $20° - 80°N, 90°W - 40°E$ in 2019/2020 with the 1.EOF of that region in the hindcast in each ensemble member (grey bars). Black line is the full ensemble mean of the NAO indices. Black dotted line is the 5% significance threshold from bootstrapping selecting 500 randomly chosen ensemble members. Coloured bars are the ensemble members chosen from the strength of their North Pacific wave train (Figure 7.3). **Left** for the positive composite, **Middle** for the neutral composite, and **Right** for the negative composite. Coloured lines show the composite mean of the NAO from the individual composites. ERA5 2019/2020 NAO as a reference is the cyan line.

This chapter shows that:

- ERA5 shows a quasi-stationary Rossby wave train in the North Pacific.
  - At the North American coast it splits into a southward travelling part and a part crossing North America.
- SEAS5 is not able to reproduce the wave train crossing North America, but does manage to forecast the NAO correctly.
- Large composite means from the OpenIFS@Home show that slightly more ensemble members with an ERA5-like wave train have a positive AO.
- There are still a lot of ensemble members with an ERA5-like wave train with a neutral or negative AO.
- For the NAO indices the difference between members with and ERA5-like and and ERA5-unlike wave train are even smaller.
- This analysis suggests that the quasi-stationary Rossby wave train was not the main teleconnection between the IOD, the North Pacific, and the NAO.

Chapter 8

Eddy, mean-flow interactions

In this chapter I investigate the eddy, mean-flow interactions in the North Pacific and North Atlantic as an alternative teleconnection mechanism connecting these two regions. The previous chapters have shown that many models did not reproduce the proposed teleconnection mechanisms well (Stratospheric pathway chapter 6 and Rossby wave train chapter 7). However, these models surprisingly still forecast the NAO correctly. Here, I show that in the North Pacific the decay of the synoptic eddies interacts in such a way with the mid-latitude jet, that it is shifted northward and extended. This signal in the jet shift is observable crossing North America and again in the North Atlantic region where the jet is similarly shifted northward and extended. This teleconnection between the North Pacific and the North Atlantic offers an alternative pathway between those regions and allows models that do not reproduce the other teleconnection mechanisms well, to still forecasts the NAO correctly.

An alternative teleconnection mechanism in addition to the Rossby wave train are shifts in the mid-latitude jets and their interaction with synoptic eddies (Rivière and Drouard, 2015 [64]). The latitude and strength of the seasonal mid-latitude jet interacts strongly with the shorter lived eddies that propagate along the axis of the jet (Drouard et al. 2013 [15]). The nature of the eddies (cyclonic/ anti-cyclonic) and where they decay can shift and weaken (or strengthen) the jet. To investigate this interaction and teleconnection, I use the E-Vectors developed in Hoskins et al. (1983 [32], see chapter[Methods E-Vectors 3.5] for more details).

8.1 Climatological E-Vectors

I test the eddy, mean-flow interactions in ERA5, SEAS5, and the OpenIFS. A special focus is here on the SEAS5 to see if the eddy, mean-flow teleconnection can close the gap from the North Pacific to the North Atlantic, since the Rossby wave train in SEAS5 does not cross North America (see chapter [Rossby wave train 7]) and neither is the polar stratosphere in the correct phase (see chapter [Stratosphere 6]). First I compare the climatological E-Vectors in SEAS5 and the OpenIFS to ERA5 to test the ability of these models to replicate the reanalysis.

The climatological E-Vectors are separated into a zonal component (left column Figure 8.1) and meridional component (right column Figure 8.1) (contours are separated into components, vectors are the full E-Vectors). The components show a high agreement between ERA5 (top row Figure 8.1), SEAS (middle row Figure 8.1) and OpenIFS (bottom row Figure 8.1). In ERA5 the zonal component of the E-Vectors is strongest in the North Pacific and North Atlantic, in the region where the mid-latitude jet is located. The Vectors all point eastward in these regions, with the Atlantic showing slightly higher values than the ones in the Pacific. In comparison, the SEAS5 zonal E-Vectors are very close in magnitude and location to the ERA5 ones, while the OpenIFS has slightly higher values in the Atlantic and slightly lower values in the Pacific.

The meridional component (right side Figure 8.1) of the climatological E-vectors has a very zonally symmetric structure in ERA5. On the southern flank of the climatological jet location, the E-Vectors are pointing southward, while they are pointing northward at the northern flank of the climatological jet location. This meridional dipole extends over the North Pacific, North America, the North Atlantic and Europe, while being weaker over central Asia. Over the east coast of North America the dipole of the meridional E-Vectors is also slightly weaker. In this region the Pacific jet has not a large influence any more and the Atlantic jet only starts to pick up strength in this location. SEAS5 and the OpenIFS both manage to reproduce the magnitude and pattern well. Over the North Pacific, both models show slightly smoother fields than ERA5. This is likely connected to the nature of ensembles of the models, compared to the single realisation of reality (ERA5). These climatological E-Vectors are in agreement with calculations of the E-Vectors from the ERA-40 Atlas (ERA-40 Atlas https://sites.ecmwf.int/era/40-atlas/docs/section_D15/parameter_zwa6-2dea250hpa.html) and the analysis from Hoskins et al. (1983 their Figure 6a [32]).

The high agreement of the model climatologies with ERA5 gives confidence that the models are able to accurately represent the eddy, mean-flow interactions and that I can investigate the E-Vectors as a teleconnection mechanism.

To test the feedback between the eddies and the mean flow in ERA5 and the OpenIFS again, I calculate the eddy feedback parameter (EFP) following Hardiman et al. (2022 [26]). They find that models with a greater eddy feedback show stronger teleconnections between ENSO and the AO. At the same time, models with stronger eddy feedback are generally better at predicting the AO. To evaluate whether the OpenIFS shows a reasonable interaction between the eddies and the jet I compare its eddy feedback here to ERA5.
For this purpose I use the methods described in Hardiman et al. (2022 [26]) and in chapter 3.5.1. With the 200 hPa wind in the North Atlantic sector (50 - 70°N and 0 - 70°W) between 1981-2020, ERA5 shows an eddy feedback parameter of 0.26. The OpenIFS EFP in the same time is 0.23, showing that the OpenIFS has an eddy feedback in the same range as ERA5.
This method is very contingent on the data used and the exact methodology. For example, an extension of the North Atlantic area towards the south (25 - 70°N) yields much lower EFP values of 0.02 in ERA5. Similarly, the timing when the temporal and spatial averages are applied changes the values of the EFP strongly. For this reason, the EFP values obtained here can not directly be compared to the ones obtained by Hardiman et al. (2022 [26]). Nevertheless, the values obtained here can be used to compare ERA5 and the OpenIFS and shows that the OpenIFS has a reasonable (albeit too low) eddy feedback.
To show the location of the strongest average eddy acceleration I show the acceleration term (Hardiman et al., 2022 [26] their equation 1 or chapter 3.5.1) averaged over the DJF 1981-2020 period in ERA5 and the OpenIFS (Figure 8.2). The Northern Hemisphere jet streams in the North Pacific and North Atlantic are clearly visible in both data sets. In both jet stream regions, the southern flank of the jet is generally dominated by negative values, while on the northern flank the eddies accelerate the jet. In this climatological mean, there are no major differences in location or strength between ERA5 (Figure 8.2a) and the OpenIFS (Figure 8.2b). These regions of increased eddy acceleration agree well with the climatological E-Vectors (Figure 8.1) and calculations of the eddy kinetic energy (not shown).
In the Southern Hemisphere a band of increased eddy acceleration is evident. The region of this increased eddy acceleration is roughly where the mid-latitude jet of the

Southern Hemisphere is located. The values are lower than in the Northern Hemisphere, as the jet and the eddies are less strong in the austral summer in the Southern Hemisphere.

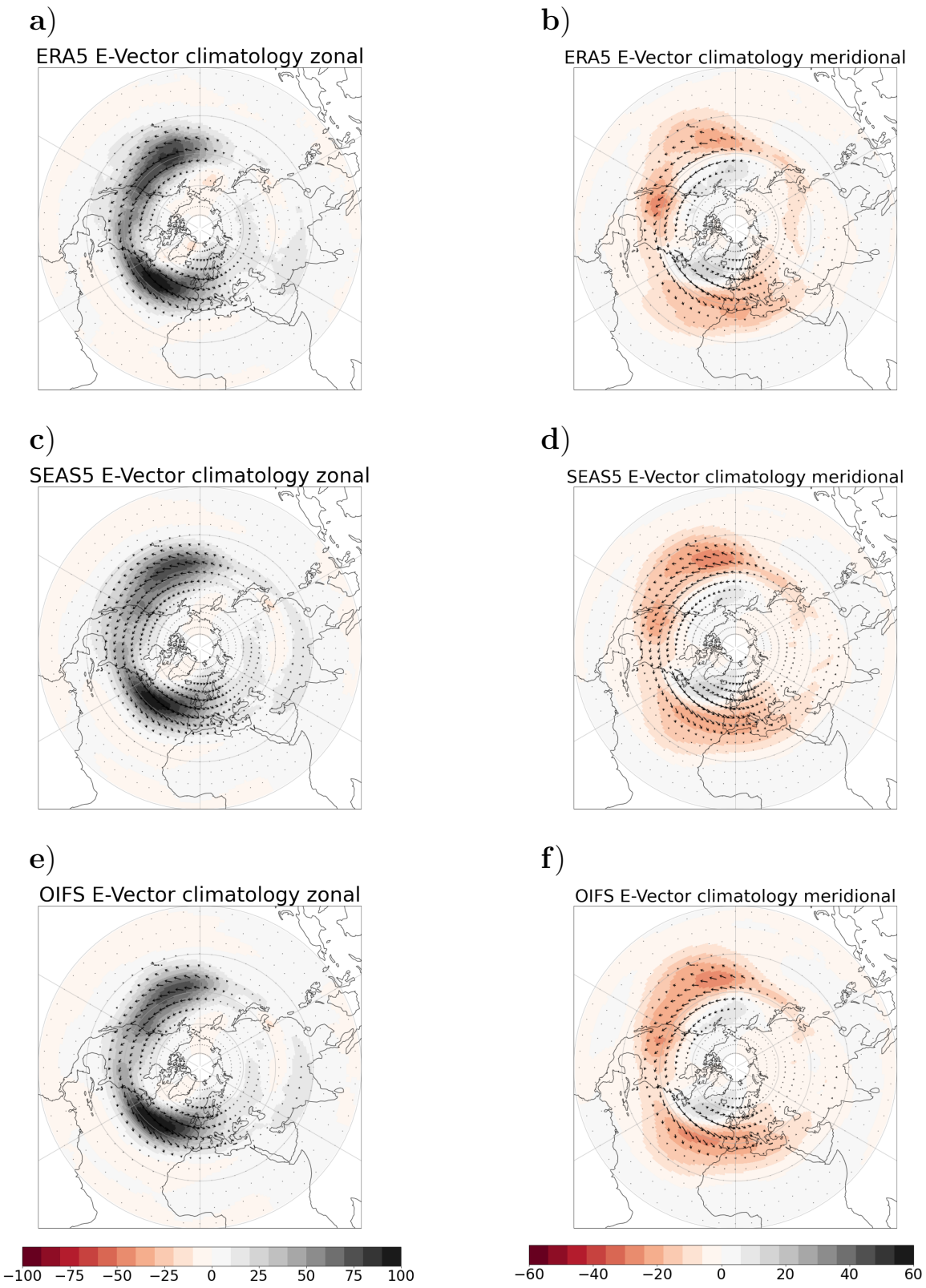


Figure 8.1: **Climatological E-Vectors in models** compared to ERA5. Vectors are full E-Vectors $[m^2/s^2]$ in **Top** row ERA5, **Second** row SEAS5, and **Bottom** row OpenIFS. Shading are the components of the E-Vectors, with **Left** the zonal component $(\overline{v'^2 - u'^2})$ and **Right** the meridional component $(-\overline{u'v'})$.

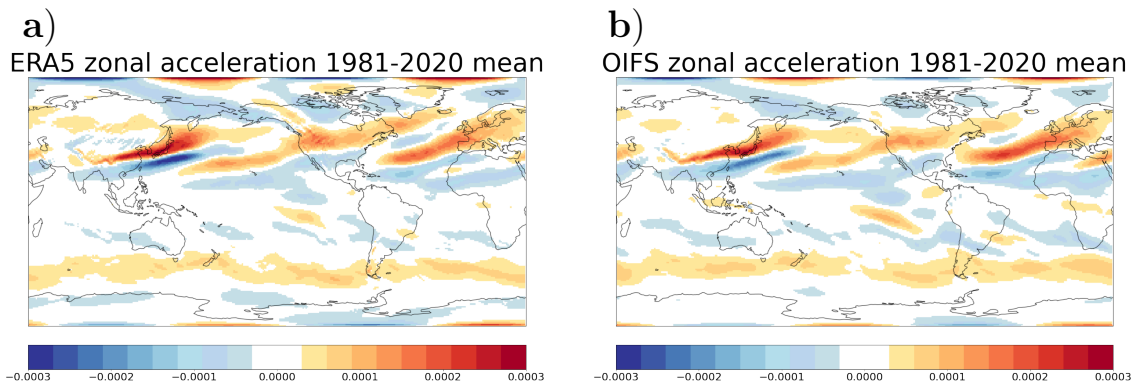


Figure 8.2: **Climatological eddy acceleration** from ERA5 and OpenIFS. Eddy acceleration is in $[m/s^2]$ **a)** ERA5, **b)** OpenIFS. Calculated from daily data and averaged over 1981-2020.

8.2 2019/2020 E-Vector teleconnection

I use the E-Vector anomalies against the above discussed climatological average to identify how the eddies interacted with the mean flow in the 2019/2020 winter. I am comparing the results of the E-Vector anomalies to the jet-stream anomalies to identify regions where the properties of the jet are altered by interaction with the eddies. First, I examine ERA5.

The E-Vector anomalies of ERA5 (Figure 8.3 b-c) show a consistent eastward and southward signal over most of the North Pacific, North America, and the North Atlantic. For the purpose of investigating the impact of the eddies on the jet, the meridional component of the E-Vectors is of high importance. Rivière and Drouard (2015 [64]) showed that specifically in the jet exit region of the Pacific jet, the meridional component is of high importance in preconditioning the Atlantic jet. The southward pointing E-Vectors in 2019/2020 show more energy from the eddies refracted equatorward which shifts the jet northward, strengthens it and is associated with a positive NAO (Drouard et al., 2013 [15]). The consistent southward pointing E-Vector anomalies in the North Pacific that continue over North America indicate that the Pacific jet is shifted towards the north. This is evident in the zonal wind anomalies at 200 hPa (U200) in ERA5 (Figure 8.3 a). The Pacific jet is shifted towards the north from its climatological position and slightly extended. At the American-Atlantic coast, where the Atlantic jet starts, the meridional E-Vectors are again pointing southward and shift the jet northward (Figure 8.3 c). Again, this is evident in the jet itself (U200) that is shifted towards the north and extended. This shift of the jet through

the interaction with the eddies leads to a positive NAO in the North Atlantic sector.

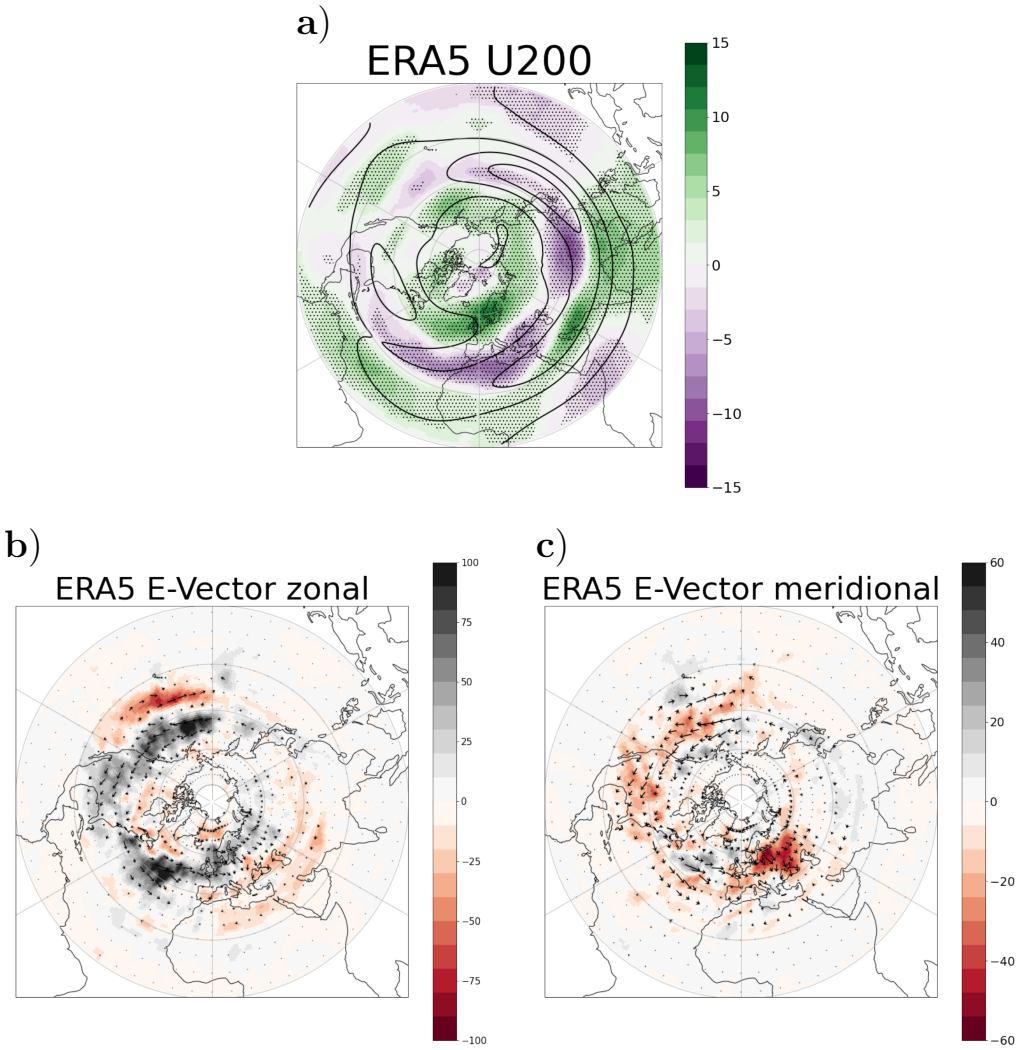


Figure 8.3: **ERA5 mean flow and eddies in 2019/2020**. Relation between shifts in the mid-latitude jet, identified from 200 hPa zonal wind and eddy interactions with the jet, identified from E-Vector anomalies. **a)** U200 [m/s] climatological average (contours) and 2019/2020 anomalies (shading). **b)** E-Vector anomalies $[m^2/s^2]$, with full E-Vectors (vectors) and zonal component (shaded). **c)** E-Vector anomalies, with full E-Vectors (vectors) and meridional component (shaded). Anomalies are calculated against the 1981-2020 climatological average. ERA5 stippling denotes significant areas calculated with a 2-sided Student's t-test at 5%

For the comparison between ERA5 and the model ensemble means, it is important to note, that the magnitude of the anomalies differs between ERA5 compared to the ensemble mean of SEAS5 and the OpenIFS. Where the anomalies in ERA5 have the same magnitude as the climatological average, the anomalies in SEAS5 and OpenIFS

are about 5 times smaller than the climatological average. Similar to the anomalies of pressure and wind fields, the ensemble mean gives lower anomalies compared to the single realisation of ERA5 (Scaife and Smith, 2018 [70]). Since the E-Vectors are the square (or multiplication) of the wind fields, this even smaller magnitude in the ensemble mean makes sense. Single ensemble members of both SEAS5 and OpenIFS do show a similar magnitudes compared to ERA5 and climatological average.

The ensemble mean E-Vectors of SEAS5 (Figure 8.4 b-c) show a high agreement with the ERA5 (Figure 8.3 b-c) results (albeit with lower magnitude). Compared to ERA5, the E-Vector fields in SEAS5 are generally smoother, since the process of creating the ensemble mean averages out a lot of the smaller scale influences of individual eddies. These SEAS5 E-Vector anomalies show more eastward and southward pointing E-Vectors, starting from the North Pacific and crossing over North America into the North Atlantic region. One larger difference between ERA5 and SEAS5 is the absence in SEAS5 of the westward pointing E-Vectors to the north of Hawaii, that are present in ERA5. This is likely due to the differences between ERA5 and SEAS5 over Alaska and the west coast of North America that are also present in other fields (see chapter [ECMWF model forecast skill 4.1). Nevertheless, the Pacific jet exit region is within the region of enhanced eddy, mean-flow interactions, indicating again that the Atlantic jet is preconditioned here towards a northward and extended phase. The jet itself (U200 Figure 8.4 a) is slightly northward shifted and extended in the Pacific and Atlantic sector. This is a difference compared to the ERA5 jet, that is mainly shifted northward and only slightly extended. The differences between the SEAS5 and ERA5 jets are likely a result of the different dynamics in the North Pacific described before. The SEAS5 E-Vector forecast and the associated jet shifts are still comparatively good and project onto a positive AO/NAO. The eddy, mean-flow mechanism appears to be high importance for SEAS5, since SEAS5 did not manage to reproduce the Rossby wave train that crosses North America (chapter [Rossby wave train teleconnection 7), nor the strong positive stratospheric polar vortex (chapter [Stratosphere in reanalysis and forecast 6]). Therefore, the eddy, mean-flow interactions serve as a possible mechanism that closes the gap between the North Pacific and North Atlantic in SEAS5 and allows SEAS5 to predict the NAO correctly event when it is missing the other mechanisms.

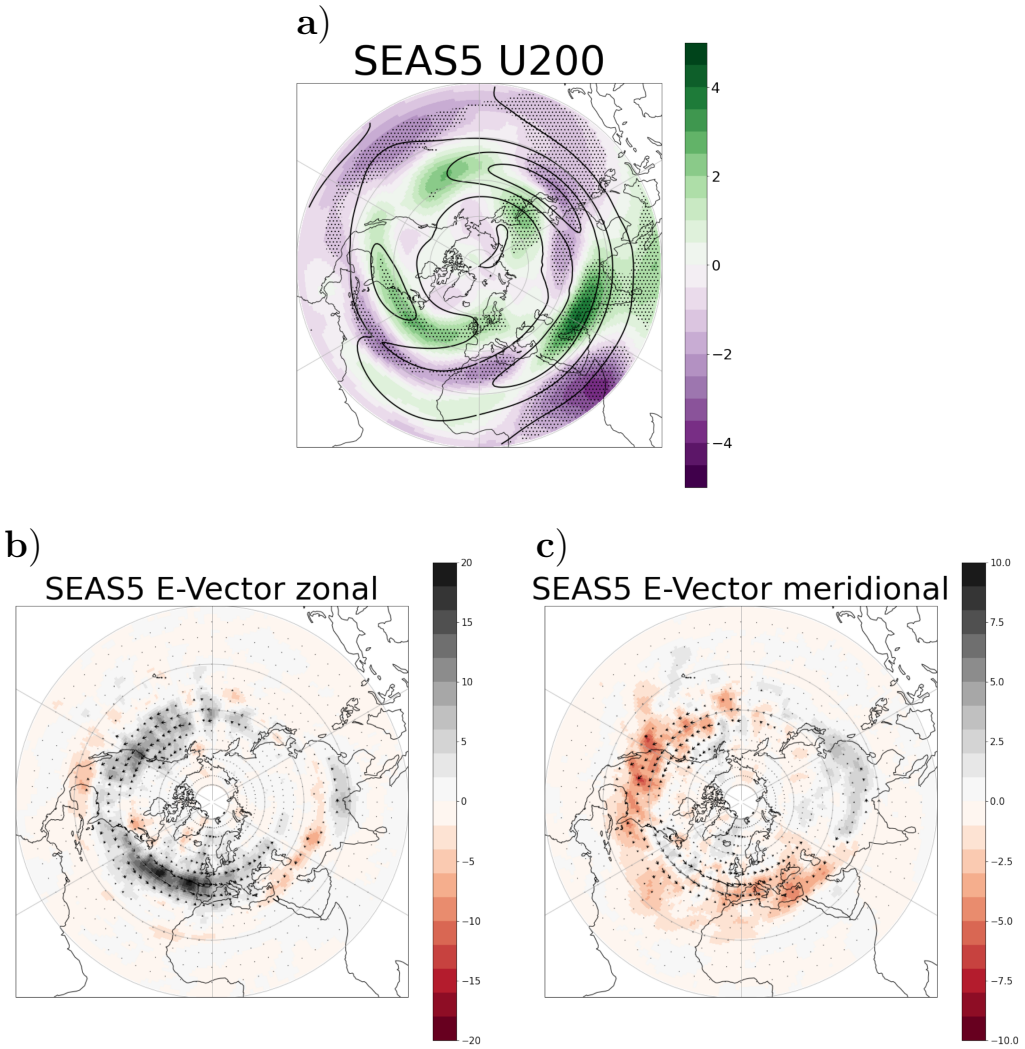


Figure 8.4: **SEAS5 mean flow and eddies in 2019/2020**. Relation between shifts in the mid-latitude jet, identified from 200 hPa zonal wind and eddy interactions with the jet, identified from E-Vector anomalies. **a)** U200 [m/s] climatological average (contours) and 2019/2020 anomalies (shading). **b)** E-Vector anomalies $[m^2/s^2]$, with full E-Vectors (vectors) and zonal component (shaded). **c)** E-Vector anomalies, with full E-Vectors (vectors) and meridional component (shaded). Anomalies are calculated against the 1981-2020 climatological average. Stippling denotes significance and is calculated with a 2-sided bootstrapping at 5%.

In the OpenIFS the major signals are again reproduced well with regards to ERA5 (again with lower amplitude) (Figure 8.5 b-c). The individual components of the E-Vectors show some differences in the North Pacific. Where in ERA5 both zonal and meridional component of the E-Vectors on their own showed large continuous anomalies from the North Pacific to the North Atlantic, the zonal component drops off at the American coast in OpenIFS. On the other hand, the meridional component of the E-Vectors only picks up in this region at the American coast and is weak before that. As described before, the region at the American-Pacific coast is of high importance, since it sets the conditions for the Atlantic jet (Rivière and Drouard, 2015 [64]). Even though there are some differences between the OpenIFS and ERA5, the fact that the E-Vectors are pointing southward and crossing North America is sufficient to have the Pacific jet influence the Atlantic jet and shift it northward. Comparing the jet anomalies of the OpenIFS in 2019/2020 (U200 Figure 8.5 a) to the climatological average, it is evident that the jet is shifted to the north from its average position and slightly stronger. These jet shifts agree very well with the ones observed in ERA5 and are again related to a positive AO/NAO.

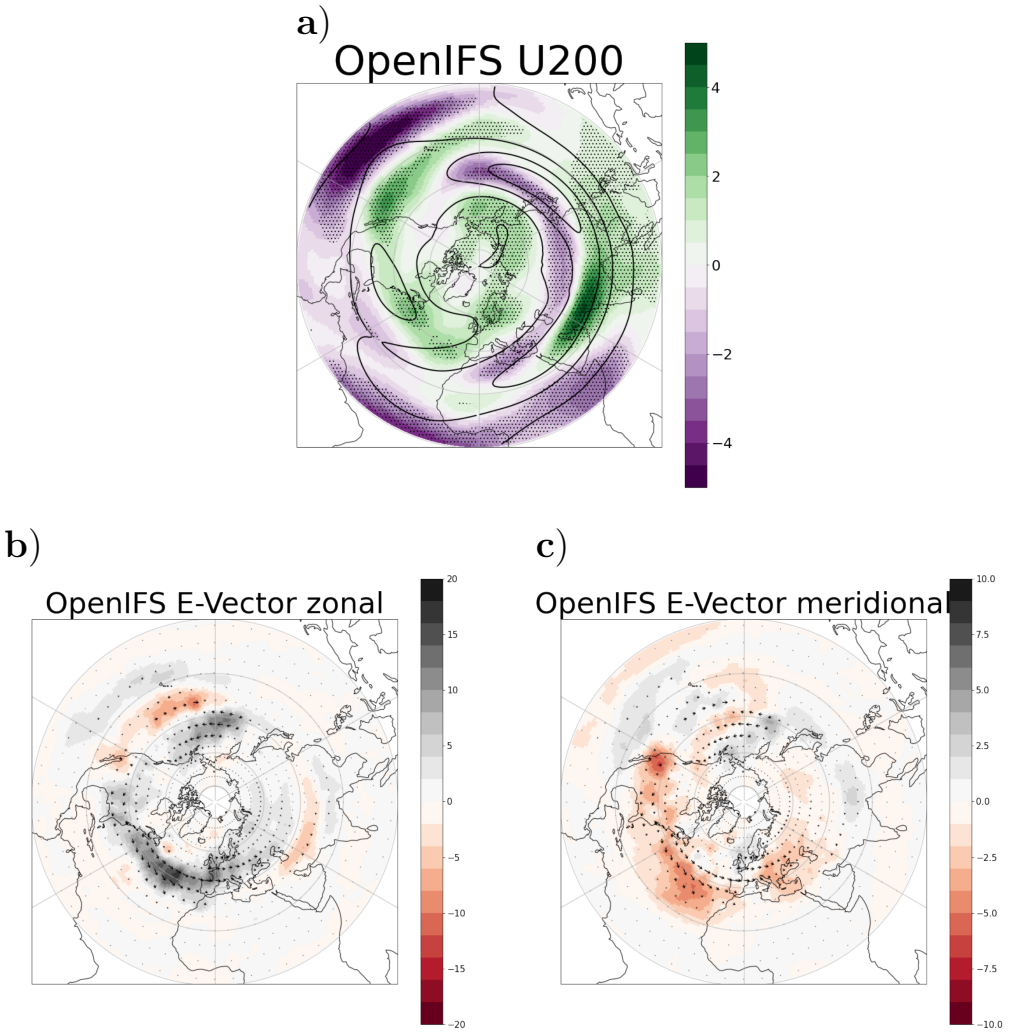


Figure 8.5: **OpenIFS control experiment mean flow and eddies in 2019/2020**. Relation between shifts in the mid-latitude jet, identified from 200 hPa zonal wind and eddy interactions with the jet, identified from E-Vector anomalies. **a)** U200 [m/s] climatological average (contours) and 2019/2020 anomalies (shading). **b)** E-Vector anomalies [m^2/s^2], with full E-Vectors (vectors) and zonal component (shaded). **c)** E-Vector anomalies, with full E-Vectors (vectors) and meridional component (shaded). Anomalies are calculated against the 1981-2020 climatological average. Stippling denotes significance and is calculated with a 2-sided bootstrapping at 5%.

As a reference between a positive and negative AO/NAO, I am comparing the IO only experiment (with the positive AO) to the Pacific Ocean only experiment (with the negative AO). The experiments are described in detail in chapter [OpenIFS experiments 5.2]. The hypothesis here is that that the Indian Ocean Dipole has a positive effect on this teleconnection and the E-Vector mechanism is strengthened in the IO only experiment. Meanwhile, the Pacific only experiment shows a more negative NAO that is connected to a more southerly jet and the expectation here is that E-Vector anomalies are opposite of the ones in the Indian Ocean experiment.
In the Indian Ocean only experiment, the E-Vector anomalies (Figure 8.6 b-c) show a similar spatial pattern to the forecasts of SEAS5, the OpenIFS control forecast, and the ERA5 conditions. The meridional E-Vectors in the Pacific jet region and at the Pacific-American coast are again southward which agrees with the strongly northward shifted jet in the Pacific (Figure 8.6 a). Over North America and into the Atlantic sector, the meridional E-Vectors are southward and the jet is shifted northward and extended. This shift of the jet projects well onto the positive AO/NAO described earlier in this experiment (chapter [OpenIFS experiments 5.2]). The magnitude of the anomalies in the experiment, however, is greater than in the control forecast or the SEAS5 forecast. This is not only caused by the smaller ensemble size in the experiment (25 members), as a 25 member subset of the control forecast shows values similar to the ones discussed in the 100 member control forecast here. The previous discussion of this experiment also shows that it has a stronger AO/NAO than the control forecast and thus a stronger teleconnection is expected.
As a check for a different type of teleconnection I am using the Pacific only experiment and the negative AO/NAO that resulted from this experiment. As expected, the opposite E-Vector signal can be seen in the Pacific experiment (Figure 8.7 b-c). In the North Pacific the E-Vectors have a northward component on the northern side of the jet position that continues over North America into the Atlantic. Similarly, the zonal E-Vectors have a more westward component on the northern side of the jet and an eastward component on the southern side. This is opposite to the ERA5 conditions and the Indian Ocean only experiment. These anomalies with more E-Vector divergence in the north indicate that more eddies decay on the northern flank of the jet. This helps to establish the jet in a more southerly position in both North Pacific and North Atlantic which is associated with the more negative AO/NAO in this experiment. The jet itself (Figure 8.7 a) is strengthened in this experiment and the jet exits are further to the south than in the climatological mean.

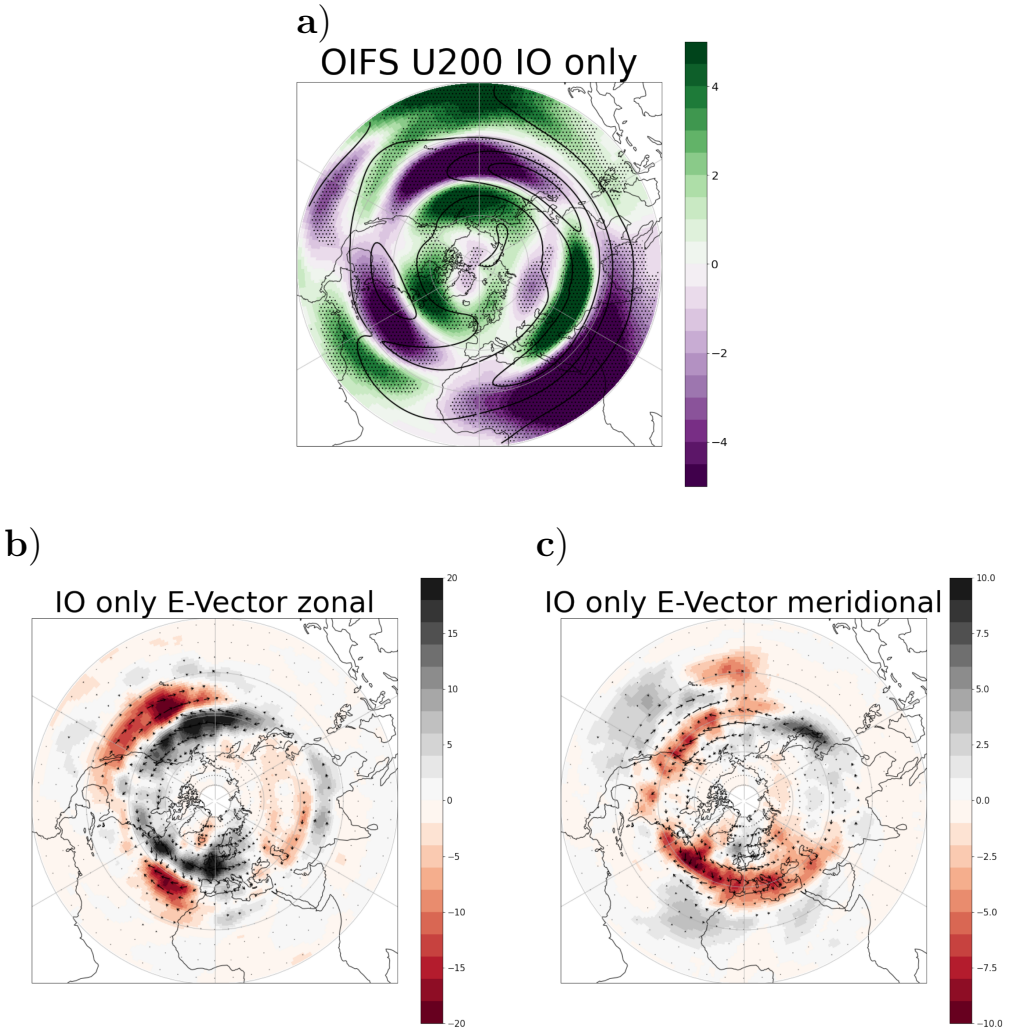


Figure 8.6: **OpenIFS IO only experiment mean flow and eddies in 2019/2020**. Relation between shifts in the mid-latitude jet, identified from 200 hPa zonal wind and eddy interactions with the jet, identified from E-Vector anomalies. **a)** U200 [m/s] climatological average (contours) and 2019/2020 anomalies (shading). **b)** E-Vector anomalies [m^2/s^2], with full E-Vectors (vectors) and zonal component (shaded). **c)** E-Vector anomalies, with full E-Vectors (vectors) and meridional component (shaded). Anomalies are calculated against the 1981-2020 climatological average. Stippling denotes significance and is calculated with a 2-sided bootstrapping at 5%.

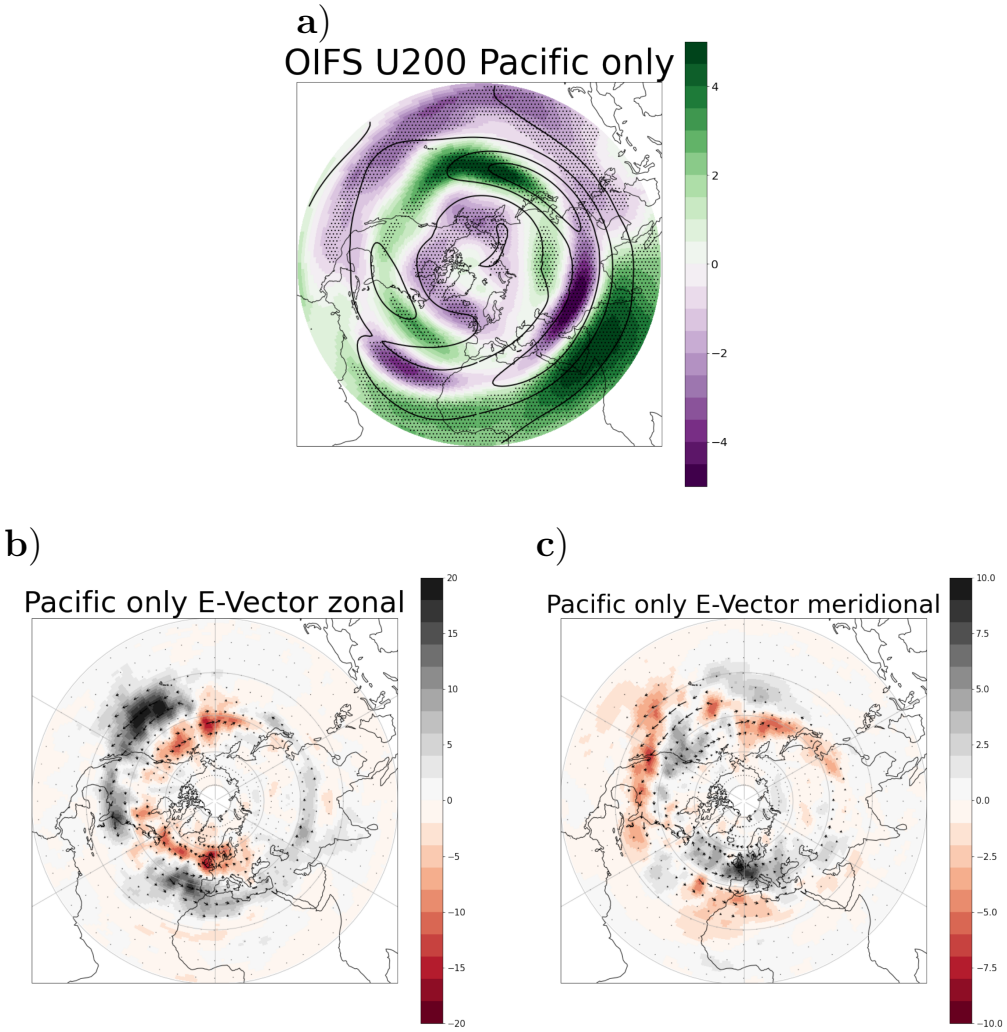


Figure 8.7: **OpenIFS Pacific only experiment mean flow and eddies in 2019/2020**. Relation between shifts in the mid-latitude jet, identified from 200 hPa zonal wind and eddy interactions with the jet, identified from E-Vector anomalies. **a)** U200 [m/s] climatological average (contours) and 2019/2020 anomalies (shading). **b)** E-Vector anomalies [m^2/s^2], with full E-Vectors (vectors) and zonal component (shaded). **c)** E-Vector anomalies, with full E-Vectors (vectors) and meridional component (shaded). Anomalies are calculated against the 1981-2020 climatological average. Stippling denotes significance and is calculated with a 2-sided bootstrapping at 5%.

The analysis of the E-Vectors in ERA5, model forecasts, and model experiments shows that anomalous eddy, mean-flow interactions in the Pacific propagate across North America and influence the North Atlantic jet. The teleconnections from the anomalous Indian Ocean Dipole, that reach the North Pacific via Rossby wave trains are then in the North Pacific picked up by the eddy, mean-flow teleconnection and propagated further downstream. In the Pacific jet exit region, the E-Vectors show that the jet is preconditioned towards a more northerly phase in the Atlantic. Comparisons to the U200 jet show that the jet is always more northward or strengthened when these anomalous eddy interactions are active. This mechanism is especially important for the SEAS5 model, as it closes the gap for the SEAS5 2019/2020 forecast between the North Pacific and the North Atlantic.

Chapter 9

Initial condition impact on the Southern Hemisphere

In this chapter I discuss the Southern Hemisphere anomalies of the DJF 2019/2020 and their likely origins. The southern high latitudes exhibited a negative Southern Annular Mode (SAM) characterised by a strong positive pressure anomaly over the South Pole. Interestingly, this negative SAM is also present in all OpenIFS experiments with perturbed SSTs discussed earlier (e.g. IO only, Pacific only). The fact that the southern high latitudes are in such a strong negative state, seemingly independent of the boundary conditions, leads me to investigate the causes of this anomaly further. Surprisingly, I find that in the OpenIFS, the atmospheric initial conditions from the 01.11.2019 used for the experiments are sufficient to get a negative SAM in the DJF mean, even when all boundary conditions are climatological average. I conclude that the IOD did not have a large impact on the southern high latitudes in 2019/2020 and that most of the anomalies there came from the initial conditions. This result is unusual, since most of the predictable signal on seasonal timescales stems usually from the boundary conditions.

Compared to teleconnections between the tropics and the Northern Hemisphere, the links between the tropics and the Southern Hemisphere are less researched. Over a long period a negative correlation between ENSO and the SAM can be observed (Dätwyler et al., 2020 [12]; Gong et al., 2010 [23]). This teleconnection is strongest between austral late-autumn to winter and late-spring to summer (Lim et al., 2013 [45]). However, no clear teleconnection between the IOD and the SAM is known. Since 2019/2020 experienced both a strong IOD and an anomalous SAM, this would be a good year to investigate the IOD-SAM relationship. However, all OpenIFS perturbation experiments discussed in chapter [OpenIFS experiments 5] share a strong

high (Z500 and MSLP) over Antarctica in the DJF mean. This height anomaly is irrespective whether the experiment has SST conditions in the Indian Ocean, Pacific, Atlantic, or the SSTs are perturbed in a different way (e.g. reduced IO only experiment). The height anomaly in all experiments can be characterised by a negative Southern Annular Mode (SAM, 1 EOF of Z500 between 30°S and 90°S). This uncommon behaviour of the experiments leads me to investigate the impact of the lower boundary conditions, the initial conditions, and the external forcing on the SAM conditions of 2019/2020.

In seasonal forecasts, strong and skilfully predicted extratropical atmospheric anomalies (after the first month) are usually associated with forcing from the lower boundary (i.e. SST, Sea Ice anomalies, land surface, etc.) (Palmer and Anderson, 1994 [60]; Reichler and Roads, 2003 [63]). In coupled forecast models, the SST and Sea-Ice anomalies that exist at the initialisation time of the forecast persist well into the season due to the longer timescales of both SST and Sea Ice and thus offer a chance of a skilful forecast. In uncoupled models (like the OpenIFS), SST and Sea-Ice are the lower boundary conditions (BC) and have a continuous influence on the seasonal atmospheric anomalies. In the DJF season of 2019/2020 in the Southern Hemisphere, these lower BC do not seem to have a strong impact on the atmosphere.

A factor that had the potential to strengthen the impact of the initial conditions on the seasonal DJF mean in the Southern Hemisphere is the occurrence of a rare sudden stratospheric warming on the 16.09.2019 (Rao et al., 2020 [62]). This sudden stratospheric warming was predicted by a number of forecast models on the subseasonal range including the ECMWF, UKMO, Australian Bureau of Meteorology, and Japanese Meteorological Agency (Lim et al., 2020 [44]). The occurrence of a sudden stratospheric warming is very rare in the Southern Hemisphere (Lim et al., 2020 [44]). Since this SSW occurred before the initialisation of the DJF forecast, its effects are contained in the initial conditions. This offers a first insight why the initial conditions were so important for the state of the Southern Hemisphere.
The 4 additional experiments used in this chapter are described in Table 9.1. As a first test, I set all lower boundary conditions to climatological average, leaving all initial conditions and external forcing from 2019/2020 (climatological BC experiment Figure 10.1 a). As a contrast to the climatological BC experiment, I use an experiment with climatological initial conditions and 2019/2020 boundary conditions (climatological IC experiment Figure 10.1 b). Both these experiments use 2019/2020 external forcing.

This external forcing includes Aerosol forcing, greenhouse gases, and volcanic activity in 2019/2020 (none present). A comparison with external forcing from 1981/1982 is also conducted ("climatological BC 81 external" and "climatological IC 81 external" Figure 10.1 c, Figure 10.1 d, respectively). The model names and input parameters are described in Table 9.1. Comparing the climatological BC and climatological IC experiments with each other and with the experiments with 1981/1982 external forcing, shows which aspects of the model conditions are of importance for the SH forecast of 2019/2020.

experiment Name	**initial conditions (IC)**	**boundary conditions (BC)**	**external forcing**
control forecast	ERA5 01.11.2019	ERA5 2019/2020	2019/2020
climatological IC	01.11. climatological 1981-2020	ERA5 2019/2020	2019/2020
climatological BC	ERA5 01.11.2019	climatological 1981-2020	2019/2020
climatological IC 81 external	01.11. climatological 1981-2020	ERA5 2019/2020	1981/1982
climatological BC 81 external	ERA5 01.11.2019	climatological 1981-2020	1981/1982

Table 9.1: **OpenIFS forcing for the Southern Hemisphere experiments**. Description of the forcing in the experiments used to investigate the Southern Hemisphere anomalies in 2019/2020. Separated into experiment Name, initial conditions supplied, boundary conditions supplied, and year of the external forcing.

The DJF mean of the climatological BC experiment (Figure 9.1 a) shows that the negative SAM exists even in the absence of any lower boundary anomalies. The strongest positive Z500 anomalies are over the Weddell Sea and the Ross Sea, evident in both the original control forecast (chapter [OpenIFS model 5.1] Figure 5.1 b) and this experiment. Interestingly, the NH also shows some anomalies that are consistent with the NH anomalies from 2019/2020 (i.e. the positive AO). However, the NH anomalies are weaker than the effects of the IO only experiment. Meanwhile, the anomalies over the Southern Hemisphere are large and consistent and show that the IC have a long lasting impact on the southern mid- to high-latitudes. The anomalies of the DJF mean are mostly the effect of the early months (December and to a lesser degree January). This time evolution and the decay of the impact of the initial conditions is discussed below (chapter [Individual months of the Southern Hemisphere 9.1]).

The second experiment with climatological IC and 2019/2020 BC (Figure 9.1 b) shows similar anomalies in both Hemispheres. The southern mid- to high-latitudes are still characterised by a high over Antarctica. This high shows centres of action in the same location as the climatological BC experiment, but the magnitude of the anomalies is weaker and larger areas are insignificant. The Northern Hemisphere anomalies, however show larger anomalies in this climatological IC experiment than in the climatological BC experiment. As expected from the OpenIFS control forecast and the various OpenIFS experiments conducted in chapter [OpenIFS experiments 5], the SST anomalies in the tropics (especially in the Indian Ocean) have a large impact on the Northern Hemisphere anomalies in this winter. Contrasting these two experiments does not clearly solve the question whether the Southern Hemisphere anomaly is more influenced by the IC or the BC. From these two experiments there seems to be an impact of both IC and BC on the strong negative SAM. One caveat is that these two experiment share the same external forcing and this external forcing could be the reason for the negative SAM. To answer this question I ran the same two experiments again, but with the external forcing set to 1981/1982 (called "climatological BC 81 external" and "climatological IC 81 external" Figure 9.1 c, Figure 9.1 d, respectively). It would have been better to set the external forcing to a climatological average in these experiments, but technical limitations of the OpenIFS prevented me from doing so. As the alternative I chose to use external forcing from the earliest years of the hindcast as an opposite to the 2019/2020 forcing.

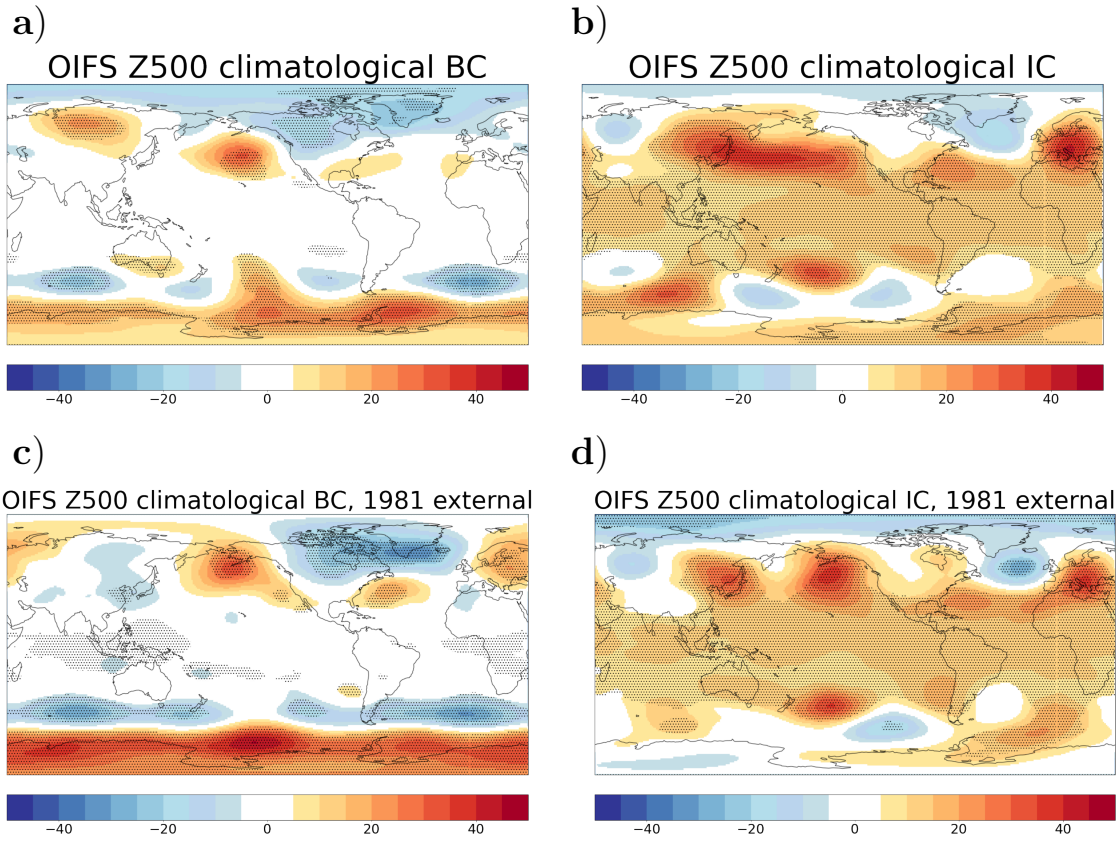


Figure 9.1: **Southern Hemisphere anomalies in the DJF season** in different OpenIFS experiments. Z500 anomalies [m] from experiments described in Table 9.1. **a)** the climatological BC experiment, **b)** climatological IC experiment, **c)** climatological BC 81 external forcing experiment, and **d)** climatological IC 81 external forcing experiment. Anomalies calculated against the 1981-2020 climatological average. Stippling denotes significance and is calculated with a 2-sided bootstrapping at 5%.

The climatological BC 81 external experiment (Figure 9.1 c) shows Z500 anomaly patterns that are similar to climatological BC experiment (Figure 9.1 a). In the Northern Hemisphere a weak positive NAO and a high anomaly over the Aleutian region are visible. The Southern Hemisphere on the other hand shows a stronger negative SAM with a large significant positive anomaly over Antarctica and negative anomalies surrounding it. Comparing the climatological BC and climatological BC 81 external experiments shows that using the external forcing from a different year does not decrease the strength of the negative SAM, but the amplitude is even slightly higher. This comparison shows that the external forcing from 2019/2020 did not have a large impact on the negative SAM.

To investigate the impact of the external forcing from 1981/1982, I use the climatological IC 81 external experiment (Figure 9.1 d) as a contrast to the climatological BC 81 external experiment. Over the Northern Hemisphere, the climatological IC 81 external experiment shows similar results to the climatological IC experiment with a positive AO/NAO. The Southern Hemisphere on the other hand shows only very weak signals. The fact that there is no strong signal over the southern mid- to high-latitudes when the external forcing from 1981/1982 is used, shows that the external forcing of 1981/1982 is unlikely to play a large role in shifting the Southern Hemisphere towards a negative SAM.

These 4 experiments show together that the IC from 2019/2020 are enough to create a significant negative SAM in DJF even with climatological BC and varying external forcing. The experiments also show that the BC from 2019/2020 are not enough to create the negative SAM. To get a better understanding how the IC and BC influence the Southern Hemisphere, I analyse the NDJF months in the following individually.

9.1 Individual months of the Southern Hemisphere

To investigate the hypothesis that the impact of the IC last well into the DJF season, the previous seasonal means are split into individual months and the November is included in the analysis. Since the ensemble members of the November month are much closer together than in the later months after initialisation (ensemble spread plateaus after approximately 30 days), the scale for November anomalies is adjusted to accommodate the larger values in the ensemble mean.

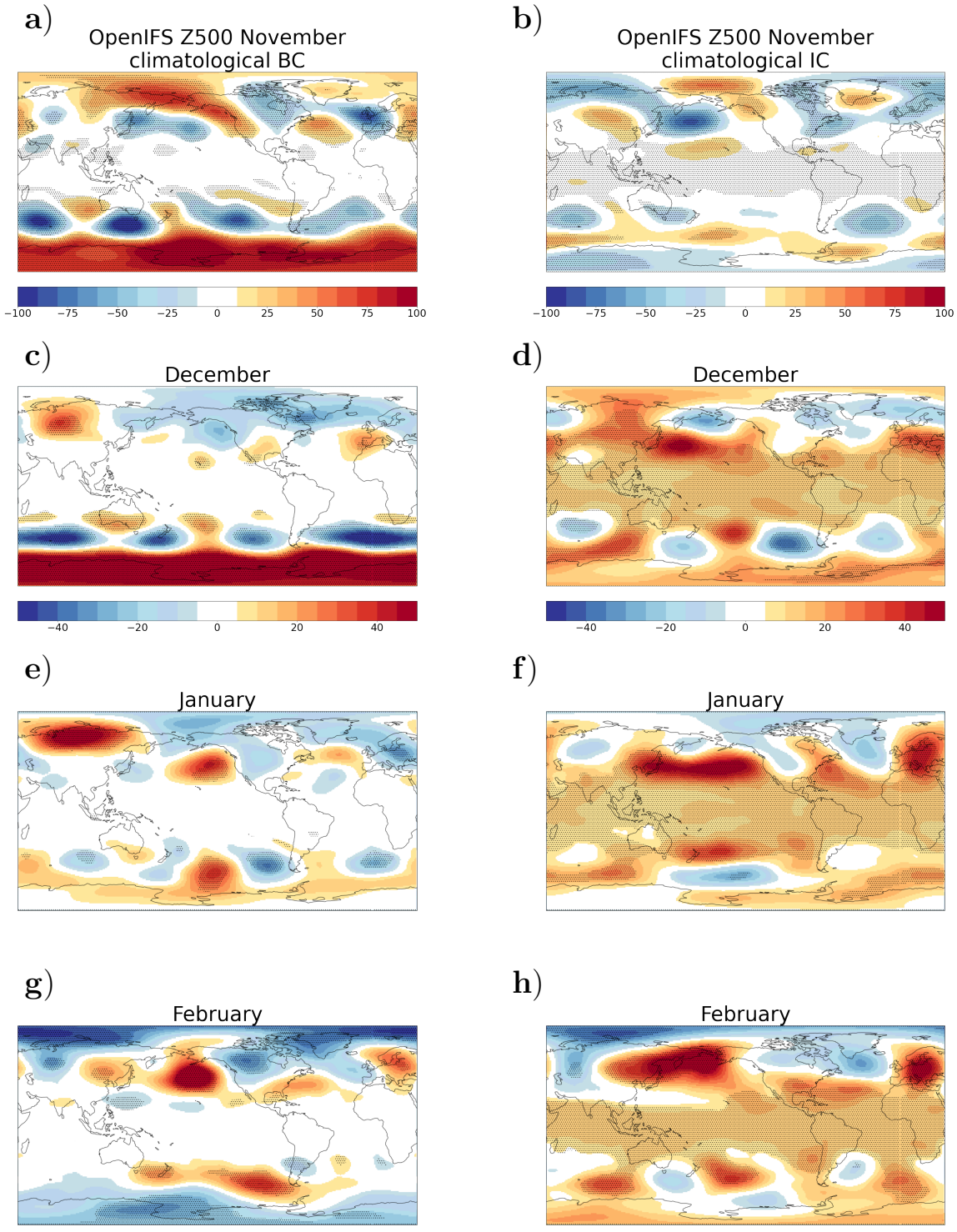


Figure 9.2: **Southern Hemisphere anomalies in months with forcing from 2019/2020** in the two different OpenIFS experiments. Z500 anomalies [m] from the experiments described in Table 9.1 with the external forcing set to 2019/2020. **Left** climatological BC experiment, **Right** climatological IC experiment. **Top** row November, **Second** row December, **Third** row January, and **Fourth** row February. Anomalies calculated against the 1981-2020 climatological average. Stippling denotes significance and is calculated with a 2-sided bootstrapping at 5%.

In November, the climatological BC experiment (left column of Figure 9.2) shows a very strong negative SAM, while the SAM is neutral or even slightly positive in the climatological IC experiment (right column in Figure 9.2). This is expected for the monthly mean of the first month, as the IC still have a very strong influence on this month. Investigating the IC themselves (01.11.2019) shows that the SAM starts in a very negative phase (not shown). As the season progresses into December and January, the strength of the SAM declines in the climatological BC experiment (left column), but is still slightly negative even in January. In February, the SAM is in a positive state, cancelling some of the negative signal from December in the DJF mean. In contrast, the climatological IC experiment (right column Figure 9.2) starts (as designed) in a very weak state, with a mostly neutral SAM. In December a slight negative SAM develops, that stays in a weak negative state the entire DJF season. These two experiments again suggest that the negative SAM is a combination of the IC and the BC forcing. However, the experiments with external forcing from 1981/1982 do not suggest the same (Figure 9.3). The climatological BC 81 external experiment (left column Figure 9.3) shows again the strong negative SAM in the first months (NDJ) of the experiment that lasts even into January. Only February shows a neutral SAM in this experiment. Meanwhile, the climatological IC 81 external experiment (right column Figure 9.3) does not show a clear negative SAM in any month. This absence of a negative SAM shows that it is unlikely that the BC had a large influence on the SAM.

This analysis of the strong negative SAM in 2019/2020, conducted with the OpenIFS model shows that:

- The impact of the November initial conditions lasts well into the DJF season in the southern mid- to high-latitudes in 2019/2020.
  - The IC impact decays only in January 2020 which is slower than usual for most seasonal forecasts.
- A likely reason for the strong impact of the initial conditions is the sudden stratospheric warming event that occurred in the austral spring season.
- The boundary conditions likely had a small influence on the negative SAM.
  - The BC can not be fully disregarded, since the climatological IC experiment shows a negative SAM.
- The external forcing does not show a clear impact on the SAM in either direction.

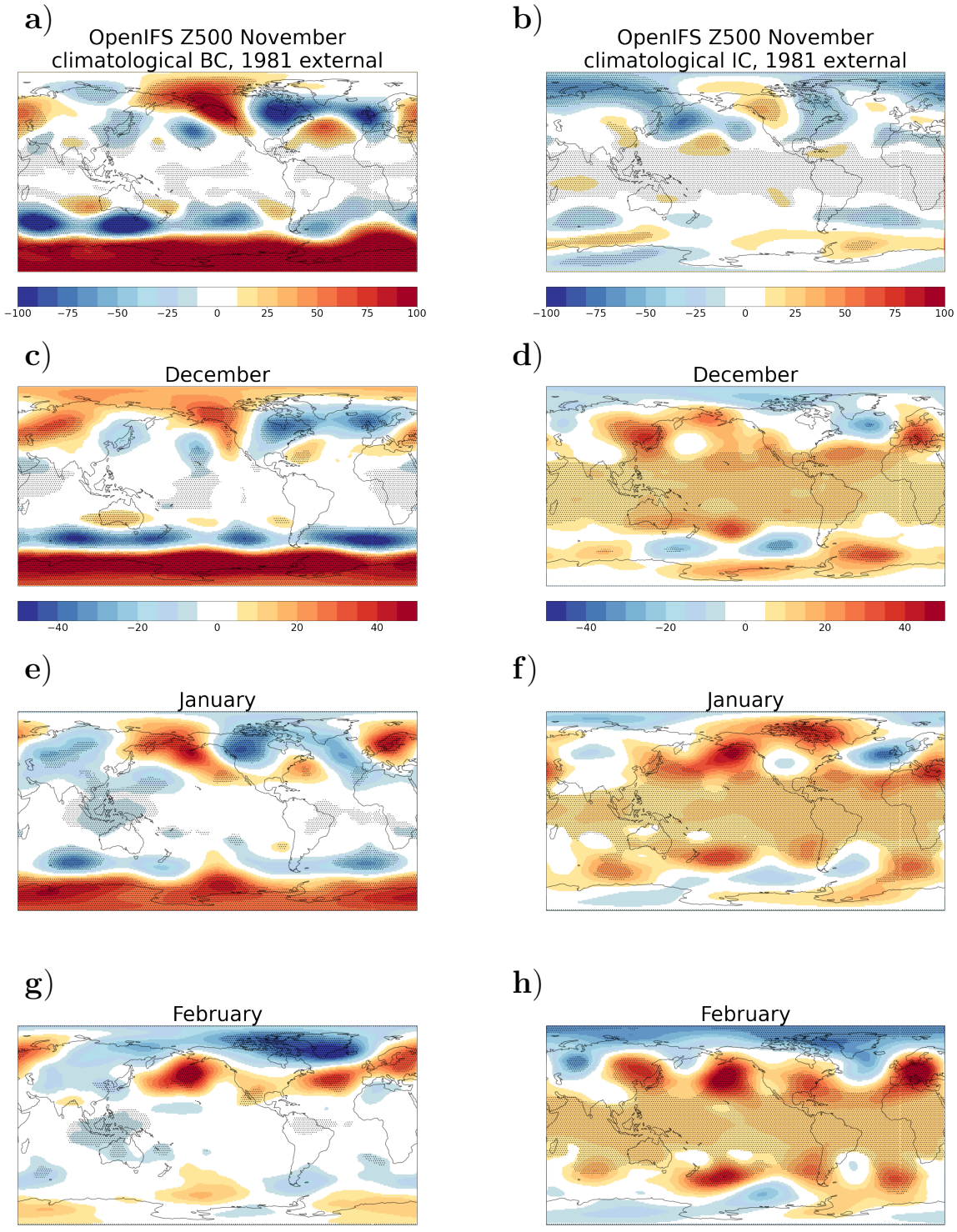


Figure 9.3: **Southern Hemisphere anomalies in months with forcing from 1981/1982** in the two different OpenIFS experiments. Z500 anomalies [m] from the experiments described in Table 9.1 with the external forcing set to 1981/1982. **Left** climatological BC 81 external forcing experiment, **Right** climatological IC 81 external forcing experiment. **Top** row November, **Second** row December, **Third** row January, and **Fourth** row February. Anomalies are calculated against the 1981-2020 climatological average and not detrended. Stippling denotes significance and is calculated with a 2-sided bootstrapping at 5%.

Chapter 10

Differences in hindcasts

In this chapter I investigate the impact of the hindcast on the calculated anomalies. Seasonal forecasts typically only show the state of a particular year as the deviation from the mean (climatological average, as this thesis does as well). Therefore, the climatological average has a large impact on the anomalies and different climatological averages lead to different anomalies. Here, I contrast three different versions of hindcasts that all represent a reasonable way to create a model climatology. The differences between these possible climatological states is on the same order of magnitude as the seasonal anomaly of some years.

10.1 Geopotential height differences between models

In seasonal averages the main observable signal is the climatological average. This includes the equator to pole temperature and pressure gradient, the average position of the jet stream and more (e.g. Webster, 2020 [86]). Because it is difficult to evaluate any deviations from these mostly average states, it is common to show/calculate deviations from these climatological average (anomalies). The anomalies show the seasonal deviation of the current year from the average conditions. For the NAO these anomalies are a positive or negative NAO, indicating a stronger or weaker equator to pole pressure gradient, respectively. However, this means that the anomalies of a particular year are influenced by climatological average that is subtracted. A simple example is the anomaly of surface temperature of a recent year (e.g. 2019/2020). This temperature anomaly will show over a majority of the globe a positive anomaly due to climate change. Therefore, anomalies from a climatological period of 1981-2020 are different to anomalies from a climatological period of 2000-2020. This is

true for reanalyses and models. In addition, studies have shown that multi-decadal variations exist in many parts of the climate system (NAO Hurrell and Van Loon, 1997 [35]; ENSO Torrence and Webster, 1999 [78]). O'Reilly et al. (2017 [58]) show that the forecast skill of seasonal forecast models similarly has decadal variations. In their work, they discuss the Pacific/North American (PNA) and NAO index and show a large drop in seasonal forecast skill in the mid 20.th century for both indices. Weisheimer et al. (2020 [89]) discuss this drop in skill in another large hindcast and expand the variation of forecast skill by showing that ENSO has a similar drop in forecast skill. Therefore, the choice of hindcast (period and type) can have an impact on the results.
In this work I am using the period 1981-2020 of realistic (control) model runs with realistic forcing from each year as the hindcast. However, alternative methods to create a climatological average are also feasible. For example a baseline experiment with climatological boundary conditions could be considered. These alternatives become more important when perturbed experiments are conducted (like the IO only experiment in this work). Here, most boundary conditions are set to climatological average and only limited regions are perturbed. So it could be argued that the perturbed experiments are closer to a climatological average hindcast, rather than a full "Normal" hindcast.
To understand how large the role of the climatological base state on the anomalies is, I discuss three model base states that could be used as a climatological average. These base states are:

- "Normal" hindcast (5 ensemble member), with every year between 1981-2020 run with ERA5 initial and boundary conditions.
- "Average boundary" hindcast (5 ensemble member), with every year between 1981-2020 run with ERA5 initial conditions, but boundary conditions set to climatological average (1981-2020) in every year.
- "One average year", an experiment (25 ensemble member) with all initial and boundary conditions set to 1981-2020 climatological average.

In a climate where the atmosphere responds completely linearly to boundary forcing, the three hindcasts would be (statistically) identical and no coherent anomalies would be observable. Since the climate system does not behave linearly, differences between the two hindcasts (and the climatological experiment) are observable.

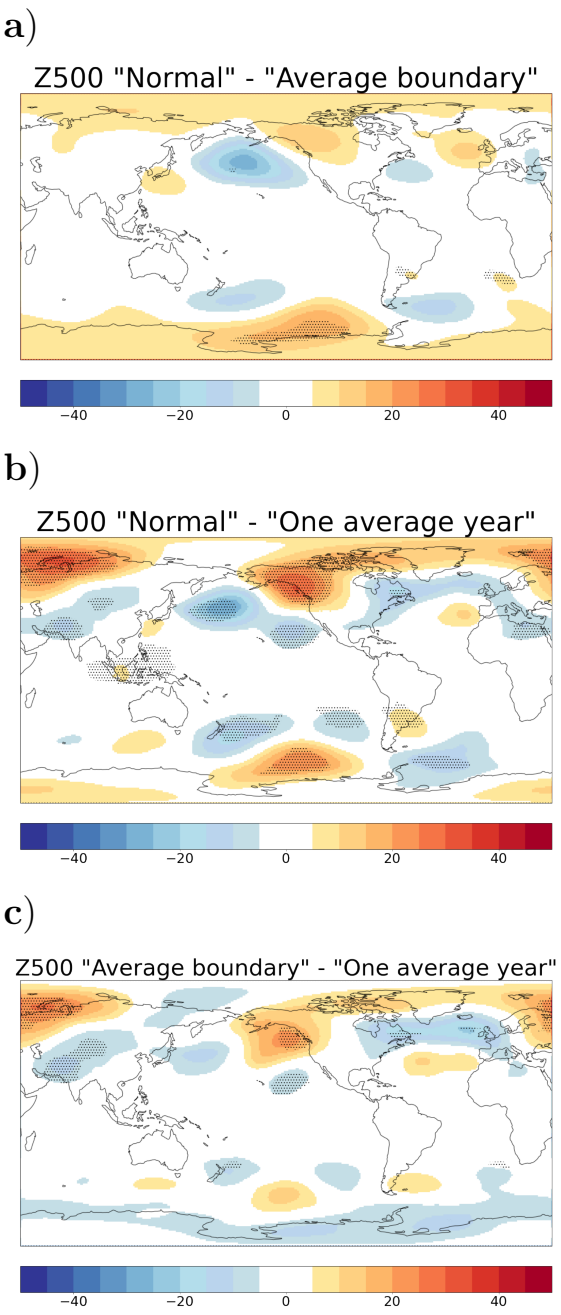


Figure 10.1: **Differences in DJF Z500 climatological averages** calculated in different ways [m]. The time-mean differences between three possible OpenIFS climatological averages. **a)** "Normal" hindcast minus "Average boundary" hindcast, **b)** "Normal" hindcast minus "One average year" experiment, and **c)** "Average boundary" hindcast minus "One average year" experiment.

The discussion below involves (and shows) the differences between the hindcasts, since the absolute values of the hindcasts would mainly show the climatological average in all hindcasts.
The Z500 difference between the two hindcasts (Figure 10.1 a) and the hindcasts to the experiment (Figures 10.1 b and c) show differences that are in the lower range of seasonal anomalies (compare to C3S forecast anomalies for 2019/2020 e.g. Figure 4.4). The fact that the different hindcast methods even have the same magnitude as anomalies from a particular winter, highlights the importance of the choice of hindcast method. The larger Z500 differences are located in the extratropics. Between the "Normal" hindcast and the "Average boundary" hindcast, the difference (Figure 10.1 a) roughly resembles a El Niño pattern, with a negative anomaly over the Aleutian region and as a whole a negative AO. In the southern high latitudes, the negative SAM pattern also resembles the expected impact of an El Niño (Lim et al., 2013 [45]). Similar results are observable in the comparison between the "Normal" hindcast and the "One year average" experiment (Figure 10.1 b). Apart from a larger amplitude, the patterns are very similar to the ones observed in the difference between the two hindcasts. This is also evident in the difference between the "Average boundary" hindcast and the "One average year" experiment (Figure 10.1 c). This difference is over most areas an increase of the difference between the two hindcasts.
As a whole the Z500 differences indicate that the impacts of El Niño and La Niña do not average out and while the "Normal" hindcast contains both events, the "Average boundary" hindcast and "One average year" experiment contain neither. This means that when an El Niño is connected to a strong low over the Aleutian region, but a La Niña is only connected to a mild high, the average Z500 over this the Aleutian is lower in the "Normal" hindcast than in the other two. To have a better understanding why the Z500 fields from these climatologies differ, I investigate the tropical regions and the average teleconnections in these climatologies.

10.2 Origin of differences and propagation

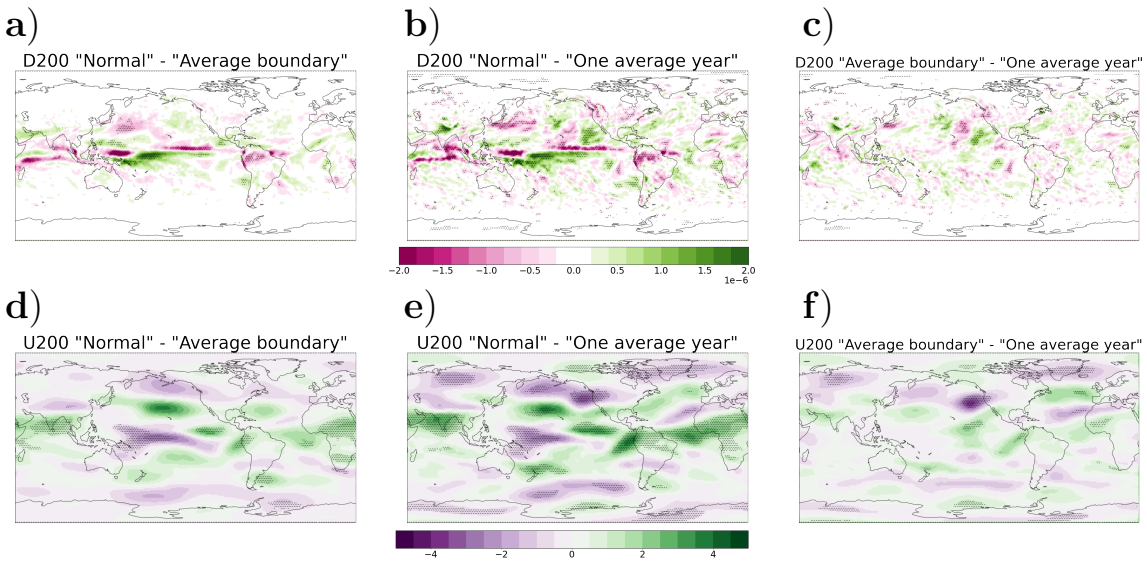


Figure 10.2: **Differences in DJF D200 and U200 climatological averages** calculated in different ways. The time-mean differences between three possible OpenIFS climatological averages. **Top** D200 [1/s] and **Bottom** U200 [m/s]. **Left** "Normal" hindcast minus "Average boundary" hindcast, **Middle** "Normal" hindcast minus "One average year" experiment, and **Right** "Average boundary" hindcast minus "One average year" experiment.

The tropical 200 hPa divergence differences (top row Figure 10.2) between the "Normal" hindcast compared to the "Average boundary" hindcast and "One average year" experiment are characterised by an El Niño like pattern with more divergence over the central Pacific and more convergence closer to the Maritime Continent. This shows that using average SST fields does not result in an average divergence field. One possible reason is a nonlinear response to El Niño and La Niña events, that is not captured in hindcasts with an average SST. The D200 signal in the Indian Ocean does not clearly show an IOD pattern. While there is more convergence in the east, the west does not show a clear convergence pattern and it more split into a northern divergence and a southern convergence. I would expect a stronger difference in the Indian Ocean in a comparison of SON hindcasts, when the IOD is typically stronger.

As evident in the Z500 differences (Figure 10.1 a), the differences in the tropical Pacific have an impact on the extratropical anomalies. The U200 zonal wind (second row Figure 10.2) shows shifts in the jet that are in consistent with the Z500 differences.

The jet in the "Normal" hindcast is further to the south and stronger in the Pacific compared to the "Average boundary" hindcast (Figure 10.2 d). Over the North Atlantic a minor increase in jet strength and shift to the south is evident. As a whole, these jet patterns are consistent with a low amplitude negative AO. The U200 difference between the "Normal" hindcast and the "One average year" experiment (Figure 10.2 e) exhibits similar patterns, but with slightly larger amplitude. A notable difference is over the eastern North Atlantic, where the jet is not shifted southwards, but strengthened. As before the difference between the "Average boundary" hindcast and the "One year hindcast is the residual of the previous two differences (Figure 10.2 f).

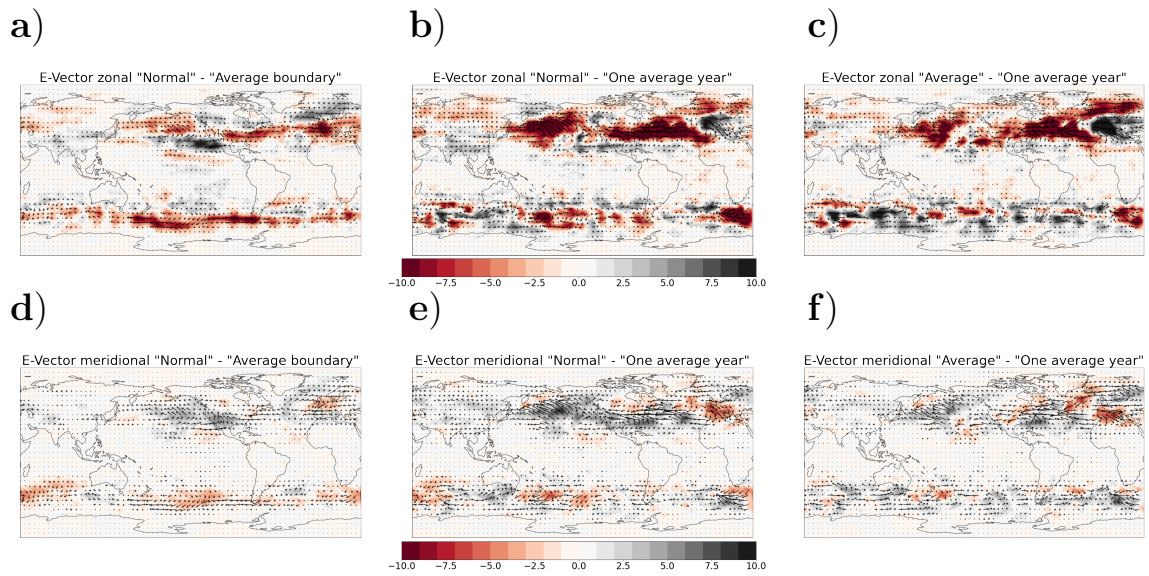


Figure 10.3: **Differences in DJF E-Vectors in climatological averages** calculated in different ways. The time-mean differences between three possible OpenIFS climatological averages. **Top** E-vectors $[m^2/s^2]$ with zonal component shaded and **Bottom** E-vectors with meridional component shaded. **Left** "Normal" hindcast minus "Average boundary" hindcast, **Middle** "Normal" hindcast minus "One average year" experiment, and **Right** "Average boundary" hindcast minus "One average year" experiment.

The differences between the climatologies also appears in the eddy, mean-flow teleconnections. Comparing the E-Vectors in the three climatologies (Figure 10.3), the zonal component (top row) shows larger differences in agreement with the larger climatological mean. The difference in the meridional component between the "Normal" hindcast and the "Average boundary" hindcast (Figure 10.3 d), shows negative values over the North Pacific and the Pacific-American coast. This negative signal agrees

with the southward shifted jet in the U200 field (Figure 10.2) and the negative Z500 anomaly over the Aleutian region (Figure 10.1). This consistent signal in Z500, U200, and the E-Vectors of a more southward jet in the "Normal" hindcast compared to the "Average boundary" hindcast shows a consistent difference between these hindcasts. It is not entirely clear which hindcast method is most appropriate as a climatological average, especially for experiments with perturbed boundary conditions and a more in-depth analysis of the non-linearities involved would be necessary for a certain conclusion. However, this analysis shows that the choice of the average can have a large impact on the anomalies and the signal in the climatological average should be considered when analysing seasonal anomalies.

Chapter 11

Conclusion and Outlook

Teleconnections are of high importance on seasonal timescales. Our model's ability to reproduce these teleconnections accurately does not only impact the ability of the models to forecast correctly, but also our confidence in them. The teleconnections from the Indian Ocean have in the past been neglected in favour of the stronger ENSO teleconnections from the Pacific. This thesis highlights the teleconnections from the Indian Ocean and their importance for the Northern Hemisphere winter season. The main tool used in this thesis is the detailed analysis of the 2019/2020 winter, the tropical-extratropical connections, and the contributors to the well forecasted positive NAO.
The following questions have guided the structure of this thesis:

- Why is the winter season 2019/2020 worth researching and what are its special features?
- Why do seasonal forecast models agree in their forecast of this winter and what are commonalities between models?
- How does different tropical SST forcing from 2019/2020 impact the atmospheric state in the OpenIFS model?
  - Is SST forcing in the Indian Ocean region enough to significantly impact the AO/NAO?
  - Does a combination of multiple ocean regions still show the impact of the IOD on the AO/NAO?
  - How does the climate change signal impact the teleconnections from the Indian Ocean?

- What teleconnection pathways are identifiable in 2019/2020?
  - What is the teleconnection pathway to the North Atlantic involving the stratosphere and how well is it represented in models?
  - What is the role of the Rossby wave train from the Indian Ocean to the North Pacific and from there to the North Atlantic?
  - What is the role of eddy, mean-flow interactions as a teleconnection mechanism between the North Pacific and North Atlantic?
- What is the sensitivity of the Southern Hemisphere to boundary- and initial-condition forcing in 2019/2020?
- Three different methods are used to define the climatological average of the model. How large are the differences between these possible climatological averages?

This thesis shows that the boreal winter 2019/2020 experienced unusual conditions in the tropics (namely the Indian Ocean region), the NH extratropics, the SH extratropics, and the European region. The Indian Ocean region is dominated by a strong positive IOD in SON 2019. This dipole is evident in SST, TP, and D200 and lasted unusually long into the DJF season. A notable anomaly of this winter is the absence of an ENSO event that accompanied the IOD event. In the 20.th Century reanalysis CERA-20C only very few IOD events are not accompanied by an ENSO event. This absence of an ENSO event makes this winter a prime example for the investigation of IOD teleconnections. The Northern Hemisphere shows a strong well predicted positive AO/NAO DJF 2019/2020. The fact that most of the C3S models predict this positive AO/NAO correctly, points to a common tropical source. In the absence of an ENSO event, this is likely to be the IOD. Europe similarly experienced unusual conditions in the DJF season. Most of Europe experienced a warm winter with higher precipitation in the North and less precipitation in the South, in line with the positive NAO.

Comparisons between ERA5, the C3S models, SEAS5, the uncoupled SEAS5, and the OpenIFS show an unusually high agreement between most models in the Northern Hemisphere. This high agreement points towards teleconnections from the tropics that the models are able to reproduce. The agreement of the OpenIFS with the other models and ERA5 also demonstrates the ability of the OpenIFS to reproduce major

factors of the winter 2019/2020. I use the OpenIFS model then to show that just the SST conditions in the Indian Ocean in NDJF 2019/2020 are enough to reproduce the main features of the NH extratropics of that winter. The experiment shows a strong positive AO/NAO with many features of ERA5 accurately reproduced. Reversed experiments and experiments with other ocean regions active do not manage to reproduce the positive AO/NAO and show the importance of the Indian Ocean region in the 2019/2020 winter. Combination experiments with multiple ocean regions similarly shows that only when the Indian Ocean is included, the AO/NAO is in a strong positive state. The combined experiments also show that there is a significant non-linear aspect, in favour of the signal from the Indian Ocean in the 2019/2020 winter. Linear combinations of individual experiments show a weaker signal compared to an experiments with multiple ocean regions active at the same time. In another experiment where a linear trend of climate change is removed from the experiments boundary conditions shows a spatially similar signal with a generally lower amplitude. The reduced IO only experiment still produces a positive AO/NAO, while the reduced Pacific only experiment still shows a slightly negative AO/NAO. The fact that the atmospheric response is weaker is interesting since the strength of the dipole itself (west - east) is the same in this experiment. Since the Indian Ocean is the fastest warming tropical Ocean, this effect could indicate that there will be more strong impacts of the IOD in the future.

It is unlikely that the Rossby wave train connecting Indian Ocean and North Atlantic is the only teleconnection active in the 2019/2020 winter. In ERA5 this wave train reaches from the Indian Ocean to the North Pacific and then into the North Atlantic. In models, this wave train is not well reproduced, with a number of models failing to show the wave train over North America. Since these models still manage to forecast the NAO well, the importance of the wave train is questionable (at least in these models). A composite analysis of a large ensemble investigating the wave train reveals that ensemble members with a strong wave train are more likely to have a positive AO as well. Similarly members with a weak wave train are less likely to have a positive AO. However, the results are only marginally significant and a lot of ensemble members with a strong wave train still have a neutral/negative AO. The results are even less reliable considering the wave train and the NAO. Here, a similar shift of probabilities exists with a stronger wave train having a higher probability of a positive NAO, but the results are not significant even with a very large (1600 member) ensemble. These results show that it is not likely that the wave train is the

sole teleconnection between IOD and NAO.

Since the stratosphere is an important pathway for El Niño teleconnections, I analyse whether a similar pathway plays a role for the IOD teleconnection in 2019/2020. Again, I use the forecast ability (or their lack of) of the C3S models, SEAS5, and the OpenIFS as an indication of the importance of this teleconnection (at least in the models). Many of the C3S models, SEAS5, and OpenIFS show major deficiencies in their stratospheric forecast of the winter 2019/2020, but have a well forecasted troposphere. This discrepancy between the model troposphere and stratosphere forecasts indicates that the stratosphere did not have a large impact on the model forecasts.

Since both the Rossby wave train and the stratospheric pathway only offer an uncertain teleconnection for the winter 2019/2020 I investigate the eddy, mean-flow interactions as an alternative teleconnection mechanism. With the E-Vectors described in Hoskins et al. (1983 [32]) I analyse this teleconnection in ERA5 and model experiments. In ERA5, the forecasts of 2019/2020, as well as the IO only experiments, the results of this analysis show an E-Vector field that is associated with a northward shifted and extended mid-latitude jet. These anomalies are observable in the U200 jet as well. Over the North Pacific, the Pacific jet is shifted northward and extended towards the North American coast. There, more anticyclonic wave breaking in the jet exit region of the Pacific jet preconditions the Atlantic jet into a northerly phase. In the North Atlantic similar E-Vector anomalies are observable. The Atlantic jet is similarly shifted northward and extended with higher E-Vector divergence (and more anticyclonic wave breaking) on the southern flank of the jet shifting the jet northward. In other experiments resulting in a negative NAO (e.g. Pacific only experiment), the opposite signal is observed with larger divergence (more cyclonic wave breaking) on the northern flank of the jet, shifting it towards the south. This interaction between the eddies and the jet in the North Pacific and North Atlantic serves as an alternative teleconnection pathway between the North Pacific and North Atlantic. This is of special importance for models that did not reproduce the wave train crossing North America (like SEAS5), but that do show the teleconnection via the eddy, mean-flow interactions (like SEAS5). For these models, the eddy, mean-flow interactions can close the gap and offer an explanation why the prediction of the NAO was correct in spite of missing parts of the wave train.

An anomalous high over Antarctica is a consistent signal in many of the OpenIFS experiments, ERA5, and the C3S forecasts. This high (negative SAM) is mostly independent of the boundary conditions used in the OpenIFS experiment (e.g. IO only, Pacific only, Atlantic only, etc.). An analysis into the cause of this persistent negative SAM shows that the atmospheric initial conditions have a large impact on the Southern Hemisphere in the 2019/2020 austral summer (DJF). Model experiments using varying boundary conditions, initial conditions, and external forcings show that the Southern Hemisphere anomaly is strongest in experiments with 2019 initial conditions. This is even the case when all boundary conditions are set to climatological average. An analysis of the evolution of this anomaly shows that the impact of the initial conditions from November lasts into December, weakly into January, and have decayed in February. This analysis shows that while the initial conditions had a strong impact on the southern high latitudes, the strong IOD did not have a large impact in DJF 2019/2020.

The choice of the model hindcast is considered by comparing a "Normal" model hindcast against a hindcast with climatological average boundary conditions and an experiment where initial conditions and boundary conditions are set to climatological average. The comparison shows that while the time-average boundary forcing and initial conditions are the same between possible hindcasts (by design), the atmosphere responds differently to each, leading to a different atmospheric climatological average. The difference between the hindcasts, shows a weak El Niño like signal in the "Normal" hindcast compared to the "Average boundary" hindcast in many variables. This shows that even if the SST forcing of El Niño and La Niña are mostly opposite, the atmospheric response is not. The impact of an El Niño event on the extratropics is larger than an equivalent La Niña event. Thus, when the hindcast dos not contain either, the extratropical climate is shifted closer to a La Niña like state (like in the "Average boundary" hindcast.
A similar non-linear response from the Indian Ocean is not identifiable. This is likely because in most years the impact of the IOD on the DJF season is small. I expect a stronger signal from the Indian Ocean if the SON season had been considered.

In this thesis I am using a TL159L60 resolution and I am showing that many aspects of the winter 2019/2020 are reproduced well at this resolution. However, it is also clear that the model has deficiencies which could potentially be lessened using

higher resolution. Especially increased vertical resolution could have solves some of the stratospheric deficiencies that the OpenIFS showed (see chapter 6). Tibaldi et al. (1990 [76]) and Buizza (2010 [8]) discuss that the benefits of increased resolution, but also that increased resolution does not solve all model problems. That the increased resolution is not synonymous with a better forecast is evident in this thesis, where the lower resolution OpenIFS manages to reproduce the Rossby wave train more accurately than the higher resolution SEAS5 (with TCo319). At the TL159L60 resolution I am able to save the different experiments without many storage problem (especially for the daily E-Vector analysis). Overall, the TL159L60 resolution is a good compromise where I am still able to run many experiments with a good number of ensemble members in a relatively short time, but a comparison to the same model experiments at higher resolution would still offer benefits.

As described in Molteni et al. (2015 [55]), defining the IOD via the precipitation dipole instead of SST has a closer link to the dynamics. In the analysis between IOD and ENSO events in CERA-20C I still use the SST metric, because the reanalysis of precipitation has larger uncertainties compared to the SST reanalysis. Comparing the CERA-20C precipitation to the GPCC (https://www.dwd.de/EN/ourservices/gpcc/gpcc.html) and the NOAA-20CR (https://psl.noaa.gov/data/20thC_Rean/) over Indonesia, shows large differences in the early part of the 20.th century. In the same period, the SST differences between CERA-20C, the NOAA-20CR, and the HadISST (https://www.metoffice.gov.uk/hadobs/hadisst/) are much smaller. For the analysis of the 2019/2020 boreal winter, the definition of the IOD from SST, precipitation, and upper level divergence all shows a positive IOD. However, the IOD is much more clear in the precipitation and divergence fields than in the SST fields where in DJF the negative anomaly in the eastern Indian Ocean is very weak. This is in agreement with the findings from Molteni et al. (2015 [55]) that using variables related to atmospheric dynamics is more appropriate for the analysis of teleconnections from the Indian Ocean.

Abid et al. (2023 [1]) found that the IOD has a stronger impact on the NAO in early winter (ND), while ENSO has more impact on the late winter (JF). Since the winter season is typically defined as DJF, the impact of ENSO dominates when ENSO and IOD co-occur (not in 2019/2020). Separating the 2019/2020 winter in an early and a late winter and conducting model experiments for both periods individually is beyond the scope of this thesis, but could give additional insight into the teleconnection

mechanisms of the IOD.

A possible way to extend this work is to use the OpenIFS initialised in different months and the SEAS5 initialisation from different months. This could extend the here presented analysis further and identify when exactly the eddy, mean-flow interactions and the shifts in the jet become important. The analysis could be combined with an analysis of the switch in teleconnection pattern from the IOD in early winter to ENSO in later winter. Investigating the transition between the different teleconnections (from IOD and ENSO) would likely also increase our understanding when each of them are active.

At the start of this thesis I try to "predict" the winter season of 2023/2024 from just the statistical connections between the IOD, ENSO, and the NAO. I wrote that the early winter would likely be in a positive NAO phase, connected to the positive IOD, while the late winter would show a negative NAO associated with the positive ENSO, this however did not happen. The winter showed a quadropole signal of Z500 over the North Atlantic with no clear NAO signal in either the early or late winter. A possible explanation for this behaviour is the strong positive SST anomalies in the North Atlantic, that might have had a very strong influence on this winter. This winter 2023/2024 shows that a lot more regions than the tropical Indian and Pacific Ocean influence the NAO and the investigation of more uncommon years is necessary to understand the teleconnections to the NAO in more detail.

One could use the well investigated 2019/2020 DJF season to investigate seasonal teleconnections in more depth. When we consider seasonal teleconnections we mostly ignore (or aggregate) the effects of the shorter timescales (like MJO and weather patterns). Since we have a decent understanding of the seasonally averaged teleconnections in 2019/2020 we could use this season to investigate the different timescales that teleconnections work on. This would require a very different analysis setup to the one presented here, starting from daily data, then possibly analysing the development of the Rossby wave train and its interaction with the MJO. In the North Atlantic one would have to transition from the seasonal average picture of the NAO and jet towards investigating individual weather patterns, their location, and persistence. This analysis would be a very complex, but very exciting and have the possibility to offer a new way of understanding teleconnections (from my knowledge and talking to

colleagues this has not been fully done yet).

This thesis discusses the DJF season 2019/2020 in detail. It shows that the strong IOD is unusual and that this IOD has a large impact on the Northern Hemisphere. The teleconnection from the IOD is associated with a higher likelihood of a positive NAO that is well predicted pointing towards a robust teleconnection from the IOD to NAO. Model experiments support this connection between the Indian Ocean and the North Atlantic, but both a stratospheric pathway, as well as a Rossby wave train do not explain the entire teleconnection mechanism. A teleconnection involving the interaction between short lived eddies and the mid-latitude jet close the teleconnection gap between the North Pacific and the North Atlantic. Jet shifts induced in the Pacific jet by larger eddy decay rates on the southern flank of the jet shift the Pacific jet northward. This signal propagates across North America and impacts the North Atlantic jet, shifting it to the north. This northward shifted jet is associated with a positive NAO that is observable in Z500. A similar impact of the IOD onto the Southern Hemisphere is not observable. In the DJF season 2019/2020 the phase of the SAM contains a large signal from the initial conditions and the impact of the Boundary forcing is weak.

11.1 Proposed teleconnection mechanism

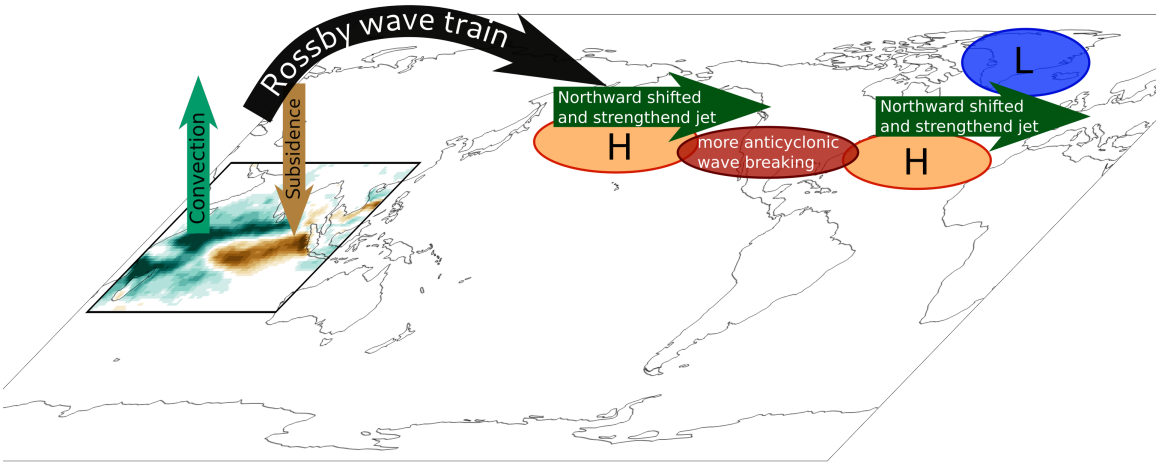


Figure 11.1: **Schematic of proposed IOD teleconnections** in DJF 2019/2020. Mechanisms are superimposed on top of ERA5 precipitation in the Indian Ocean in DJF 2019/2020.

As the teleconnection between the IOD and the NAO I propose the mechanisms shown in Figure 11.1

In the Indian Ocean region a dipole of SST, precipitation, and upper level divergence exists between the western and eastern Indian Ocean. This dipole is connected to anomalous convection in the west and subsidence in the east, triggering a quasi-stationary Rossby wave train. The emerging Rossby wave train propagates northeastward over Southeast Asia and Japan into the North Pacific. There, the wave-train projects onto the positive phase of the Aleutian cyclone appearing as a positive Z500 anomaly. From this high, the Pacific jet is shifted northward and extended, which is associated with more southward energy propagation from eddies (i.e. more anticyclonic wave breaking) on the southern flank of the jet stream. Between the Pacific jet exit region and the North Atlantic, this increased southward energy propagation sustains the northward shift of the jet and preconditions the North Atlantic

jet towards a northerly and strengthened phase. In the North Atlantic region, the northward shifted jet then projects onto the positive phase of the NAO, closing the teleconnection between the IOD and the NAO.

Bibliography

[1] Muhammad Adnan Abid, Fred Kucharski, Franco Molteni, and Mansour Almazroui. Predictability of Indian Ocean precipitation and its North Atlantic teleconnections during early winter. *npj Climate and Atmospheric Science*, 6(1):38–41, 2023.

[2] Omid Alizadeh. A review of ENSO teleconnections at present and under future global warming. *Wiley Interdisciplinary Reviews: Climate Change*, (June):1–20, 2023.

[3] D. G. Andrews and M. E. McIntyre. Planetary Waves in Horizontal and Vertical Shear: The Generalized Eliassen-Palm Relation and the Mean Zonal Acceleration. *Journal of the Atmospheric Sciences*, 1976.

[4] David S. Battisti and Anthony C. Hirst. Interannual Variability in a Tropical Atmosphere–Ocean Model: Influence of the Basic State, Ocean Geometry and Nonlinearity. *Journal of the Atmospheric Sciences*, pages 1687–1712, 1989.

[5] J Bjerknes. Theorie der aussertropischen Zyklonenbildung. 1937.

[6] J Bjerknes. Monthly Weather Reyiew Atmospheric Teleconnections From the Equatorial Pacific. *Monthly Weather Review*, 97(3):163–172, 1969.

[7] R. Buizza, M. Milleer, and T. N. Palmer. Stochastic representation of model uncertainties in the ECMWF ensemble prediction system. *Quarterly Journal of the Royal Meteorological Society*, 125(560):2887–2908, 1999.

[8] Roberto Buizza. Horizontal resolution impact on short- and long-range forecast error. *Quarterly Journal of the Royal Meteorological Society*, 136(649):1020–1035, 2010.

[9] Amy H. Butler, Lorenzo M. Polvani, and Clara Deser. Separating the stratospheric and tropospheric pathways of El Niño-Southern Oscillation teleconnections. *Environmental Research Letters*, 9(2), 2014.

[10] Christophe Cassou. Intraseasonal interaction between the Madden-Julian Oscillation and the North Atlantic Oscillation. *Nature*, 455(7212):523–527, 2008.

[11] A. Czaja and C. Frankignoul. Observed Impact of Atlantic SST Anomalies on the North Atlantic Oscillation. *Journal of Climate*, 15(18):2707–2712, 2002.

[12] Christoph Dätwyler, Martin Grosjean, Nathan J. Steiger, and Raphael Neukom. Teleconnections and relationship between the El Niño-Southern Oscillation (ENSO) and the Southern Annular Mode (SAM) in reconstructions and models over the past millennium. *Climate of the Past*, 16(2):743–756, 2020.

[13] A. Defant. OSCILLATIONS OF THE ATMOSPHERIC CIRCULATION OVER THE NORTH ATLANTIC OCEAN IN THE 25-YEAR PERIOD, 1881–1905. *Monthly Weather Review*, 1924.

[14] Daniela I.V. Domeisen, Olivia Martius, and Bernat Jiménez-Esteve. Rossby Wave Propagation into the Northern Hemisphere Stratosphere: The Role of Zonal Phase Speed. *Geophysical Research Letters*, 45(4):2064–2071, 2018.

[15] Marie Drouard, Gwendal Rivière, and Philippe Arbogast. The north Atlantic oscillation response to large-scale atmospheric anomalies in the northeastern Pacific. *Journal of the Atmospheric Sciences*, 70(9):2854–2874, 2013.

[16] L. Ferranti, T. N. Palmer, F. Molteni, and E. Klinker. Tropical-Extratropical Interaction Associated with the 30–60 Day Oscillation and Its Impact on Medium and Extended Range Prediction. *Journal of the Atmospheric Sciences*, 1990.

[17] Albert S. Fischer, Pascal Terray, Eric Guilyardi, Silvio Gualdi, and Pascale Delecluse. Two independent triggers for the Indian Ocean dipole/zonal mode in a coupled GCM. *Journal of Climate*, 18(17):3428–3449, 2005.

[18] Klaus Fraedrich and Klaus Müller. Climate anomalies in Europe associated with ENSO extremes. *International Journal of Climatology*, 12(1):25–31, 1992.

[19] John C. Fyfe. Separating extratropical zonal wind variability and mean change. *Journal of Climate*, 16(5):863–874, 2003.

[20] Chaim I. Garfinkel, Wen Chen, Yanjie Li, Chen Schwartz, Priyanka Yadav, and Daniela Domeisen. The Winter North Pacific Teleconnection in Response to ENSO and the MJO in Operational Subseasonal Forecasting Models Is Too Weak. *Journal of Climate*, 35(24):4413–4430, 2022.

[21] Chellappan Gnanaseelan, Milind Mujumdar, Ashwini Kulkarni, Supriyo Chakraborty, and Earth Sciences. *Assessment of Climate Change over the Indian Region*. 2020.

[22] Daoyi Gong and Shaowu Wang. Definition of Antarctic oscillation index. *Geophysical Research Letters*, 26(4):459–462, 1999.

[23] Tingting Gong, Steven B. Feldstein, and Dehai Luo. The impact of ENSO on wave breaking and southern annular mode events. *Journal of the Atmospheric Sciences*, 67(9):2854–2870, 2010.

[24] Feiyan Guo, Qinyu Liu, S. Sun, and Jianling Yang. Three types of Indian Ocean dipoles. *Journal of Climate*, 28(8):3073–3092, 2015.

[25] Zhe Han, Feifei Luo, and Jianghua Wan. The observational influence of the North Atlantic SST tripole on the early spring atmospheric circulation. *Geophysical Research Letters*, 43(6):2998–3003, 2016.

[26] Steven C. Hardiman, Nick J. Dunstone, Adam A. Scaife, Doug M. Smith, Ruth Comer, Yu Nie, and Hong Li Ren. Missing eddy feedback may explain weak signal-to-noise ratios in climate predictions. *npj Climate and Atmospheric Science*, 5(1):1–8, 2022.

[27] Steven C. Hardiman, Nick J. Dunstone, Adam A. Scaife, Doug M. Smith, Jeff R. Knight, Paul Davies, Martin Claus, and Richard J. Greatbatch. Predictability of European winter 2019/20: Indian Ocean dipole impacts on the NAO. *Atmospheric Science Letters*, 21(12):1–10, 2020.

[28] M. P. Hoerling, J. W. Hurrell, and T. Xu. Tropical origins for recent North Atlantic climate change. *Science*, 292(5514):90–92, 2001.

[29] Martin P. Hoerling and Arun Kumar. Atmospheric response patterns associated with tropical forcing. *Journal of Climate*, 15(16):2184–2203, 2002.

[30] James R. Holton and Gregory J. Hakim. *An introduction to dynamic meteorology: Fifth edition*, volume 9780123848. 2012.

[31] John D. Horel and John M. Wallace. Planetary-Scale Atmospheric Phenomena Associated with the Southern Oscillation. *Monthly Weather Review*, 1981.

[32] Brian J. Hoskins, Ian N. James, and Glenn H. White. The Shape, Propagation and Mean-Flow Interaction of Large-Scale Weather Systems. *Journal of the Atmospheric Sciences*, 1983.

[33] James W. Hurrell. Decadal trends in the North Atlantic oscillation: Regional temperatures and precipitation. *Science*, 269(5224):676–679, 1995.

[34] James W. Hurrell, Yochanan Kushnir, Geir Ottersen, and Martin Visbeck. An overview of the north atlantic oscillation. *Geophysical Monograph Series*, 134:1–35, 2003.

[35] James W. Hurrell and Harry Van Loon. Decadal variations in climate associated with the North Atlantic oscillation. *Climatic Change*, 36(3-4):301–326, 1997.

[36] Takeshi Izumo, Maxime Colin, Fei Fei Jin, and Bastien Pagli. The Hybrid Recharge Delayed Oscillator: A More Realistic El Niño Conceptual Model. *Journal of Climate*, 37(9):2765–2787, 2024.

[37] Stephanie J. Johnson, Timothy N. Stockdale, Laura Ferranti, Magdalena A. Balmaseda, Franco Molteni, Linus Magnusson, Steffen Tietsche, Damien Decremer, Antje Weisheimer, Gianpaolo Balsamo, Sarah P.E. Keeley, Kristian Mogensen, Hao Zuo, and Beatriz M. Monge-Sanz. SEAS5: The new ECMWF seasonal forecast system. *Geoscientific Model Development*, 12(3):1087–1117, 2019.

[38] Manish K. Joshi, Muhammad Adnan Abid, and Fred Kucharski. The Role of an Indian Ocean Heating Dipole in the ENSO Teleconnection to the North Atlantic European Region in Early Winter during the Twentieth Century in Reanalysis and CMIP5 Simulations. *Journal of Climate*, 34(3):1047–1060, 2021.

[39] Hsun Ying Kao and Jin Yi Yu. Contrasting Eastern-Pacific and Central-Pacific types of ENSO. *Journal of Climate*, 22(3):615–632, 2009.

[40] Ben P. Kirtman and J. Shukla. Influence of the Indian summer monsoon on ENSO. *Quarterly Journal of the Royal Meteorological Society*, 126(562):213–239, 2000.

[41] Stephen A. Klein, Brian J. Soden, and Ngar Cheung Lau. Remote sea surface temperature variations during ENSO: Evidence for a tropical atmospheric bridge. *Journal of Climate*, 12(4):917–932, 1999.

[42] Philip J. Klotzbach. El Niño-Southern Oscillation's impact on Atlantic basin hurricanes and U.S. Landfalls. *Journal of Climate*, 24(4):1252–1263, 2011.

[43] M. Leutbecher and T. N. Palmer. Ensemble forecasting. *Journal of Computational Physics*, 227(7):3515–3539, 2008.

[44] Eun-Pa Lim, Harry H. Hendon, Amy H. Butler, Rene D. Garreaud, Inna Polichtchouk, Theodore G. Shepherd, Adam Scaife, Ruth Comer, Lawrence Coy, Paul. A. Newman, David W. J. Thompson, and Hisashi Nakamura. The 2019 Antarctic sudden stratospheric warming. *SPARC newsletter*, (January):10pp, 2020.

[45] Eun Pa Lim, Harry H. Hendon, and Harun Rashid. Seasonal predictability of the southern annular mode due to its association with ENSO. *Journal of Climate*, 26(20):8037–8054, 2013.

[46] Hai Lin, Gilbert Brunet, and Juan Sebastian Fontecilla. Impact of the Madden-Julian Oscillation on the intraseasonal forecast skill of the North Atlantic Oscillation. *Geophysical Research Letters*, 37(19):2–5, 2010.

[47] Roland A. Madden and Paul R. Julian. Detection of a 40–50 Day Oscillation in the Zonal Wind in the Tropical Pacific. *Journal of the Atmospheric Sciences*, 1971.

[48] Roland A. Madden and Paul R. Julian. Observations of the 40–50-Day Tropical Oscillation—A Review. *Monthly Weather Review*, 1994.

[49] Gareth J. Marshall. Trends in the Southern Annular Mode from observations and reanalyses. *Journal of Climate*, 16(24):4134–4143, 2003.

[50] Adrian J. Matthews, Brian J. Hoskins, and Michiko Masutani. The global response to tropical heating in the Madden-Julian oscillation during the northern winter. *Quarterly Journal of the Royal Meteorological Society*, 130(601 PART B):1991–2011, 2004.

[51] C. S. Meinen and M. J. McPhaden. Observations of warm water volume changes in the equatorial Pacific and their relationship to El Nino and La Nina. *Journal of Climate*, 13(20):3551–3559, 2000.

[52] Ute Merkel, Matthias Prange, and Michael Schulz. ENSO variability and teleconnections during glacial climates. *Quaternary Science Reviews*, 29(1-2):86–100, 2010.

[53] Kristian Mogensen, Sarah Keeley, and Peter Towers. Coupling of the NEMO and IFS models in a single executable. *Technical Memorandum*, 736(April), 2012.

[54] Franco Molteni, Tim Stockdale, and Frederic Vitart. Understanding teleconnections with the Indo-Pacific region during the northern winter. *ECMWF Seminar on Seasonal Prediction*, (September):47, 2012.

[55] Franco Molteni, Timothy N. Stockdale, and Frédéric Vitart. Understanding and modelling extra-tropical teleconnections with the Indo-Pacific region during the northern winter. *Climate Dynamics*, 45(11-12):3119–3140, 2015.

[56] Yu Nie, Yang Zhang, Xiu Qun Yang, and Hong Li Ren. Winter and Summer Rossby Wave Sources in the CMIP5 Models. *Earth and Space Science*, 6(10):1831–1846, 2019.

[57] Christopher H O'Reilly. Interdecadal variability of the ENSO teleconnection to the wintertime North Pacific. *Climate Dynamics*, 51(9-10):3333–3350, 2018.

[58] Christopher H. O'Reilly, James Heatley, Dave MacLeod, Antje Weisheimer, Tim N. Palmer, Nathalie Schaller, and Tim Woollings. Variability in seasonal forecast skill of Northern Hemisphere winters over the twentieth century. *Geophysical Research Letters*, 44(11):5729–5738, 2017.

[59] Christopher H. O'Reilly, Tim Woollings, Laure Zanna, and Antje Weisheimer. The impact of tropical precipitation on summertime euro-Atlantic circulation via a circumglobal wave train. *Journal of Climate*, 31(16):6481–6504, 2018.

[60] T. N. Palmer and D. L.T. Anderson. The prospects for seasonal forecasting—A review paper. *Quarterly Journal of the Royal Meteorological Society*, 120(518):755–793, 1994.

[61] T. N. Palmer, R. Buizza, F. Doblas-Reyes, T. Jung, M. Leutbecher, G.J. Shutts, M. Steinheimer, and A. Weisheimer. Stochastic Parametrization and Model Uncertainty. *ECMWF Technical Memorandum*, 2009.

[62] Jian Rao, Chaim I. Garfinkel, Ian P. White, and Chen Schwartz. The Southern Hemisphere Minor Sudden Stratospheric Warming in September 2019 and its Predictions in S2S Models. *Journal of Geophysical Research: Atmospheres*, 125(14):1–19, 2020.

[63] T. J. Reichler and J. O. Roads. The role of boundary and initial conditions for dynamical seasonal predictability. *Nonlinear Processes in Geophysics*, 10(3):211–232, 2003.

[64] Gwendal Rivière and Marie Drouard. Understanding the contrasting North Atlantic Oscillation anomalies of the winters of 2010 and 2014. *Geophysical Research Letters*, 42(16):6868–6875, 2015.

[65] C G Rossby and And Collaborators. Relation between variations in the itensity of the zonal circulation of the atmosphere and the displacements of the semi-permanent centres of action. *MIT*, 1939.

[66] N Saji, B Goswami, P Vinayachandran, and T Yamagata. A dipole mode in the Tropical Ocean. *Nature*, 401(6751):360–363, 1999.

[67] Prashant D. Sardeshmukh and Brian J. Hoskins. The Generation of Global Rotational Flow by Steady Idealized Tropical Divergence. *Journal of the Atmospheric Sciences*, 1988.

[68] A. A. Scaife, A. Arribas, E. Blockley, A. Brookshaw, R. T. Clark, N. Dunstone, R. Eade, D. Fereday, C. K. Folland, M. Gordon, L. Hermanson, J. R. Knight, D. J. Lea, C. MacLachlan, A. Maidens, M. Martin, A. K. Peterson, D. Smith, M. Vellinga, E. Wallace, J. Waters, and A. Williams. Skillful long-range prediction of European and North American winters. *Geophysical Research Letters*, 2014.

[69] Adam A. Scaife, Chris K. Folland, Lisa V. Alexander, Anders Moberg, and Jeff R. Knight. European climate extremes and the North Atlantic Oscillation. *Journal of Climate*, 21(1):72–83, 2008.

[70] Adam A. Scaife and Doug Smith. A signal-to-noise paradox in climate science. *npj Climate and Atmospheric Science*, 1(1), 2018.

[71] S. Sharmila, H. Hendon, O. Alves, A. Weisheimer, and M. Balmaseda. Contrasting El Niño–La Niña Predictability and Prediction Skill in 2-Year Reforecasts of the Twentieth Century. *Journal of Climate*, 36(5):1269–1285, 2023.

[72] Daniel T. Skinner, Adrian J. Matthews, and David P. Stevens. North Atlantic Oscillation response to the Madden–Julian Oscillation in a coupled climate model. *Weather*, 77(6):201–205, 2022.

[73] Tim Stockdale, Stephanie Johnson, Laura Ferranti, Magdalena Balmaseda, and Simona Briceag. ECMWF's new long-range forecasting system SEAS5. *ECMWF Newsletter*, 2018.

[74] Max J. Suarez and Paul S. Schopf. A Delayed Action Oscillator for ENSO. *Journal of the Atmospheric Sciences*, pages 3283–3287, 1988.

[75] K. Takahashi, A. Montecinos, K. Goubanova, and B. Dewitte. ENSO regimes: Reinterpreting the canonical and Modoki El Nio. *Geophysical Research Letters*, 38(10):1–5, 2011.

[76] S. Tibaldi, T. N. Palmer, Branković, and U. Cubasch. Extended-range predictions with ecmwf models: Influence of horizontal resolution on systematic error and forecast skill. *Quarterly Journal of the Royal Meteorological Society*, 116(494):835–866, 1990.

[77] Robert A. Tomas and Peter J. Webster. The role of inertial instability in determining the location and strength of near-equatorial convection. *Quarterly Journal of the Royal Meteorological Society*, 123(542):1445–1482, 1997.

[78] Christopher Torrence and Peter J. Webster. Interdecadal changes in the ENSO-monsoon system. *Journal of Climate*, 12(8 PART 2):2679–2690, 1999.

[79] Kevin E. Trenberth, Grant W. Branstator, David Karoly, Arun Kumar, Ngar Cheung Lau, and Chester Ropelewski. Progress during TOGA in understanding and modeling global teleconnections associated with tropical sea surface temperatures. *Journal of Geophysical Research: Oceans*, 103(C7):14291–14324, 1998.

[80] Duane Waliser, K. Sperber, H. Hendon, D. Kim, E. Maloney, M. Wheeler, K. Weickmann, C. Zhang, L. Donner, J. Gottschalck, W. Higgins, I. S. Kang, D. Legler, M. Moncrieff, S. Schubert, W. Stern, F. Vitart, B. Wang, W. Wang, and S. Woolnough. MJO simulation diagnostics. *Journal of Climate*, 22(11):3006–3030, 2009.

[81] G. T. Walker. CORRELATION IN SEASONAL VARIATIONS OF WEATHER—A FURTHER STUDY OF WORLD WEATHER. *Monthly Weather Review*, 1924.

[82] G. T. Walker and E. W. Bliss. World Weather 6, 1936.

[83] John M. Wallace and David S. Gutzler. Teleconnections in the Geopotential Height Field during the Northern Hemisphere Winter. *Monthly Weather Review*, 1981.

[84] Guojian Wang, Wenju Cai, Kai Yang, Agus Santoso, and Toshio Yamagata. A Unique Feature of the 2019 Extreme Positive Indian Ocean Dipole Event. *Geophysical Research Letters*, 47(18):1–9, 2020.

[85] Xin Wang and Chunzai Wang. Different impacts of various El Niño events on the Indian Ocean Dipole. *Climate Dynamics*, 42(3-4):991–1005, 2013.

[86] Peter J. Webster. *Dynamics of The Tropical Atmosphere and Oceans*. John Wiley and Sons, Ltd, 2020.

[87] Peter J. Webster, Andrew M. Moore, Johannes P. Loschnigg, and Robert R. Leben. Coupled ocean±atmosphere dynamics in the Indian Ocean during 1997±98. *Nature*, 401(September):356–360, 1999.

[88] Antje Weisheimer, Laura H Baker, Jochen Bröcker, Chaim I Garfinkel, Steven C Hardiman, Dan L R Hodson, Tim N Palmer, Jon I Robson, Adam A Scaife, James A Screen, Theodore G Shepherd, Doug M Smith, and Rowan T Sutton. The Signal-to-Noise Paradox in Climate Forecasts. 2024.

[89] Antje Weisheimer, Daniel J. Befort, Dave MacLeod, Tim Palmer, Chris O'Reilly, and Kristian Strømmen. Seasonal forecasts of the twentieth century. *Bulletin of the American Meteorological Society*, 101(8):E1413–E1426, 2021.

[90] Daniel S. Wilks. Preface to the Fourth Edition. In Daniel S Wilks, editor, *Statistical Methods in the Atmospheric Sciences (Fourth Edition)*. Elsevier, fourth edi edition, 2019.

[91] Klaus Wyrtki. Water displacements in the Pacific and the genesis of El Nino cycles. *Journal of Geophysical Research: Oceans*, 90(C4):7129–7132, 1985.

[92] Xinqiang Xu, Lei Wang, and Weidong Yu. The unique mean seasonal cycle in the Indian Ocean anchors its various air-sea coupled modes across the basin. *Scientific Reports*, 11(1):1–8, 2021.

[93] R. K. Yadav, D. A. Ramu, and A. P. Dimri. On the relationship between ENSO patterns and winter precipitation over North and Central India. *Global and Planetary Change*, 107:50–58, 2013.